AN ANALYSIS OF THE PECULIAR VELOCITY STRUCTURE IN GALAXY CLUSTER A154

A DISSERTATION

SUBMITTED TO THE GRADUATE SCHOOL

IN PARTIAL FULFILLMENT OF THE REQUIREMENTS

FOR THE DEGREE

DOCTOR OF EDUCATION

BY

RYAN WESLEY TOBIN

DR. ROBERT BERRINGTON - ADVISOR

BALL STATE UNIVERSITY

MUNCIE, INDIANA

DECEMBER 2016

To Elijah, Samuel and Zachary...

The important thing is not to stop questioning. Curiosity has its own reason for existing.

–Albert Einstein

Never fear answers, only fear running out of questions.

–Unknown

Acknowledgements

I would like to thank Dr. Robert Berrington for his years of patience, advice and encouragement. I would also like to thank my graduate committee members, Dr. Patricia Lang, Dr. Ronald Kaitchuk and Dr. Thalia Mulvihill, and the Department of Physics and Astronomy faculty for their support, instruction and advice throughout the years.

I also want to thank my wife, Amy, and my sons, Elijah and Samuel, who supported me when I was gone — but always made me glad to come home. This research is a testament to their support and perseverance as much as it is to mine own.

Finally, I would like to thank Mr. Marc Semanchik, who helped me to overcome a disability and provided me with a sounding board to discuss and refine my understanding of various complex topics. Without your help, I would never have been able to finish.

Thank you all!

Contents

1 Introduction **1**

1.1 Understanding Galaxy Clusters 2

1.2 Importance of Further Study 2

1.3 Abell 154 and Dissertation Overview 3

2 Background **5**

2.1 Hierarchical Merging 5

2.2 Cluster Properties 6

2.2.1 Cosmic Distances 7

2.2.2 Cluster Mass 13

2.2.3 Timescales 15

2.3 The Relaxed Cluster 19

2.3.1 Distributions 20

2.3.2 Cooling Flows and X-ray Emission 23

2.4 The Merging Cluster 26

2.4.1 Merger Shocks 27

2.4.2 Cluster Environments 28

2.5 Prior Studies of Abell 154 30

2.5.1 Morphology and Appearance 33

2.5.2 Cluster Core 34

2.5.3 Previous Radial Velocities 37
2.5.4 X-ray Sources and Cooling Flow Signatures 37
2.5.5 Photometric Analysis 41

3 Radial Velocity Measurements **42**
3.1 New Data 42
3.1.1 Targets for Observation 43
3.1.2 Observations 43
3.1.3 Reduction 44
3.1.4 Reconciling Absorption- and Emission-Based Data 55
3.2 Literature Data 55
3.3 Compilation of Data 57
3.3.1 Reconciling Literature Data with New Data 57

4 Data Analysis And Discussion **62**
4.1 Statistical Analysis 62
4.1.1 3-σ Clipping 64
4.1.2 Gaussian Fitting 68
4.1.3 Analysis in Two and Three Dimensions 75
4.1.4 Statistical Rejections 76
4.2 Gaussian Fitting and Subgroup Analysis 83
4.2.1 Group A Analysis 87
4.2.2 Group B Analysis 87
4.2.3 Additional Gaussian Components 89
4.2.4 Subgrouping 94
4.2.5 Core Structure 94
4.2.6 Summary of Statistical Results 97
4.3 Radio Data 97

4.4 X-ray Data 100
4.5 Gravitational Binding 101
4.5.1 Projected Mass Versus Virial Mass 103
4.5.2 Two-Body Analysis 104

5 Summary And Conclusions **108**
5.1 Summary 108
5.1.1 Group A 109
5.1.2 Group B 109
5.2 Drawing Conclusions 111
5.3 Future Work 113
5.3.1 Current Limitations 113
5.3.2 X-ray Emission and the Sunyaev-Zel'dovich Effect 114
5.3.3 Metallicity and Stellar Population Analyses 115
5.3.4 Computational/Numerical Modeling 115

Appendix **116**
A.1 Literature Summary 117
A.2 New Measurements 120
A.3 Final Catalog 128
A.4 Stellar Data 139

Bibliography **146**

List of Figures

2.1 Spectrum of a galaxy in Abell 154. 9

2.2 Overlayed spectra of a galaxy from Abell 154 and the Andromeda galaxy. . . 10

2.3 Temperature as a function of radius in cooling flow clusters. 24

2.4 Temperature as a function of radius in non-cooling flow clusters. 25

2.5 X-ray intensity as a function of position. 26

2.6 Abell 154 from the POSS-II survey (inverted). 31

2.7 Abell 154 core from the POSS-II survey (inverted). 32

2.8 Einstein X-ray image of Abell 154. 39

2.9 X-ray contour image of the core of Abell 154. 40

3.1 Targets for radial velocity measurements. 45

3.2 FXCOR interactive display. 48

3.3 FXCOR graphical output of a galaxy in Abell 154. 49

3.4 FXCOR graphical output of a star. 50

3.5 Stellar targets. 53

3.6 Galactic radial velocities in Abell 154. 59

3.7 Abell 154 2D histogram. 60

3.8 Abell 154 velocity histogram. 61

4.1 Abell 154 histogram. 63

4.2 Initial 3-σ histogram. 65

4.3 Abell 154 by group. 69
4.4 Histogram of the positions of all 205 galaxies with radial velocity measurements. 70
4.5 Histogram of the positions of galaxies. 70
4.6 Histogram of the positions of Group A galaxies. 70
4.7 Histogram of the positions of Group B galaxies. 70
4.8 Right ascension and declination as a function of radial velocity. 71
4.9 Abell 154 radial velocity histogram by group. 81
4.10 Group A and Group B histograms. 82
4.11 3-σ clipped Dressler-Shectman bubble plot. 84
4.12 Dressler-Shectman bubble plot of Group B galaxies. 85
4.13 Dressler-Shectman bubble plot of Group A galaxies. 86
4.14 Group A histogram. 88
4.15 Group B histogram. 90
4.16 Group B histogram. 91
4.17 Group B double root residual plot. 93
4.18 Group B histogram with subgroups. 96
4.19 Group A map overlay. 98
4.20 Group B map overlay. 99
4.21 Subgroup B1 and Subgroup B2 map. 100
4.22 X-ray emission in Abell 154. 102
4.23 Group A to Group B gravitational binding. 106
4.24 Subgroup B1 to Subgroup B2 gravitational binding. 107

List of Tables

2.1 Typical custer properties. 19

2.2 Typical timescales. 19

2.3 Abell 154 information. 34

3.1 Targets for observation. 44

3.2 Observations at Kitt-Peak National Observatory. 46

3.3 Emission reference spectra. 54

3.4 Literature radial velocity sources. 56

3.5 Literature self-consistency. 58

4.1 KMM and GMM two group analysis. 67

4.2 KMM and GMM three group analysis. 67

4.3 Identified groups. 68

4.4 Statistical tests. 72

4.5 Statistical results. 74

4.6 Group A GMM and KMM results. 87

4.7 Group B, 2 Gaussian GMM and KMM results. 89

4.8 Group B, 3 Gaussian GMM and KMM results. 92

4.9 Subgroup statistics. 95

4.10 Mass estimation. 103

5.1 Group A and Group B characteristics. 112

A.1 Literature radial velocities. 118
A.2 Radial velocities from absorption features. 120
A.3 Radial velocities from emission spectra. 125
A.4 Cross-listing for duplicate measurements. 128
A.5 Radial velocities for Abell 154. 129
A.6 Subgroup membership. 135
A.7 Radial velocities for foreground stars. 140

Chapter 1

Introduction

On the largest observable scales, the universe exists in a filamentary organization of matter and dark matter that is manifested in galaxies, galaxy clusters and superclusters (Geller & Huchra, 1989; Binney & Tremaine, 2008). Galaxy clusters are the largest virialized systems (Sarazin, 2002, 2009; Binney & Tremaine, 2008; Allen et al., 2011; Kravtsov & Borgani, 2012) and the largest clusters are found where the filaments of structure intersect (Springel et al., 2005; Geller & Huchra, 1989).

A typical galaxy cluster will contain hundreds of bright galaxies and thousands of fainter galaxies spread across a region of about $\sim$4 Mpc in diameter (Sarazin, 2009; Kravtsov & Borgani, 2012). Clusters typically have a total mass of $\sim 10^{14}$ – $\sim 10^{15}$ $M_{\odot}$ (Kravtsov & Borgani, 2012; Sarazin, 2009; Binney & Tremaine, 2008), which is distributed into three basic components of a cluster: 1.) stars and galaxies, which are seen in the visible spectrum; 2.) hot intracluster medium (ICM) with temperatures $\sim 10^{7}$ – $\sim 10^{8}$ K, whose radiation can be seen in the X-ray spectrum; and 3.) dark matter, which can only be detected by gravitational influences (Carroll & Ostlie, 2006; Allen et al., 2011; Kravtsov & Borgani, 2012; Sarazin, 1986, 1988). The vast majority of the mass in a galaxy cluster can be found in dark matter (Zwicky, 1933, 1937; Sarazin, 2009). Only a small fraction of the mass is in the ICM, and less than 5% of the cluster mass is found in the stars and galaxies themselves (Binney

& Tremaine, 2008; Sarazin, 2009; Allen et al., 2011; Kravtsov & Borgani, 2012).

1.1 Understanding Galaxy Clusters

Galaxy clusters are at a unique position in the hiearchy of matter in the universe. They exist as the largest and most massive gravitationally bound and potentially relaxed systems (Sarazin, 2009; Allen et al., 2011). They are also the smallest systems that can represent the relative composition of matter and dark matter in the universe (Sarazin, 2009; McNamara & Nulsen, 2007). The dominance of dark matter in a galaxy cluster presents gravity as the driving principle for formation and evolution (Voit, 2005; Kravtsov & Borgani, 2012). The distribution and amount of matter and dark matter in a cluster is the most basic information that is necessary in order to understand a galaxy cluster, and thereby, understand its influence on cosmology and the properties of the universe (Voit, 2005; Allen et al., 2011; Kravtsov & Borgani, 2012).

Galaxies and the ICM trace the potential well of the cluster, which is dominated by the dark matter (Allen et al., 2011; Sarazin, 1988; Binney & Tremaine, 2008). Clusters also provide multiple targets for observation (Allen et al., 2011), and correlations between observations can help to statistically reduce uncertainties and eliminate some systematic effects (Bevington & Robinson, 2003; Leo, 1994).

1.2 Importance of Further Study

Current observations suggest that structure formation occurs through hierarchical merging (Press & Schechter, 1974; Kravtsov & Borgani, 2012; Allen et al., 2011; Sarazin, 1988) where less-massive systems accrete to form more-massive systems over time. However, hierarchical merging is not able to fully explain the existence of the most massive galaxies in cluster cores (Merritt, 1984b, 1985; Dubinski, 1998), and that merging is expected to be less probable in more massive clusters due to a higher velocity dispersion resulting from the deeper

gravitational potential well (Ostriker, 1980).

Several reviews of galaxy clusters also present dark matter as being collisionless (Allen et al., 2011; Sarazin, 1986; Voit, 2005), but recent studies have called this into question, suggesting the possibility of a self-interacting property of dark matter (Williams & Saha, 2011; Kahlhoefer et al., 2014; Koda, 2009). Additionally, there are discrepancies between cosmological models and observations (Voit, 2005; Allen et al., 2011; Kravtsov & Borgani, 2012), and there are still some processes that are not yet understood fully (e.g., Cooling Flows, etc.) (Allen et al., 2011; Peterson et al., 2003; Fabian & Sanders, 2009; Fabian, 2012).

Recent observations of galaxies in clusters have been used to further calibrate models with constraints for formation and evolution, clarify the nature of dark matter and describe the mechanisms responsible for thermal and non-thermal radiation on the largest scales (Allen et al., 2011; Ness, 2012). Additional data is necessary for further advancement.

1.3 Abell 154 and Dissertation Overview

This dissertation is a presentation of a robust analysis of a galaxy cluster that has only been marginally studied previously: Abell 154. This specific galaxy cluster will be examined and its current dynamical status will be analyzed. The morphology of the cluster suggests that the cluster exhibits signs of recent merger activity while also exhibiting some characteristics that would suggest the opposite. The research will include reduction and analysis of previously unpublished data. Correlations between new data and the multi-wavelength data from the literature will be examined. An overall analysis of the data will conclude with a summary of the dynamical status, and the results will provide important evidence for on-going research in dark matter, dark energy, cosmological constraints and the large-scale structure of the universe.

First, the detailed background science and previous information from the literature

is presented in Chapter 2. This includes a thorough literature review and a summary of all of the information, to date, available on Abell 154.

Next, in Chapter 3, the methods used to observe Abell 154 are explored. The methods used to reduce and compile the new observations are presented while paying special attention to the handling of duplicated measurements and the uncertainties of galaxies that have multiple measures. The data are consistently evaluated with "Sanity Checks" to ensure that the data are self-consistent. In the few cases where there are inconsistencies, a description of how we have chosen to move past those inconsistencies is presented.

Then, Chapter 4 provides an analysis of the information as a whole, using various methods that are described therein. In this chapter the cluster and any subgroups in velocity space are examined, as well as spatially along the plane of the sky. There are comparisons to radio and X-ray data provided. There is also an analysis of the potential subgroups to determine their likelihood for current interaction and to define their current dynamical status.

Finally, Chapter 5 summarizes and draws conclusions based on the information that is presented and discusses potential future work. Catalogs of data are presented in the appendices.

Chapter 2

Background

Prior to 1960, Zwicky, Shapley and Abell provided the first analyses of galaxy clusters through their collected works (Abell, 1957, 1958; Shapley, 1933; Shapley & Paraskevopoulos, 1940a; Shapley & Boyd, 1940; Shapley & Paraskevopoulos, 1940b; Shapley, 1944; Zwicky, 1938, 1939, 1942c,b,a, 1950b,a, 1951a,b, 1953, 1956b,a, 1957, 1959). Initial research was limited by the statistically small number of clusters, but was greatly broadened by Abell's catalog (Abell, 1958) and Zwicky's 6-volume catalog (Zwicky et al., 1961-1968). The large number of clusters that are identified in these works suggest that galaxy clusters are fundamental condensations of matter in the universe (Abell, 1958; Rood & Sastry, 1971). This idea of matter, in the form of galaxies, as the building blocks of clusters became the underlying hypothesis of large-scale structure formation through hierarchical merging (White & Rees, 1978; Press & Schechter, 1974).

2.1 Hierarchical Merging

Observations, such as the cosmic microwave background, suggest that matter in the early universe was nearly uniform with a nearly isotropic distribution, and that matter is evolving into filamentary structures of dark matter, galaxy clusters and groups of galaxies, which are observed at later times. One explanation of this evolution is through the process of

hierarchical merging (Press & Schechter, 1974; White & Rees, 1978; Binney & Tremaine, 2008; Sarazin, 2002; Kravtsov & Borgani, 2012). A brief synopsis of the theory is presented here: Within the initial isotropy, slight fluctuations in mass density perturbed matter from a nearly equilibrium condition. The fluctuations were more frequent on the smallest mass scales, resulting in many regions of slightly enhanced density. Each density enhancement acted as a local center of mass, toward which the distribution of local matter would gravitationally collapse, creating many small clumps of matter. Over time, small clumps then collapse through their mutual self-gravitation to form the earliest stars and galaxies. On longer time scales, galaxies will accrete to form groups of galaxies, which accrete on even longer time scales, to form galaxy clusters as the process continues towards progressively more massive objects.

As this process continues, objects become greater in mass, resulting in a stronger gravitational influence. The increased gravitational potential well of the objects improves the chances of objects interacting and, eventually, becoming gravitationally bound (Ostriker & Tremaine, 1975). In this way, it is expected that interaction probability will correlate with increased mass. However, too much mass can also have the opposite effect by inhibiting the merging processes between galaxies due to an excessive velocity differential (Ostriker, 1980). However, it is expected this to be less significant in cluster-cluster interactions where energy can be dissipated through a number of mechanisms, such as ram-pressure stripping, dynamical friction, two-body galaxy interactions, etc. (Sarazin, 2002).

2.2 Cluster Properties

Analyses of galaxy clusters evolved throughout the decades following the Abell (1958) catalog, becoming more robust with the onset of technological advances. Early studies were focused on richness, position and – for nearby galaxy clusters – surface brightness. Earliest analyses of galaxy clusters traditionally assumed that each cluster was a spherical distribu-

tion of galaxies, and that interactions between clusters were rare (Zwicky, 1956b,a; Seyfert, 1948; Abell, 1958; Carroll & Ostlie, 2006). Later studies began to examine the morphology of galaxy clusters which suggested that dynamics and encounters were much more common than traditionally assumed (Struble & Rood, 1982; Rood & Sastry, 1971; Bautz & Morgan, 1970; Bahcall, 1977). The dynamical state of a cluster is analyzed by the distribution of galaxies, gas and/or dark matter of the cluster, each of which contributes to the appearance of underlying complex structures, or substructure (Geller & Beers, 1982). While determining actual cluster membership is non-trivial, foreground and background galaxies that are along the line of sight of the cluster (interlopers) are occasionally identified (Sarazin, 1988, 1986). Existence of interlopers and the appearance of multiple locii in either the right ascension and declination positions or the radial velocities of galaxies of several clusters suggested that clusters could come with varying amounts and orientations of substructure (van den Bergh, 1961; Rood & Sastry, 1971; Geller & Beers, 1982; Sarazin, 1986).

2.2.1 Cosmic Distances

Galaxy clusters reside at distances that are beyond the direct methods of measurement using geometry. Instead, indirect methods to estimate distances, or relative distances, to extragalactic objects are used. For relative distances of galaxy clusters, there are several kinds of distance scaling relations, including the Faber-Jackson Relation (Faber & Jackson, 1976), Tully-Fisher Relation (Tully & Fisher, 1977), Fundamental Plane Relation (Vogt et al., 1996; Bender et al., 1996), the Sunyaev Zel'dovich Effect (Sunyaev & Zeldovich, 1969), among others, including general surveys of distance measures (Jacoby et al., 1992). Distances to nearby galaxy clusters can use Type Ia Supernovae as standard candles in order to determine the distance (Carroll & Ostlie, 2006; Binney & Tremaine, 2008). A standard candle is method of determining distance by exploiting the difference between observed and intrinsic brightnesses. Intrinsic brightness can be ascertained in Type Ia supernovae by using the object's change in brightness over time (lightcurve) and correlating it with an empirically

derived relationship between the peak of the lightcurve and the absolute magnitude (Carroll & Ostlie, 2006; Binney & Tremaine, 2008). While these relationships are used in much of the literature, none of these methods will be used directly in this dissertation.

Instead of using these scaling relations and standard candles, relative distances are determined using the apparent recessional velocities of the galaxies through Hubble's Law (Hubble, 1929),

$$d = \frac{v}{H_0}, \tag{2.1}$$

where v is the apparent recessional velocity, d is the relative distance to the object, and H_0 is the constant of proportionality, called the Hubble Constant, that represents the present expansion rate of the universe. H_0 is currently measured at 74.2 ± 3.6 km s^{-1} Mpc^{-1} (Riess et al., 2009).

The apparent recessional velocity, v, is determined through the analysis of the spectrum of the galaxy. A spectral shift, z, of a spectrum can be measured as a fractional change between the observed and rest wavelengths for specific absorption or emission features by

$$z = \frac{\lambda_{\text{obs}} - \lambda_{\text{rest}}}{\lambda_{\text{rest}}}, \tag{2.2}$$

where λ_{obs} is the observed wavelength of a spectral feature and λ_{rest} is the rest wavelength of the same spectral feature. A rest wavelength is the wavelength of a spectral feature from a stationary – relative to the observer – source. A spectral feature is any transition of an electron to a higher energy state (by absorption of light) or to a lower energy state (by emission of light). The wavelength of light corresponds to the energy, E, of the transition,

$$E = \frac{hc}{\lambda}, \tag{2.3}$$

where h is Planck's Constant, $6.626 \times 10^{-34} Js$, c is the speed of light in a vacuum and λ is the wavelength of the photon that is absorbed or emitted. The speed of light in a vacuum

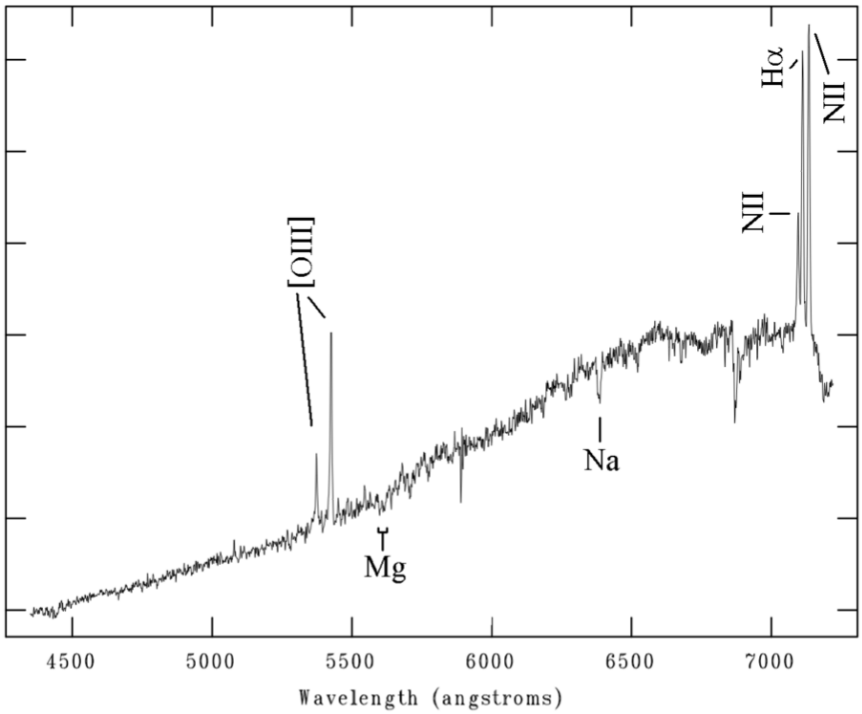

Figure 2.1: Spectrum of a galaxy in Abell 154. The spectrum of this example galaxy shows both emission and absorption features that can be used to calculate recessional velocity. The horizontal axis shows wavelength in angstroms and the vertical axis represents the intensity of the spectrum.

is defined as a constant with the value of $299792458\,m\,s^{-1}$, but for the purposes of this dissertation we will use the rounded figure of $3.0 \times 10^8\,m\,s^{-1}$. These transitions only occur at discrete energies, which are specific to the transitions that are available in each atom. An example of a galaxy spectrum that contains both emission and absorption features is presented in Figure 2.1.

An example of the spectral shift of sodium and magnesium absorption features is given in Figure 2.2, in which a galaxy in Abell 154 (in black) and the Andromeda galaxy (in green) are compared. Andromeda is a nearby galaxy, but the galaxy from Abell 154 is much more distant. The redward shift of the magnesium and sodium absorption features from Andromeda's (green) spectrum to Abell 154's (black) spectrum clearly exemplifies the effect of a spectral shift.

The spectral shift is then used to calculate the apparent recessional velocity of the object relative to the speed of light, using

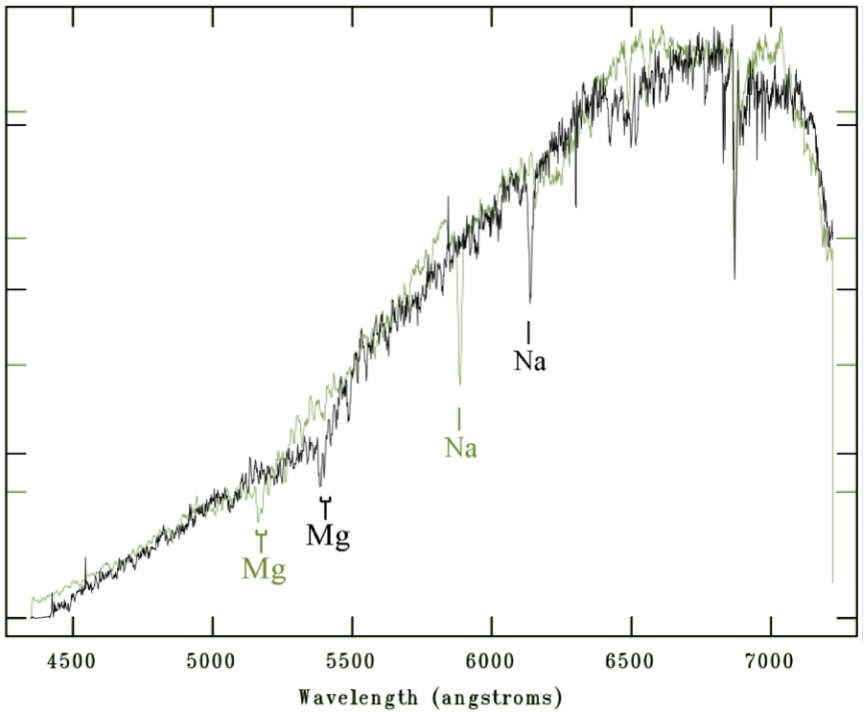

Figure 2.2: Overlayed spectra of a galaxy from Abell 154 and the Andromeda galaxy. Abell 154 galaxy is shown in black. Andromeda galaxy is shown in green. The horizontal axis shows wavelength in angstroms and the vertical axis represents the brightness of the spectrum. The two strong absorption features of the magnesium triplet and the sodium doublet are indicated and labeled for both spectra. The redward shift of the more distant Abell 154 galaxy is evident and is related to the apparent recessional velocity of the galaxy.

$$z + 1 = \sqrt{\frac{1 + \frac{v}{c}}{1 - \frac{v}{c}}}, \tag{2.4}$$

where v is the apparent recessional velocity of the object, c is the speed of light and z is the shift of the spectra relative the the rest wavelength as shown in Equation 2.2, which becomes

$$v = c\frac{(z+1)^2 - 1}{(z+1)^2 + 1}, \tag{2.5}$$

when solved for v. For low z values, an approximation of Equation 2.4 can be used. These approximations are:

$$z \approx \frac{v}{c}, \tag{2.6}$$

$$v \approx cz, \tag{2.7}$$

where v represents the apparent recessional velocity of the object and c represents the speed of light. For this dissertation, the approximations (given in Equations 2.6 and 2.7) are used exclusively since the cluster's z value is small ($z < 0.08$). This approximation results in a maximum of 4% deviation between the velocities obtained from Equation 2.5 versus Equation 2.7 for the most distant galaxies of Abell 154's main locus of data points in velocity space. It is also a recommended convention to represent radial velocities using the approximations in Equations 2.6 and 2.7, rather than the relativistic corrections in Equations 2.4 and 2.5 (Hogg, 1999; Fairall, 1992).

The apparent velocity that is obtained by Equation 2.7 is due to a spectral shift that has two potential causes. The first cause is the physical motion of the object. This kind of spectral shift is known as a Doppler shift. The detection of the physical motion of a galaxy by the Doppler shift is limited to radial motion, or motion that is only in the dimension of the observer's line of sight. A galaxy that moves towards the observer will result in a

blue-ward shift whereas a galaxy moving away from the observer would result in a red-ward shift in the spectrum.

The second cause of spectral shift is from the expansion of the universe. This effect, which is known as cosmological spectral shift, occurs due to the increasing distance between observer and object while the light is en route. It is not caused by the physical motion of the galaxy. Cosmological spectral shift is always red-ward and is proportional to the distance between the observer and the object since the universe is uniformly, isotropically expanding. This is the basis for Hubble's Law (Equation 2.1) and makes up the most substantial portion of the spectral shift for galaxies and galaxy clusters that are located at a similar distance as Abell 154. While this means that the spectral shift of a galaxy is mainly not due to motion, it is still conventional to measure the redshift of galaxies and clusters in terms of apparent recessional velocity as calculated through Equation 2.7.

Member galaxies of a galaxy cluster are expected to be mutually bound and move about a collective center of mass (Sarazin, 2009; Allen et al., 2011). Relative to the center of mass, galaxies have varying individual motions, called peculiar motion, as well as varying distances from the cluster center. If the variation of member galaxy motion and location is sufficiently random with respect to the cluster center and if the number of cluster members is sufficiently large, an average of the apparent recessional velocities of the cluster members will minimize the contribution of peculiar motion on the apparent recessional velocity of the cluster as a whole. While the average apparent recessional velocity is impacted less by galactic motion, the cluster may still have a collective physical motion leading to a contribution to spectral shift by the Doppler effect. While these effects cannot be removed, the average apparent recessional velocity, through Hubble's law, is the distance estimator that will be used in this dissertation.

2.2.2 Cluster Mass

The mass of a galaxy cluster shapes the potential well, drives the evolution of the cluster and defines the dynamics within a cluster (Rood, 1981; Sarazin, 1986). The influence of cluster mass on cluster members impacts the environment and evolution of individual galaxies (Beers et al., 1982; Beers & Geller, 1983). Cluster galaxies orbit the collective center of mass, but this is not necessarily a uniform or isotropic motion (Sarazin, 1986). Additionally, cluster mass influences the likelihood of merger events between clusters, making mass one of the most important properties to analyze in a cluster.

Mass for galaxy clusters were initially calculated as the aggregate mass of individual member galaxies, where the mass of each galaxy was found by using galactic mass-to-light ratios. However, the total mass was known early on to be unreliable for a gravitationally bound cluster (Zwicky, 1933; Navarro et al., 1995; Faber & Gallagher, 1979; Sarazin, 1986; Binney & Tremaine, 2008). The aggregate mass would have been too small for the size of the cluster and would result in a galaxy cluster that is unbound (Binney & Tremaine, 2008; Sarazin, 1986). The speed at which unbound clusters would disperse is not consistent with the predominance of clustering that is observed visually, nor with so many clusters that appear regular and relaxed (Sarazin, 1986).

Since that time, it was discovered that the hot gas of the ICM in rich clusters contains more mass than the the total luminous matter in galaxies (Sarazin, 2002; Forman & Jones, 1990; Binney & Merrifield, 1998), and that clusters are gravitationally dominated by dark matter (Sarazin, 2002; Zwicky, 1933). Both considerations contribute to the resolution of the discrepancy when using standard mass-to-light relationships. While specialized mass-to-light ratio for clusters can provide a general estimate of mass for a cluster, new approaches have also been developed to probe the mass distribution of clusters (Binney & Tremaine, 2008). The following four approaches are the most commonly used and are independent of the luminosity of the galaxies themselves (Binney & Tremaine, 2008):

- **Gravitational Lensing** – According to Einstein's General Theory of Relativity, light

passing near a massive object will follow the curvature of spacetime. By examining the distortion and multiplicity of images, as well as the delay of synchronous events, the mass that has created these effects can be estimated (Dyer & Roeder, 1976; Zwicky, 1937; Einstein, 1911). This approach to analyze mass will not be used within this dissertation.

- **X-ray Emissivity** – Hot intracluster gas, which traces the gravitational potential well of the galaxy cluster, radiates in the X-ray spectrum. The peak and slope of the X-ray spectrum indicates the steepness of the gravitational potential well (Sarazin, 1986; Forman & Jones, 1990; Bahcall, 1977). This will be examined in greater detail along with X-ray data and cooling flows in Section 2.3.2.

- **Sunyaev-Zeldovich Effect** – Mass is determined by analyzing the reduction in the Cosmic Microwave Background energy density due to inverse Compton up-scattering of photons by electrons (Myers et al., 1997; Birkinshaw, 1999). Inverse Compton scattering is where photons are absorbed by electrons and are then re-emitted at higher energies, slowing the electron (Sarazin, 1988). This approach to analyze mass will not be used within this dissertation.

- **Statistical Analyses** – Mass can also be indirectly inferred by a statistical analysis of the positions and radial velocities of the galaxies in the cluster. Galaxies in a relaxed cluster trace the potential well of the cluster, and the positions and radial velocities of a large number of galaxies can be used to calculate the mass of the cluster using the Virial theorem (see Section 2.3.1) (Binney & Tremaine, 2008). It can also be quickly estimated and compared by observing the velocity dispersion across the cluster members (Bird, 1994; Pinkney et al., 1996; Dressler & Shectman, 1988; Heisler et al., 1985). This approach will be the primary focus when estimating mass.

Each of these approaches can constrain the value and uncertainty of the overall mass of the cluster. Congruency between two or more of these can confirm the determined cluster

mass. For this dissertation, the X-ray emissivity from the literature are used to validate the estimates of mass that are obtained from the statistical analyses.

The gravitational influences on material in a galaxy are important for understanding the motion and timescales involved in cluster dynamics. In the next section, the various time scales are discussed and how they impact cluster dynamics, including cluster mergers.

2.2.3 Timescales

As the cluster evolves, the properties of the cluster will change over time. Understanding the timescales of cluster processes is important in order to analyze the dynamical status of a cluster. The size of a galaxy cluster requires a significant amount of time to relay information from one side to the other. Therefore, time scales are measured most effectively on the order of billions of years (Gyr). There are several different timescales relevant to galaxy clusters, and each of these will impact the analysis and interpretation of the findings (Bothun, 1998; Binney & Tremaine, 2008; Carroll & Ostlie, 2006):

- **Hubble Time** – The expansion age of the universe is called a Hubble time. Hubble time is related to the Hubble Constant by the equation

$$t_{\rm H} = \frac{1}{H_0}, \tag{2.8}$$

  where H_0 was previously given in Equation 2.1. Most recent estimates concur that the Hubble Time should be $t_{\rm H} \approx 13.7$ Gyr (Riess et al., 2009).

- **Sound Crossing Time** – The time required for a vibration to propagate from one side of the cluster to the other is the sound crossing time (Binney & Tremaine, 2008; Carroll & Ostlie, 2006),

$$t_{\rm sound} \approx \frac{R}{c_{\rm s}}, \tag{2.9}$$

  where $t_{\rm sound}$ is the time it takes for a vibration to traverse the cluster, R is the radius

of the cluster, and $c_{\rm s}$ is the speed of the sound in the cluster. The speed of sound is related directly to the characteristics of the cluster. For example, if the hot ICM is assumed to be an ideal gas, then the speed of sound would be characterized as (Binney & Tremaine, 2008),

$$c_{\rm s} \propto \sqrt{\frac{k_{\rm B}T}{m}}, \tag{2.10}$$

where $k_{\rm B}$s is the Boltzmann constant ($k_B = 1.38 \times 10^{-16}\, erg\, K^{-1}$), T is the temperature of the cluster in Kelvin and m is the mass of the gas in grams.

- **Crossing Time** – The time required for an object to travel from one side of the cluster to the other side is the crossing time (Sarazin, 1986; Bothun, 1998; Binney & Tremaine, 2008),

$$t_{\rm cross} \approx \left(\frac{r}{\sigma_{\rm cl}}\right) \text{Gyr}, \tag{2.11}$$

where radius, r, is measured in megaparsecs and the velocity dispersion for the cluster, $\sigma_{\rm cl}$, is given in thousands of kilometers per second. In accordance with this equation, a cluster with a larger velocity dispersion will take less time for an object to cross since the higher velocity dispersion implies a larger mass and therefore a larger acceleration on the traversing object.

- **Two-body Relaxation Timescale** – The time that is required for the total energy to be distributed among all members of the cluster through two-body interactions, including dynamical friction, is the two-body relaxation timescale (Binney & Tremaine, 2008; Sarazin, 1986; Forman & Jones, 1982; Bothun, 1998),

$$t_{\rm relax} \approx \frac{1}{8}\frac{N}{\ln N} t_{\rm cross}, \tag{2.12}$$

where $t_{\rm cross}$ represents the crossing time of the cluster as shown in Equation 2.11 and N represents the number of particles or galaxies that are involved in two-body interactions. These interactions result in the equipartition of energy throughout the system

through mass segregation (Binney & Tremaine, 2008). More massive objects migrate towards the core, transferring potential energy to less massive objects as increased velocity. The increased velocity results in the less massive objects migrating outwards (Sarazin, 1986; Forman & Jones, 1982). In rich clusters, this may be the mechanism responsible for the creation of cD-type galaxies that are often found in the cores, or gravitational centers, of the richest clusters (Sarazin, 1986). This timescale should be much longer than most others for rich clusters since it requires the interaction of nearly all objects in the cluster.

Dynamical friction occurs when an object travels through a mass distribution, resulting in a deceleration (Chandrasekhar, 1942, 1943; Binney & Tremaine, 2008). To summarize this concept, consider an isotropic, uniform, infinite distribution of material and a massive object that is traveling through it. The massive object attracts the distribution in all directions, but the motion of the object results in material behind the object experiencing a greater cumulative effect over time. This is because the attraction is greatest at periapsis, which has already occurred for matter behind the object, but has not yet occurred for matter in front of the object. This causes the matter distribution to concentrate in a gravitational wake, which is aligned directly behind the object in motion. The concentration of matter behind the object results in gravitational influence that is greater than the material that is still spread out in front of the object, causing the object to slow. The effect of this force is similar to drag or kinetic friction since it will always oppose the direction of the object's motion.

- **Collapse Timescale** – The time required for gravitational dissipative effects that bring a cluster into a quasi-relaxed condition through collisionless interactions with the collective gravitational potential is called the collapse timescale (Sarazin, 1986; Lynden-Bell, 1967),

$$t_{\text{coll}} \approx \sqrt{\frac{R^3}{GM}} \approx \sqrt{\frac{1}{G\rho}}, \tag{2.13}$$

where R is the radius of the cluster in meters, G is the gravitational constant, $6.67 \times 10^{-11}\, N\, m^2\, kg^{-2}$, M is the cluster mass in kilograms, and ρ is the density of the cluster in kilograms per cubic meter. It is sometimes referred to as violent relaxation (Sarazin, 1986; Bothun, 1998; Binney & Tremaine, 2008; Lynden-Bell, 1967). The end result of this time scale is a cluster that is equipartitioned in velocity space (i.e. exhibits a nearly constant velocity dispersion) throughout the cluster (Sarazin, 1986), but unlike the two-body relaxation timescale, there is no mass segregation involved due to the rapid nature of processes that would cause violent relaxation (Sarazin, 1986). Two examples of conditions where this timescale is likely applicable is (1) spherical collapse of a distribution, especially from large distances, and (2) a head-on collision between two clusters of equal mass. The collapse timescale tends to be less than a few crossing times (Sarazin, 1986), see Equation 2.11.

Based on relative differences in timescale magnitudes between the collapse timescale and the two-body relaxation timescale (see Table 2.2), it is expected that merger activity in the recent past may exhibit equipartitioning in velocity space, but will not have had enough time to relax significantly through two-body interactions.

- **Cooling Time** – The time necessary for the temperature of the cluster to cool significantly is called the cooling time (Bothun, 1998),

$$t_{\text{cool}} \approx 8.5 \times 10^7 \frac{\sqrt{T}}{n_e}\, yr, \tag{2.14}$$

where n_e is the number density of particles in particles per cubic centimeter and T is the temperature of the gas in 10^8 K. This also represents the time that must pass before a cooling flow is expected to have fully developed (Bothun, 1998). See Section 2.3.2 for more information on cooling flows. This should be far longer than a Hubble time for most clusters (Sarazin, 1986; Bothun, 1998). If the cooling time for a cluster is calculated to be longer than a Hubble time, it is unlikely to exhibit a cooling flow

Property	Value
Radius	R = 1 Mpc
Dispersion	$\sigma_{\rm cl} = 1000$ km s^{-1}
Galaxies	N = 1000
Mass	M = 10^{15} M$_\odot$
Temperature	T = 10^8 K
Density	$n_e = 10^{-3}$ $\frac{particles}{cm^3}$

Table 2.1: Typical cluster properties. This table provides several example values for rich clusters. These values will be used to calculate timescales, the results of which can be found in Table 2.2.

Timescale	Value
$t_{\rm cross}$	1 Gyr
$t_{\rm relax}$	18.1 Gyr
$t_{\rm coll}$	0.469 Gyr
$t_{\rm cool}$	85 Gyr

Table 2.2: Typical timescales. This table gives the calculated timescales based on the properties in Table 2.1 and the timescales described in 2.2.3. This information can be used to compare the relative timescales for the characteristics that are expected for a rich cluster. Recall that a Hubble time, $t_{\rm H}$, is 13.7 Gyr.

phenomenon (Sarazin, 1986; Bothun, 1998).

All of these timescales depend on the properties of the cluster or clusters that are being analyzed. Many of the time scales will vary based on only a few properties. As an example, Table 2.1 provides the values for a typical rich cluster, from which each of these time scales can be calculated. Typical time scales of rich clusters based on the values in Table 2.1 are presented in Table 2.2.

2.3 The Relaxed Cluster

A relaxed cluster is defined as a cluster that is in virial equilibrium (see Section 2.3.1) with equipartion of energy between galaxies. While this could be achieved through two-body interactions over a long period of time, the actual processes leading to relaxation may have been a combination of several kinds of interactions or even a hierarchy of interactions, which allow for some clusters to reach this state within a Hubble time (Sarazin, 1988; Forman & Jones, 1982). Relaxed clusters are expected to exhibit several properties indicative of the processes leading to relaxation. While each property, alone, cannot prove that the cluster is relaxed, a confluence of these signatures is evidence that can be used to quantify the likelihood of the cluster's dynamical status. Signatures of a relaxed cluster may include:

- Symmetric, Gaussian-like distribution of the apparent recessional velocities of galaxies

(Dressler & Shectman, 1988; Bird, 1994; Beers et al., 1990; Ashman et al., 1994).

- Smooth, azimuthally symmetric distribution in right ascension and declination that decreases in number density as a function of cluster radius (Lee, 1979; Pinkney et al., 1996; Rhee et al., 1991).

- ICM temperature that is either (1) low overall ($\lesssim 10^7$ K) or (2) has a core temperature as a function of cluster radius (temperature profile) that increases with radius significantly, then decreasing towards larger radii. The latter is a likely indicator of a cooling flow (see Section 2.3.2) (Peterson et al., 2003; Fabian, 1994; Sarazin, 1986).

- A strong, steep X-ray peak which is a likely indicator of a cooling flow (see Section 2.3.2) (Donahue et al., 2006; Bothun, 1998; Fabian et al., 1991; Fabian, 1994; Fabian & Sanders, 2009; Fabian, 2012).

- No extended radio emission features, especially in conjunction with strong radio point sources (Feretti & Giovannini, 1994; Owen & Ledlow, 1997; Sarazin, 2002).

The first two will be examined directly through observations, but for the final three signatures, findings from the literature will be presented later in this chapter. Data obtained from the literature will also be used for analysis in Chapter 4.

2.3.1 Distributions

In a relaxed cluster, the galaxy distribution trace the potential well of the cluster with an increasing number density towards the core (Kaiser, 1984). A frequency distribution in velocity, of a large number of galaxies of a cluster, is expected to be approximately Maxwellian as a function of cluster radius, which is a Gaussian function when viewing along the line of sight to the cluster (Sarazin, 1988; Bahcall, 1999). A one-dimensional Maxwellian distribution of velocities in a cluster is (Binney & Tremaine, 2008)

$$f(v) = \frac{1}{\sigma_{\rm sd}\sqrt{2\pi}}\, e^{-\frac{v_{\rm p}^2}{2\sigma_{\rm sd}^2}}, \tag{2.15}$$

where $f(v)$ represents the fractional distribution of peculiar velocities in one dimension (along the line of sight), $v_{\rm p}$ represents the peculiar velocity of a galaxy and the $\sigma_{\rm sd}$ represents the standard deviation of the velocity distribution, which is typically the same as $\sigma_{\rm cl}$ given in Equation 2.11 previously.

In addition to two-body relaxation, violent relaxation would result in equipartition in velocity space, leading to the appearance of a Gaussian distribution as well (Bahcall, 1999; Sarazin, 1988). A Gaussian distribution is also known as a normal distribution, which represents a cluster of objects that are randomly distributed about an average value with a standard deviation (Bevington & Robinson, 2003). A Gaussian distribution is (Bevington & Robinson, 2003; Binney & Tremaine, 2008)

$$f(v) = \frac{1}{\sigma_{\rm sd}\sqrt{2\pi}}\, e^{-\frac{(v-\bar{v})^2}{2\sigma_{\rm sd}^2}}, \tag{2.16}$$

where $\bar{v}$ represents the average velocity and peak in a Gaussian distribution, v represents the apparent recessional velocity, and $\sigma_{\rm sd}$ represents the standard deviation of the distribution. A deviation from a Gaussian appearance could indicate substructure exists, and it may also indicate the location or form of potential substructure. Deviation from the Gaussian fit provides a starting point for an analysis of the dynamical status of the cluster, and it is used to define potential groups within the cluster. As it can be seen, the 1-dimensional Maxwellian in Equation 2.15 is identical to the Gaussian distribution shown in Equation 2.16, except for the Gaussian distribution is relative to the observer (v represents apparent recessional velocity and $\bar{v}$ represents the recessional velocity of the cluster as a whole), but the Maxwellian 1-dimensional equation is relative to the center of motion ($v_{\rm p}$ represents peculiar velocity).

Virial Theorem

A cluster that is in a self-gravitating state will ultimately conform to the viral theorem, where the energy of the system is characterized by

$$2K + W = 0, \tag{2.17}$$

where the K and W values represent the kinetic energy and the gravitational potential energy, respectively, of the matter that constitutes the cluster. Since this is the result of the conservation of energy in a self-gravitating system, Equation 2.17 applies to the ICM and galaxies, alike, and is also believed to apply to the dark matter of the cluster (Austin, 2008; Harvey et al., 2015).

In a relaxed state, the ICM will exist in hydrostatic equilibrium where the outward gas pressure balances the inward force of gravity, which is a consequence of the virial theorem. As the ICM cools through radiation, the gas will lose kinetic energy. Loss of kinetic energy will cause a decrease in gas pressure resulting in collapse of the ICM until regaining hydrostatic equilibrium (Sarazin, 1986; Binney & Tremaine, 2008).

For a relaxed cluster, galaxies of the cluster should exhibit azimuthal symmetry and smooth distributions in right ascension and declination, as well as a Gaussian-like distribution in velocity space, as a result of the virial theorem. However, the development of symmetry may occur on multiple timescales. If relaxation is mostly due to two-body interactions (long timescales), mass segregation is expected to have occurred and equipartitioning of energy within the system. If relaxation is mostly due to violent relaxation (short timescales), equipartitioning of velocities is expected and a nearly uniform velocity dispersion would be present. In both cases, symmetry is developed, so a significant deviation from symmetry may be an indicator of potential substructure.

2.3.2 Cooling Flows and X-ray Emission

A galaxy cluster's hot ICM radiates with a temperature of $\sim 10^8$ K, peaking in the X-ray region of the spectrum. The radiation is primarily from thermal free-free collisions, which is a thermal process commonly called *bremsstrahlung*. Bremsstrahlung means "braking radiation", which is an appropriately descriptive name for the emission of a photon as a result of an unbound electron decelerating due to passing near a positive ion, such as a proton (Carroll & Ostlie, 2006). The electron loses kinetic energy, equivalent to the photon's energy, resulting in the overall loss of kinetic energy from the gas to radiation. X-ray radiation, therefore, dissipates kinetic energy and thereby reduces temperature of the gas over time. Due to the nature of free-free collisions, the radiation occurs more frequently in regions of higher particle number density.

The ICM exists in hydrostatic equilibrium so that the densest regions of the gas are located at the core where the gravitational pressure of the gas is highest. The higher density of gas results in a higher outward gas pressure, balancing the inward gravitational force. This higher density also results in a higher rate of radiation due to free-free interactions. The higher radiation results in a faster energy loss rate at the innermost regions of the ICM. Density is believed to increase exponentially towards the core (Sarazin, 1988; Binney & Tremaine, 2008), and the energy loss rate through radiation is proportional to the square of the number density of the electrons in the gas (Carroll & Ostlie, 2006; Binney & Tremaine, 2008; Sarazin, 2002), resulting in a radiation rate that increases exponentially near the core (Binney & Tremaine, 2008; Carroll & Ostlie, 2006; Sarazin, 1986, 2002; Donahue et al., 2006). The energy loss rate means that the core will lose kinetic energy much faster than other parts of the cluster, creating a decrease in temperature near the core.

The higher radiation rate at the core of the ICM means that the cooling time for the gas near the center will be shortest. After about a cooling time, a cool core will be observable in the temperature profile (compare Figure 2.3 and Figure 2.4). As the core of the ICM cools, gas pressure support of the intracluster gas reduces and the intracluster gas collapses inward.

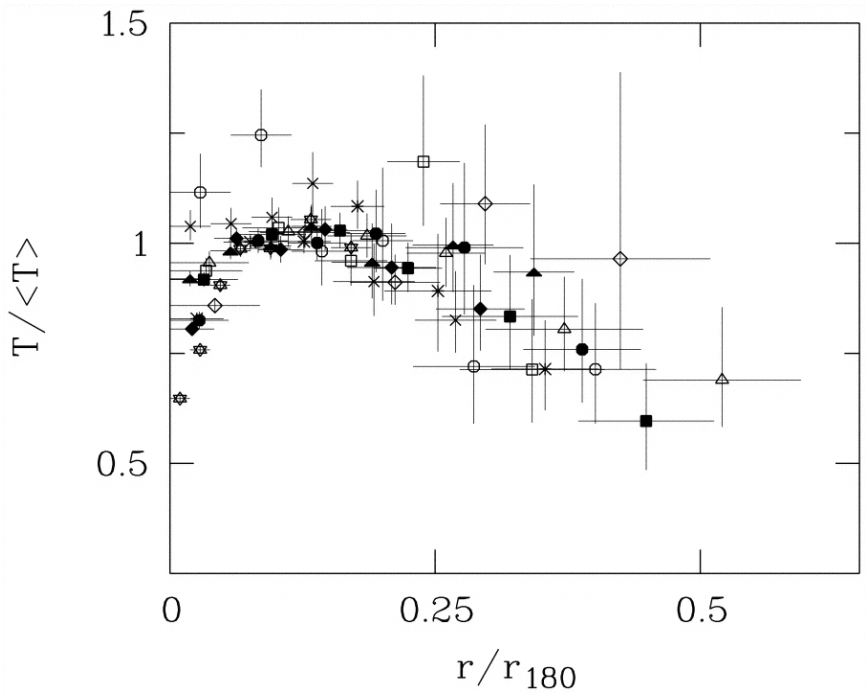

Figure 2.3: Temperature as a function of radius in cooling flow clusters. Scaled temperature as a function of scaled radius. Radius for each measurement is scaled relative to the virial radius (R_{180}). The lowered temperature nearest the core indicates the existence of a cool core (De Grandi & Molendi, 2002).

The collapse of the material increases the density, which results in exponential increase in radiation rate, especially at the core of the ICM where the density is the highest. The flow of material inward, toward the center of mass, is called a cooling flow.

The relationship between temperatures and radius from the center of the cluster can be seen in Figures 2.3 and 2.4. These figures give scaled temperature values as measured across several scaled radial locations for several clusters (De Grandi & Molendi, 2002). The horizontal axes of these figures are radius as scaled relative to the virial radius of the cluster (for these clusters, it is where the overdensity contrast factor is roughly ~ 180 times the mean background density (De Grandi & Molendi, 2002; Kravtsov & Borgani, 2012)), and the vertical axes are temperatures as scaled relative to total average temperature within the virial radius. Figure 2.3 shows the appearance of a cooling core as temperatures decline on the left side of the plot. This is in direct contrast to Figure 2.4 which shows non-cooling flow clusters that generally have flat temperature profiles near the core. It should be noted that the temperature of the gas is based on the peak wavelength of the X-ray spectrum.

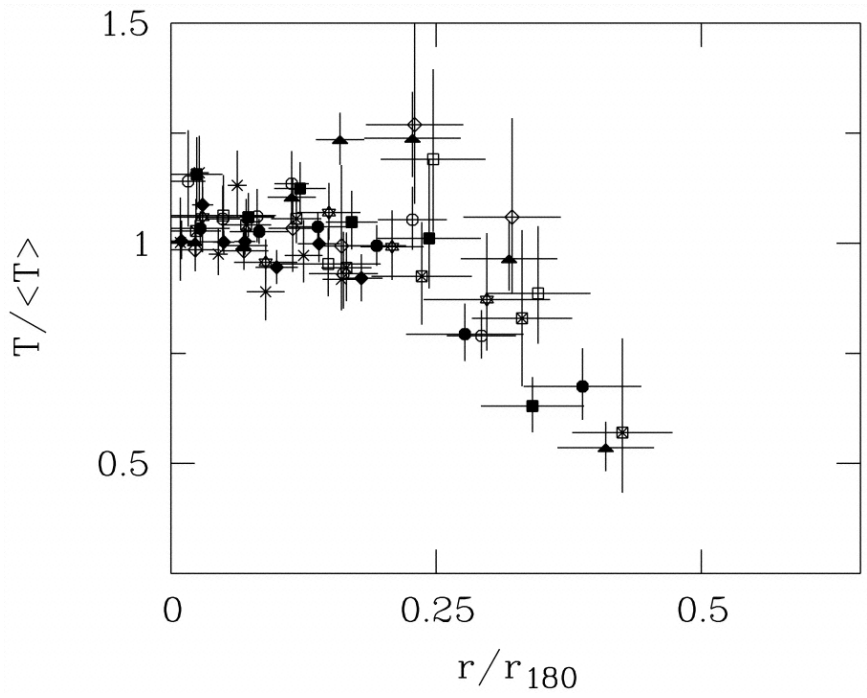

Figure 2.4: Temperature as a function of radius in non-cooling flow clusters. Scaled temperature as a function of scaled radius. Radius for each measurement is scaled relative to the virial radius (R_{180}). The temperature curve appears to be flat nearest the cluster core (De Grandi & Molendi, 2002).

X-ray intensity also shows a difference between cooling flow clusters and non-cooling flow clusters. As stated previously, the cooling flow causes an increase in particle density, which increases the X-ray intensity exponentially. Figure 2.5 clearly shows this difference between a cooling-flow cluster on the left (Abell 478) and a cluster on the right which does not exhibit the cooling-flow phenomenon (Abell 1656, the Coma Cluster) (Fabian & Sanders, 2009).

Cooling flows in rich clusters are believed to take several billion years to become observable (Fabian, 1994). Since the cooling flow phenomenon appears the same for many clusters, it would suggest that it is an approximate steady state (Fabian, 1994; Donahue et al., 2006). Any addition of heat through interaction with other clusters could interrupt this process. Therefore, a cooling flow is believed to be evidence that the cluster is in a dynamically mature state and that there has been no recent activity. The cooling flow phenomenon is an area of on-going research (see Peterson et al., 2003 and Fabian, 2012 and the references therein for a summary).

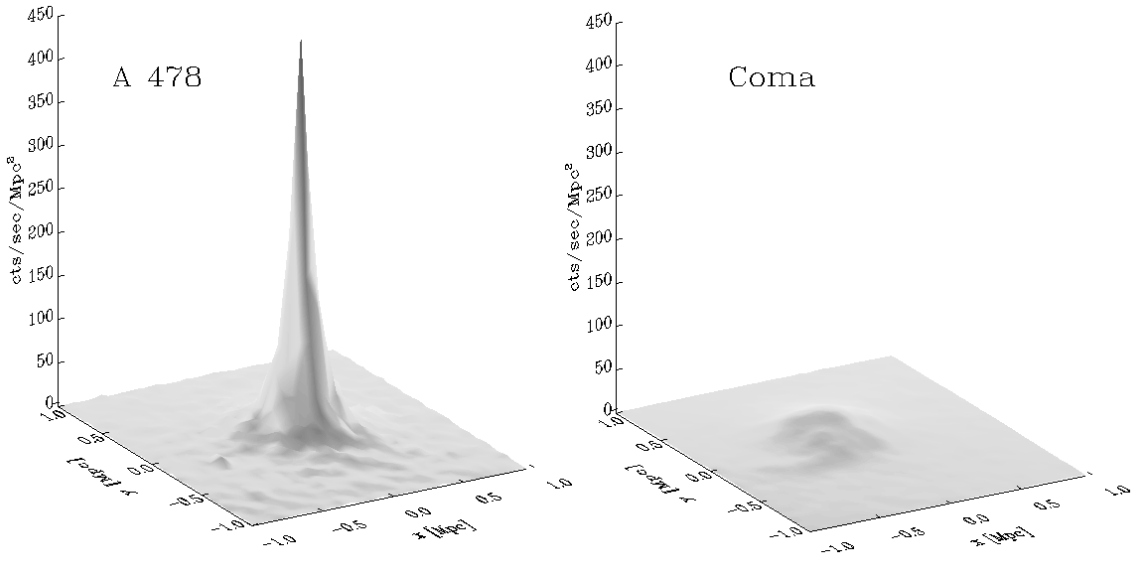

Figure 2.5: X-ray intensity as a function of position. The figure presents a comparison of X-ray intensity between a cluster that exhibits a cooling flow phenomenon (left) and one that does not (right) (Fabian & Sanders, 2009).

2.4 The Merging Cluster

Cluster mergers are the most energetic events in the universe (since the Big Bang), releasing gravitational potential binding energy of $\gtrsim 10^{64}$ ergs in a large-mass, major merger event (Sarazin, 2002). In congruence to the literature (Binney & Tremaine, 2008; Shankar et al., 2015; Sarazin, 2002), the major and minor mergers are defined as follows: When mergers involve clusters of similar mass (where the less massive cluster is no less than 30% of the mass of the other cluster), it is defined as a major merger. A minor merger is defined as a lower-mass cluster or group infalling on a cluster that has a much larger mass (where the less-massive cluster is less than 30% of the mass of the larger cluster).

A merger event is assumed to begin with galaxies existing at their largest separation distance. This initial distance, determined by the Big Bang and the inflationary period of expansion, is not an infinite distance. However, the initial distance is much larger than the relative sizes of the clusters, so that there is no real significant distinction between the separation distance and an infinite distance. The amount of gravitational potential energy is roughly comparable the potential energy of the cluster freely falling from an infinitely dis-

tant point. In-falling clusters will convert this energy into kinetic energy with typical speeds reaching $\sim$2000 km s^{-1} (Sarazin, 2008). These speeds are about a factor of 2 times larger than the virialized motions of the galaxies and ICM (Sarazin, 2008). The virialized motions are comparable to the thermal velocity (sound speed) in the cluster (Sarazin, 2008), which means that the infalling galaxy cluster is supersonic. Supersonic motion of a cluster relative to the other initiates a shock wave in the ICM upon collision that propagates through each cluster, dissipating kinetic energy into the material primarily as thermal energy and turbulence within the ICM gas. This process heats the ICM to higher temperatures, increasing the per-particle kinetic energies and destabilizing the virial equilibrium (Sarazin, 2002, 2008).

2.4.1 Merger Shocks

Each cluster contains a significant amount of gas that is distributed across the potential well of each respective cluster. The mass of the gas is $\sim 10^{14} M_{\odot}$ and exceeds the total mass of all galaxies in a typical rich cluster (Sarazin, 2008). The ICM usually has temperatures between $10^6 - 10^8$ K (which corresponds to thermal energy per particle of about $10^2 - 10^5$ eV) and a luminosity between $\sim 10^{43}$ erg s^{-1} and $\sim 10^{45}$ erg s^{-1} (Sarazin, 2002, 2008; Binney & Tremaine, 2008).

When two clusters collide, the ionized gas of the ICM interacts over short time scales, usually settling within a sound crossing time period. Galaxies take longer, usually multiple crossing time periods in order to reach the same status. During this additional time, the passage of outer (usually spiral) galaxies through one or both ICMs may strip gas and dust from the galaxies onto the ICM. Because of the immediate interaction, though, the gas returns to hydrostatic equilibrium very quickly following the inital collision. The energy of the interaction is transformed mostly into thermal energy in the ICM, leading to a higher ICM temperature and an increased radiation in the X-ray.

The effects of the merger can be seen primarily in two ways during the collision. The first is found in thermal effects from the ICM which are visible in the x-ray spectrum. The

collision of ICM may involve a shock due to the supersonic relative motions of the ICMs. The shock is where temperature, pressure and density increases sharply as material from one ICM moves through the other ICM. The increase of density and temperature are both known to increase x-ray luminosity exponentially. The shock wave would appear as a line or curve of high temperature x-ray emission, most likely perpendicular to the cluster's radius (Sarazin, 2008).

The second category of effects of a merger is non-thermal. This can include the turbulence created by varying motions and magnetic fields within the ICM, as well as the effect of a shock propagating through the ICMs. In both cases, the near-relativistic motions of ions (that are already present in one or both ICM) are reaccelerated to relativisitic speeds. For electrons, the helical motion around the magnetic fields in the region may cause synchrotron radio emission. The acceleration causes the electrons to slow, losing kinetic energy which is radiated as photons in the form of radio emission (Sarazin, 1988, 2002, 2008; Binney & Tremaine, 2008).

This synchrotron radiation is usually seen as broad, diffuse radio emission that either trails a shock wave, called a radio relic, or emanates from the core of the cluster as associated with the turbulence of the ICM, called a radio halo. Other synchrotron emission can occur, such as a head-tail radio feature, where a radio source (such as an active galactic nucleus) produces radio emission that is swept away by the flow of the ICM.

2.4.2 Cluster Environments

The population of member galaxies within a cluster are expected to have consistent environments due to a shared evolutional history (Beers & Geller, 1983; Loken et al., 1999). Merger events can cause the environment of the cluster to change substantially (Beers & Geller, 1983), impacting cluster member galaxies through morphology (Moore et al., 1996) and star formation rates (Balogh et al., 2000). By studying the member galaxies, the dynamical history of the cluster can be analyzed.

Brightest cluster galaxies are galaxies that are brighter than any other galaxy in the cluster (Binney & Tremaine, 2008). In many clusters, these are giant elliptical galaxies that are classified as cD-type galaxies (Dressler, 1984; Kormendy & Djorgovski, 1989). Brightest cluster galaxy and cD galaxy are often used interchangeably (Binney & Tremaine, 2008), and the cD label simply indicates that the galaxy has an extended halo that extends out to about 1 Mpc (Binney & Tremaine, 2008; Binney & Merrifield, 1998). cD-type galaxies tend to exist at the density maximum of the cluster (Kormendy & Djorgovski, 1989; Beers & Geller, 1983; Binney & Tremaine, 2008).

The merging process is believed to be a possible origin of brightest cluster galaxies (Dubinski, 1998), especially in clusters that appear to have two or more bright, giant ellipticals at the density maximum (occasionally referred to as secondary nuclei, see Kormendy & Djorgovski (1989) for review). Other mechanisms may also explain their existence and their unique qualities (Kormendy & Djorgovski, 1989; Merritt, 1984a,b; Sarazin, 1986). These large, massive elliptical galaxies appear to dominate their respective galaxy clusters, usually residing at the center of the potential well. The structure and location of the brightest cluster galaxies suggests that they have a unique formation history that is associated with cluster formation (Kormendy & Djorgovski, 1989; Merritt, 1984a). These galactic environments may provide the most direct evidence of the long-term dynamical history of a cluster.

Elliptical and Spiral galaxies also populate most rich clusters with elliptical galaxies being found in higher fraction in the core of the cluster (Dressler, 1980b). Spiral galaxies are more likely to be found near the edges of galaxy clusters (Adami et al., 1998). This suggests that the morphology of the galaxy's structure corresponds to its specific cluster environment (Moran, 2008; Dressler, 1980b).

2.5 Prior Studies of Abell 154

Abell 154 has a unique structure that is difficult to identify. It does not appear to be relaxed, nor are there clear indications of ongoing interactions between groups of cluster members. However, in the hierarchical merging scenario, discussed previously (see Section 2.1), the cluster (and possibly subclusters) may be found at any point between an initial interaction and two-body relaxation. Initially, dramatic effects that occur during merger events are generally completed within 1-2 crossing times. In considering timescales, it is possible to find a cluster that has not yet developed a cooling flow but also does not show dramatic indications of current merging activity ($t_{\rm cool} \gg t_{\rm cross}$).

Figure 2.6 shows the cluster with $60' \times 60'$ dimensions. Figure 2.7 presents a view of the core of the cluster – spanning $10' \times 10'$ – which will be discussed in further detail in Section 2.5.2. Both figures are courtesy of the Digitized Sky Survey.[1]

Abell (1958) completed the first significant study of the cluster and provided it in his original catalog in 1958. Abell classified the cluster as a Richness Class 1. Richness class is based on the number of galaxies that exist, within an Abell Radius along the line of sight between the magnitude of the third brightest galaxy (m_3) and two magnitudes dimmer. An Abell Radius is the cluster radius used to arbitrarily define the edge of the cluster. It is defined as 1.72/z arcminutes, where z is the redshift of the cluster (Abell et al., 1989). Richness Class 1 represents a group where 50-79 galaxies within the 2 magnitude window could be identified and contains 51% of all clusters in the catalog. This class is richer than 30% of the clusters in the catalog, and only 19% of the clusters in the catalog are in a richer class.

Additionally, Abell classified the cluster as a Distance Class 3. Distance Class is based on the magnitude of the 10th brightest galaxy (m_{10}), within an Abell Radius, using the assumption that the brightness of the galaxy is a proxy for distance. A Distance Class

[1]The Second Palomar Observatory Sky Survey (POSS-II) was made by the California Institute of Technology with funds from the National Science Foundation, the National Geographic Society, the Sloan Foundation, the Samuel Oschin Foundation, and the Eastman Kodak Corporation.

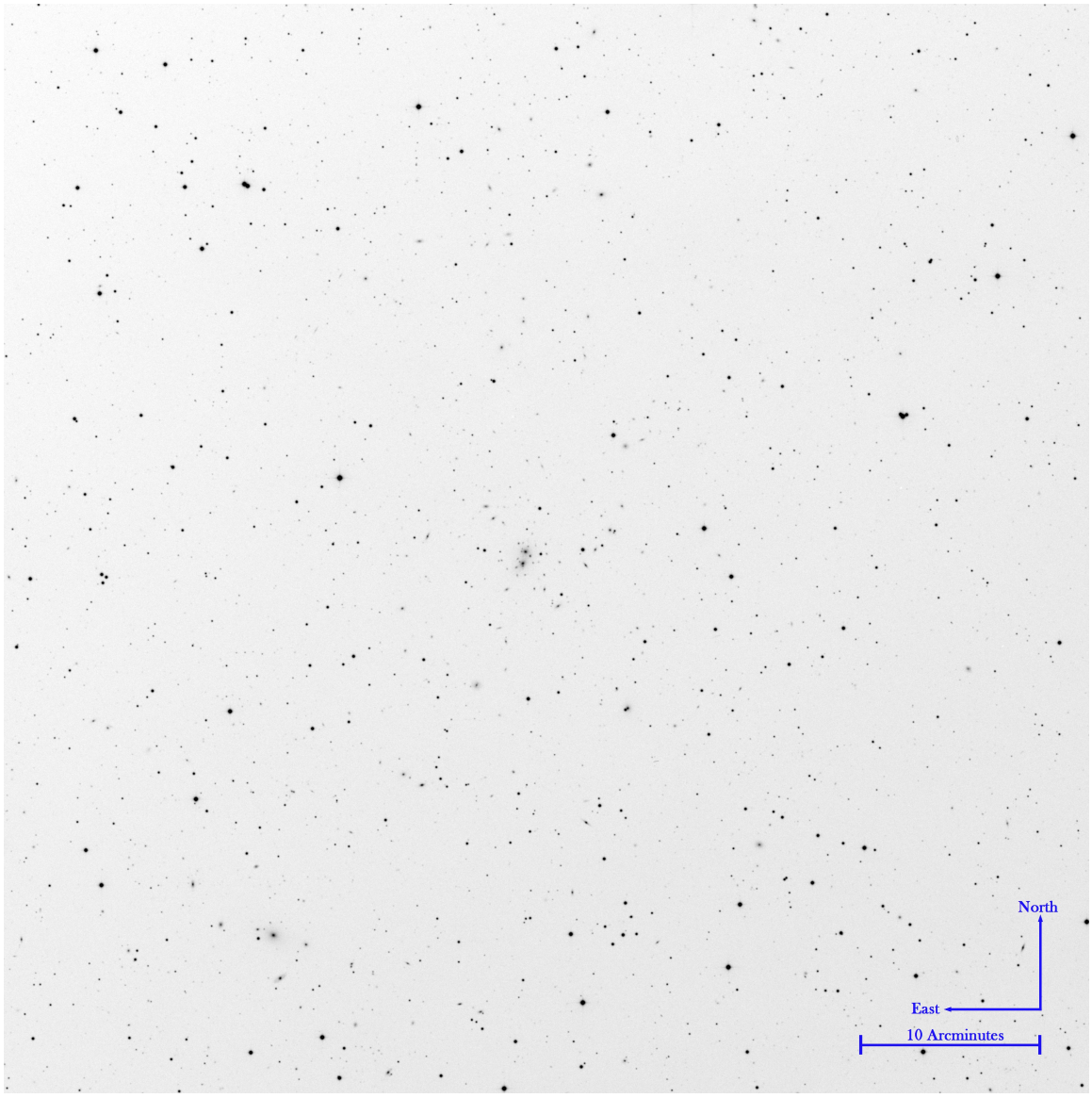

Figure 2.6: Abell 154 from the POSS-II survey (inverted). Field of view of the image is 60 arcminutes by 60 arcminutes. Direction and scale are indicated at the bottom right of the image. Image acknowledgement: The Second Palomar Observatory Sky Survey (POSS-II)

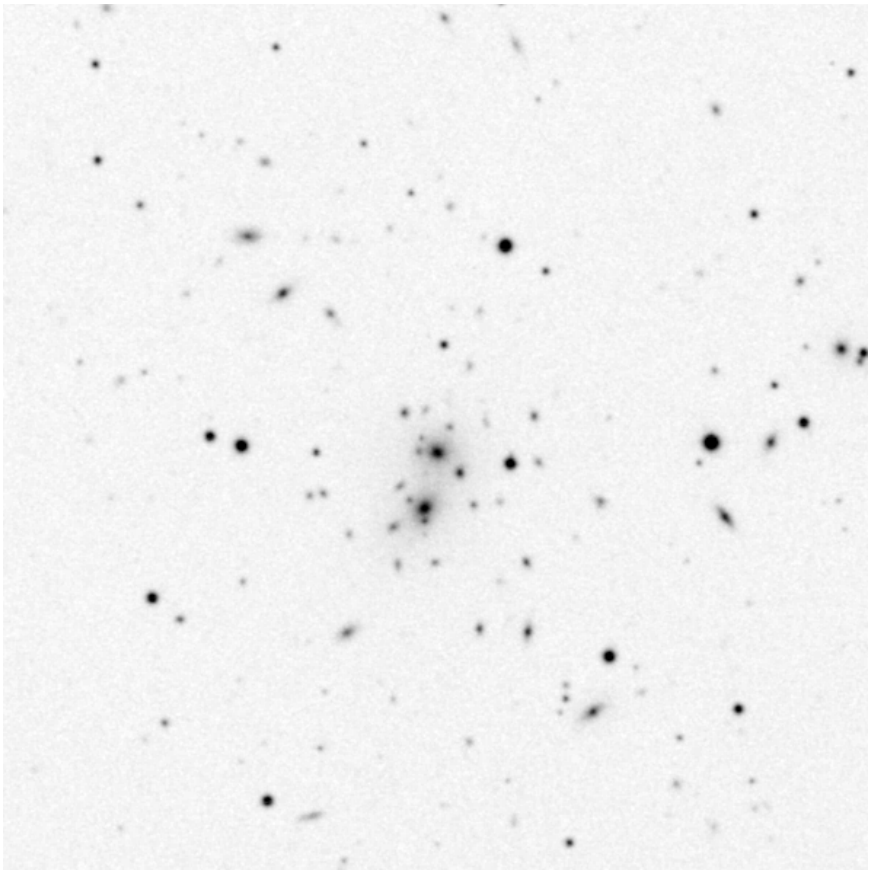

Figure 2.7: Abell 154 core from the POSS-II survey (inverted). The faint luminous bridge between the two large bright elliptical galaxies can be seen. Field of view of the image is 10 arcminutes by 10 arcminutes. Direction is the same as Figure 2.6. Image acknowledgement: The Second Palomar Observatory Sky Survey (POSS-II).

3 represents a cluster with m_{10} between 14.9 and 15.6 in apparent magnitude and contains only 3% of all clusters in the catalog. Less than 1% of all clusters were classified into brighter (closer) distance class, but 96% were classified into a dimmer (further) distance class.

Details on Abell 154 are summarized in Table 2.3. Equatorial and Galactic Coordinates for Abell 154 were presented in Abell et al. (1989). Cluster radius was last estimated by Barkhouse et al. (2007). The last significant compilation of radial velocity data on this cluster was from Struble & Rood (1999) paper, but it only included data from 1990 and prior. Photometric redshift and extinction were both determined most recently by Gal et al. (2000). Rood-Sastry type and Bautz-Morgan type were collected from the papers that originally presented those types (Bautz & Morgan, 1970; Rood & Sastry, 1971). This dissertation will also include further radial velocity values from the literature that are more recent than 1990. Further analysis and discussion of radial velocity data is presented in Chapter 3.

2.5.1 Morphology and Appearance

In the past, there has been significant confusion on the status of Abell 154 with mixed reactions from multiple studies. Several studies indicate that the the cluster is in a relaxed state (Dressler, 1976; Baier, 1977), while others suggest that the cluster is exhibiting signs of merger activity (Dressler, 1978a,b; Carter & Metcalfe, 1980). Some studies can only state that the evidence is insufficient (Geller & Beers, 1982). One study, by Zabludoff et al. (1993), indicated that the contamination of interlopers, especially foreground galaxies, may interfere with the analysis of Abell 154 and could be a primary cause of disagreement between studies.

Kriessler & Beers (1997) ran a Kaye's Mixture Model (KMM) algorithm (McLachlan & Basford, 1988) on the positions in right ascension and declination of the galaxies in Abell 154. The KMM algorithm is designed to identify and isolate clusters that overlap or are mixed and to calculate the likelihood of a correct model by fitting groups with Gaussian distributions. Kriessler & Beers (1997) were attempting to identify potential substructure within the 79 galaxies by examining their likelihood of fitting into two or more groups. A

	Value	Reference
Right Ascension (J2000.0)	$1^h8^m18^s$	Abell et al. (1989)
Declination (J2000.0)	$+17°39.9'$	Abell et al. (1989)
Constellation	Pisces	Davenhall & Leggett (1997)
Galactic Latitude (b)	-44.96°	Abell et al. (1989)
Galactic Longitude (l)	129.52°	Abell et al. (1989)
Cluster Radius (R_{200})	2.626 Mpc	Barkhouse et al. (2007)
Heliocentric Radial Velocity (c_z)	19067 km s^{-1}	Struble & Rood (1999)
Radial Velocity Dispersion ($\sigma_{Z,cl}$)	868 km s^{-1}	Struble & Rood (1999)
Heliocentric Cluster Redshift (Z_h)	0.0636	Struble & Rood (1999)
Cluster Redshift relative to CMB (Z_c)	0.0624	Struble & Rood (1999)
Photometric Redshift (Z_{phot})	0.0722 ± 0.0243	Gal et al. (2000)
Abell Richness Class	1	Abell (1958)
Abell Distance Class	3	Abell (1958)
Bautz-Morgan Type	II	Bautz & Morgan (1970)
Rood-Sastry Type	B_b	Rood & Sastry (1971)
Apparent Magnitude (m_{10})	15.6	Abell et al. (1989)
Extinction (E_{B-V})	0.06283	Gal et al. (2000)

Table 2.3: Abell 154 information. This table gives basic details about Abell 154 including a reference in Column 3. Please note that the right ascension and declination values are updated to epoch 2000 (J2000.0) by precessing the original J1950.0 coordinates from Abell et al. (1989). Cluster radius is actually the radius of the circle of area required to contain 200 galaxies while centered on the cluster center - the galaxies have not been confirmed as members of the cluster. Heliocentric Radial Velocity is the recessional velocity of the cluster after removing the earth's orbital revolution. Redshift relative to CMB is the recessional redshift as compared to the relative motion of the 3 Kelvin Cosmic Microwave Background. Apparent magnitude is based on the 10th brightest galaxy near the cluster center. Extinction is due primarily to interstellar dust within the Milky Way in the direction of A154.

standard 2 group model did not seem to fit the 79 galaxies, but a 3 group model does fit with each group having 37 galaxies, 21 galaxies and 21 galaxies, respectively (Kriessler & Beers, 1997). These results suggest potential substructure, however, Kriessler & Beers (1997) does not take into account radial velocity information or the potential presence of interlopers within the field.

2.5.2 Cluster Core

A unique quality of Abell 154 is the appearance of two giant elliptical galaxies at the core of the cluster. Initially, these galaxies are described as being D-type (Dressler, 1980a; Beers & Geller, 1983) due to the diffuse halo that surrounds them, but this classification appears

to be an ambiguous and antiquated distinction (Kormendy & Djorgovski, 1989; Beers & Geller, 1983). These galaxies exist in a common, extended envelope (Bautz & Morgan, 1970; Beers & Geller, 1983) of luminous material that connects as a bridge between the galactic halos (Rood & Sastry, 1971). The two galaxy system is believed to dominate the central cluster environment in a manner similar to the way a cD-type elliptical galaxy dominates the cluster environment (Quintana & Lawrie, 1982; Beers & Geller, 1983). Several papers make comparisons between Abell 154's binary core to the cD galaxies at the center of the Coma cluster (Dressler, 1978a,b; Carter & Metcalfe, 1980), while other papers treat them as any other cD galaxies (Beers & Geller, 1983; Makino & Tomita, 1995; Feretti & Giovannini, 1994; Sarazin, 1986; Kormendy & Djorgovski, 1989).

The formation and evolution of brightest cluster galaxies and cD-type galaxies is an area of active research. Some research suggests that the diffuse halo and bridge is due to galactic canabalism or tidal stripping of other core galaxies (Dressler, 1980b; Ostriker & Tremaine, 1975; Postman & Lauer, 1995; Loubser et al., 2008), which may suggest that the core galaxies are steadily coalescing into a single cD galaxy through a processes of dynamical friction (Dressler, 1978a,b). Galactic cannibalism, which could also be called a minor merger, is the process where a galaxy accretes or consumes its smaller neighbors (Binney & Tremaine, 2008), and tidal stripping is where material in a nearby galaxy is stripped, initially from the outer parts of the nearby galaxy, due to the gravitational encounter with another galaxy (Binney & Tremaine, 2008). More recent studies conclude that the dynamical friction would be insufficient for creating the large envelope and drawing the elliptical galaxies together (Merritt, 1984a; Dubinski, 1998). Reliable information on the radial velocities of these galaxies would be invaluable in supporting or refining these hypotheses.

A recent study on Brightest Cluster Galaxies by Lauer et al. (2014) results in some facts that suggest that Abell 154 may have an abnormal core structure in velocity space. Of the 433 clusters that were studied, Abell 154's velocity dispersion is larger than 90% of the clusters. Also, when observing clusters that have two bright galaxies at their core, the

velocity dispersion of Abell 154 is larger than 89% of the other clusters (Lauer et al., 2014). Additionally, the velocity difference between the two brightest galaxies is larger for Abell 154 than 98% of the other clusters that have two bright galaxies in the study (Lauer et al., 2014). The uniquely large velocity differences and dispersions does not support the merging of the two large elliptical galaxies (Ostriker, 1980), but rather, it may be an artifact of a two clusters falling towards their mutual center of gravity.

The cluster core is found to have an elongated distribution within the innermost 0.5 Mpc of the cluster, which was first believed to be a deviation from what is expected in a virialized cluster (Carter & Metcalfe, 1980). However, further research indicates that clusters generally appear elongated instead of spherical within the innermost portions of clusters (Geller & Beers, 1982), and many clusters appear to deviate from a relaxed appearance within as far out as 0.24 Mpc from the center (Geller & Beers, 1982). When looking beyond 0.5 Mpc, all of these studies agree that the distribution of galaxies is relatively spherical (Geller & Beers, 1982; Dressler, 1976; Carter & Metcalfe, 1980).

Later studies indicate that there is an intrinsic twist in the cluster's isophote contours that may be caused by an external perturbation (McMillan et al., 1989; Porter et al., 1991). The isophotal twist is evident enough in another study where Abell 154 was used as a prototypical example by which to compare other clusters (McMillan et al., 1989; Porter et al., 1991). This twist in isophotal contours of about 25° was statistically analyzed and was found to correspond to potential core substructure (West & Bothun, 1990; Ledlow & Owen, 1995), but further analysis has not yet been completed. Corroboration of this potential substructure through radial velocity data is pertinent and may clarify or reject these analyses.

In addition to the optical and X-ray studies, which are generally in agreement in description of the core (Paolillo et al., 2001; Blakeslee & Tonry, 1992), the radio detections of the core present as two moderate sources that are located about 3 kpc apart and is likely associated with the southern large elliptical galaxy (Feretti & Giovannini, 1994). A third, weaker radio source was detected much further south and appears to be associated with

an elliptical galaxy at that location (Slee et al., 1994). Broad or extended, diffuse radio emission, such as a radio halo or a relic, was not detected (Owen & Ledlow, 1997; Slee et al., 1994; Feretti & Giovannini, 1994).

2.5.3 Previous Radial Velocities

Prior studies have collected radial velocities for only 62 galaxies (see Table 3.4 for a summary) within the Abell 154 cluster, but only as many as 42 radial velocities were studied at any given time. This small number of galaxies is still highly impacted by the sampling error due to a small sample size. The earliest analysis of radial velocity structure was from Faber & Dressler (1977). It was not until later studies that observations could discern a foreground group that is separated significantly from the main group in velocity space (Struble & Rood, 1991; Zabludoff et al., 1993). There was also a challenge in determining the radial velocity of the main group due to the appearance of multiple peaks in the velocity histogram (Faber & Dressler, 1977; Dressler, 1978a,b; Carter & Metcalfe, 1980; Geller & Beers, 1982). However, the more recent measures indicate an average radial velocity of the main group of 19067 km s^{-1} (Struble & Rood, 1999). Due to the limited radial velocity data, literature sources have mainly focused on comparing Abell 154 to various other clusters based on cluster morphological features, such as the core structure (Smith et al., 1985; Hoffman & Williams, 1991).

2.5.4 X-ray Sources and Cooling Flow Signatures

Abell 154 exhibits multiple X-ray sources that appear to coincide with cluster galaxies. As a cluster, the overall X-ray intensity is low for a galaxy cluster (Ricketts, 1978; White et al., 1997; Elvis et al., 1992; McMillan et al., 1989), but the upper limit to the peak of A154 is unusually high when compared to other clusters (Ricketts, 1978) of similar distance and richness classes. Low luminosity background with a strong peak is a description commonly associated with cooling flows, see Section 2.3.2.

X-ray information for Abell 154 was only available from the Einstein Observatory archives and was previously presented by McDowell (1994) and McMillan et al. (1989). See Figures 2.8 and 2.9 for images from the Einstein X-ray Observatory (McDowell, 1994; McMillan et al., 1989).

X-ray analyses from the literature provides some evidence associated with cooling flows. Cooling flows are thought to be common in galaxy clusters (Stewart et al., 1984; White et al., 1997; Edwards et al., 2007), and the unusually strong X-ray peak near the core of the cluster (Ricketts, 1978) is a typical characteristic. Brightest cluster galaxies, like the two large elliptical galaxies at the center of Abell 154, are commonly found at the center of cooling flow clusters (Edwards et al., 2007). Studies predominantly indicate, however, that a cooling flow does not exist for Abell 154 (Jones & Forman, 1984; Stewart et al., 1984; David et al., 1992; White et al., 1997; Loken et al., 1999). Many of these studies draw their conclusions for Abell 154 after estimating the cooling time and comparing it to a Hubble time. In each calculation, the cooling time for the core of Abell 154 is much longer than a Hubble time (Stewart et al., 1984; White et al., 1997; David et al., 1992).

A method of deprojection was used to analyze the X-ray data by several studies (Jones & Forman, 1984; David et al., 1992; Stewart et al., 1984; White et al., 1997). The deprojection method is essentially reducing the two-dimensional projection in the plane of the sky into three-dimensional data. Based on that three-dimensional result, Abell 154 appears to have a cooling time of a factor of $2.50^{+3.67}_{-1.35}$ times greater than a Hubble time (White et al., 1997). Even at the minimum cooling time, the time exceeds a Hubble time, therefore Abell 154 should not be exhibiting a cooling flow.

X-ray data do suggest multiple peaks (McMillan et al., 1989; Paolillo et al., 2001; Barkhouse et al., 2007) and does not show significant difference from what is seen in optical data (Ulmer et al., 1992; Blakeslee & Tonry, 1992; Hoffman & Williams, 1991). A discernible difference, or twist, in the orientation between the outer and inner isophotes is clearly seen in X-ray (McMillan et al., 1989), and it is located at the same locations that similar features are

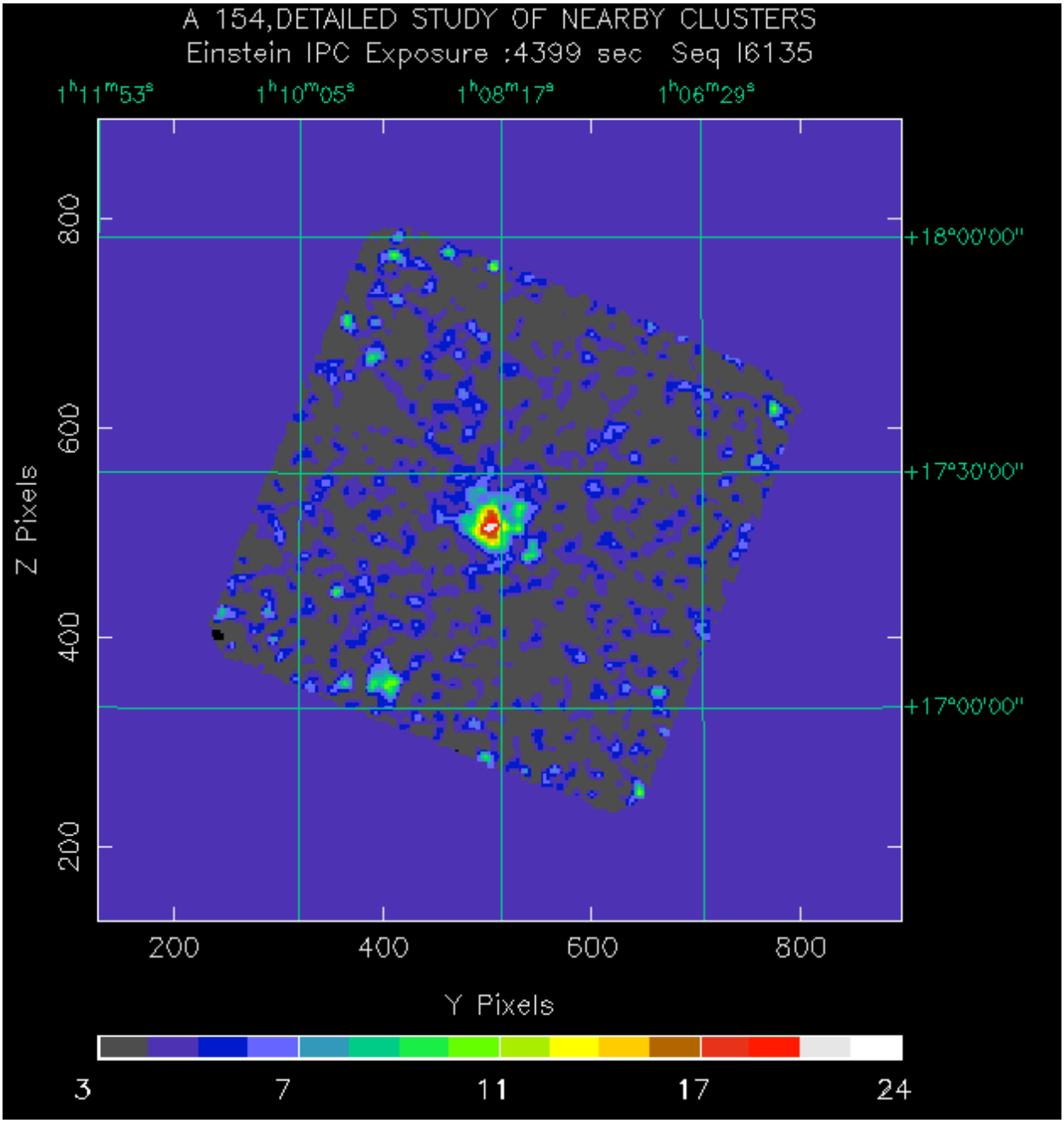

Figure 2.8: Einstein X-ray image of Abell 154. Resolution of the x-ray image is poor due to outdated technology, but a clear peak can still be seen. Note that the colors represent the number of counts per second for the detector area and angular resolution, and correspond to thermal energies between 0.2 keV and 3.5 keV. The peak is directly over the southern large elliptical galaxy. Asymmetry can be seen to the northwest of the center of the emission. There is also a secondary peak in the x-ray to the south east of the main peak. The image was retrieved from Einstein databases and presented by McDowell (1994).

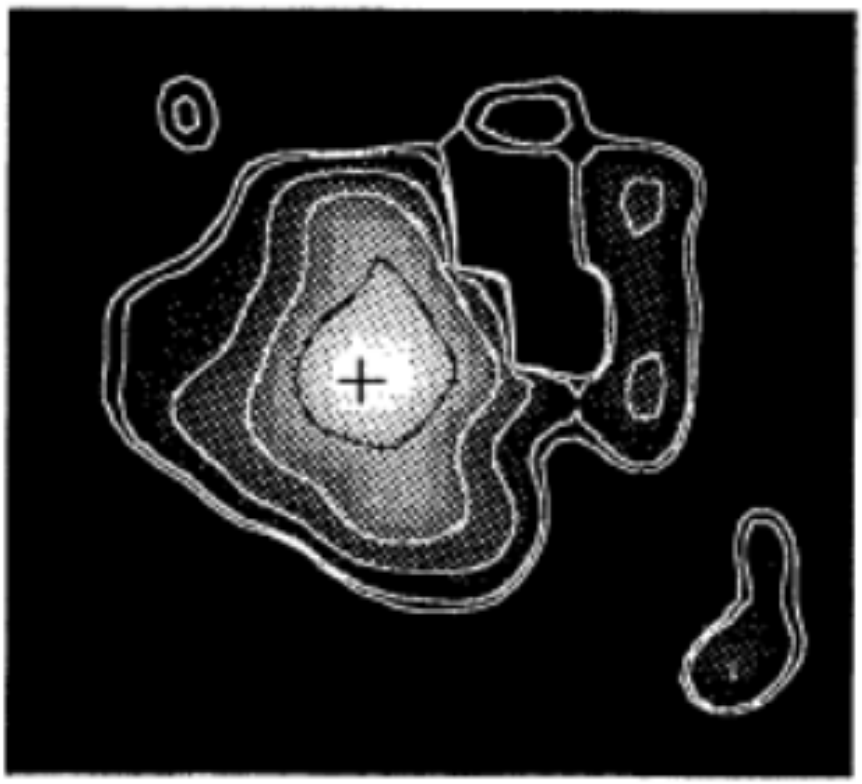

Figure 2.9: X-ray contour image of the core of Abell 154. The intensity peaks at 4.209×10^{-3} counts cm^{-2} arcminutes^{-2} s^{-1}, and contours in this image represent flux levels of (0.192, 0.288, 0.432, 0.648, 0.972)$\times 10^{-3}$ counts cm^{-2} arcminutes^{-2} s^{-1}. The northwest spur is clearly seen in this image. The image was retrieved from McMillan et al. (1989).

seen in the optical (see Section 2.5.2). This change in orientation appears to be continuous throughout the core and does not have a clear, distinctly different outer orientation like the majority of clusters that have the same characteristic (McMillan et al., 1989). The correlation between both optical and X-ray data suggests that this feature is not an artificial result and may be an important factor to consider in analysis.

2.5.5 Photometric Analysis

With the advent of the Charge-Coupled Device (CCD), photometry of galaxy clusters has become easier. CCD detectors are significantly more sensitive than the photographic plates and photomultiplier detectors that were used in the earliest analyses of galaxy clusters. In planning photometric observations, astronomers consider many factors that effect light. One factor to consider is that galaxy cluster members, especially those that reside near the cores of their clusters, are usually elliptical galaxies with old stellar populations and very few spiral galaxies (Dressler, 1980b). However, even cluster members that are spiral galaxies have a notably diminished spiral arm structure (Sarazin, 1988), meaning that there are fewer blue star-forming regions. Galaxy cluster members are, therefore, predominantly more red than their field spiral galaxy counterparts (Bothun, 1998; Sarazin, 1988; Carroll & Ostlie, 2006; Binney & Tremaine, 2008). Because of this, photometry and spectra of galaxies is usually obtained in the red and infrared regions of the spectrum for a galaxy cluster as a way of increasing the likelihood of detecting and imaging cluster members over field interlopers.

Chapter 3

Radial Velocity Measurements

This dissertation presents 176 new radial velocity measurements of galaxies in Abell 154. Additionally, 82 radial velocity measurements from the literature were collected for a total of 258 measurements across 205 galaxies. This chapter summarizes the observations, collection of literature results and reduction of data into a single catalog, which will be analyzed in Chapter 4.

3.1 New Data

Prior studies have attempted to statistically analyze Abell 154 (Merrifield & Kent, 1991; Zabludoff et al., 1990, 1993), but none analyzed the cluster in velocity space with more than 42 galaxies. The latest analysis was successful at identifying a group of galaxies in the foreground (Zabludoff et al., 1993), though it (and other studies) indicated that further data collection is necessary (Hoffman & Williams, 1991; Zabludoff et al., 1993; Faber & Dressler, 1977) for confident analysis of the cluster. Nothing more definitive was found within the literature (which is discussed in more detail in Section 3.2).

3.1.1 Targets for Observation

The goal for new data is to increase the number of galaxies with radial velocities in Abell 154. However, discriminating between stars and galaxies is non-trivial. Galaxies are typically resolved objects (Binney & Merrifield, 1998) with extended luminous bodies (Binney & Merrifield, 1998; Carroll & Ostlie, 2006). However, small galaxies in a cluster may not be resolved and may appear like distant stars within the Milky Way Galaxy. One way to distinguish distant galaxies from stars is to fit each object with a point spread function (PSF) template for a star or a galaxy and evaluate the fit. The Faint Object Classification and Analysis System (FOCAS) (Jarvis & Tyson, 1981) is a program designed to detect and determine the relative likelihood of the object being a star or a galaxy by fitting PSF templates to the object and analyzing the object's shape. It should be noted that some stars may appear more like galaxies due to seeing. These will need to be eliminated in a later process.

Observing targets were identified by using POSS-I E image[1] of Abell 154 and processing it with FOCAS. The POSS-I E image was taken using a red filter that has a peak transmission at 6500Å. This is to exploit the property that member galaxies of a cluster are predominantly more red in color, see Section 2.5.5 (Dressler, 1980b; De Propris et al., 2004; Balogh et al., 2000; Allen et al., 2011), which helps to reduce the chances of targeting stars and interloper field galaxies that tend to be brighter at shorter wavelengths.

3.1.2 Observations

Spectra of 176 galaxies were obtained by Robert C. Berrington, in October of 1997, using the WIYN 3.5 m telescope at Kitt Peak National Observatory equipped with the HYDRA multi-object fiber-based spectrograph. The HYDRA spectrograph can capture the spectra of up to 97 targets simultaneously for each field, allowing for the spectra of many objects to

[1]The National Geographic Society - Palomar Observatory Sky Atlas (POSS-I) was made by the California Institute of Technology with grants from the National Geographic Society.

Field	N_{cz}	Stars	Galaxies
Field 1	75	65	10
Field 2	79	44	35
Field 3	84	26	58
Field 4	75	18	57
Field 5	63	19	44
Field 6	23	9	14
Total	399	181	218
Reduced Total	349	173	176

Table 3.1: Targets for observation. The first column represents the number of objects with a radial velocity. The second and third columns are counts of objects that were classified as stars and galaxies, respectively, according to their radial velocities. To distinguish between the classifications, it was arbitrarily defined that anything greater than 10000 km s^{-1} was a galaxy. This was done since there was a large gap between 83 km s^{-1} and 10037 km s^{-1}. The first total is a sum of each field without combining or eliminating duplicated measurements. The Reduced Total accounts for unduplicated results.

be recorded in each frame. A few fibers were dedicated for sky subtraction, but most fields had more than 55 fibers on science objects, see Table 3.1. There were a total of 6 fields observed for Abell 154 with a total of 399 measurements of radial velocities. Each of the six fields, represented by a different color circle, has been superimposed on an image of Abell 154 in Figure 3.1. See also Table 3.2 for dates and details of observations.

3.1.3 Reduction

Each field was observed twice during the same night. This is done to 1.) increase the total integration time of light traveling through the system, which ultimately improves the signal-to-noise ratio for each field, and 2.) reduce the significance of spurious contamination, such as a cosmic ray. However, before this, systematic effects and offsets are eliminated, which can be done through CCDPROC and DOHYDRA routines in the Image Reduction and Analysis Facility (IRAF)[2].

[2]IRAF is distributed by the National Optical Astronomy Observatories, which are operated by the Association of Universities for Research in Astronomy, Inc., under cooperative agreement with the National Science Foundation.

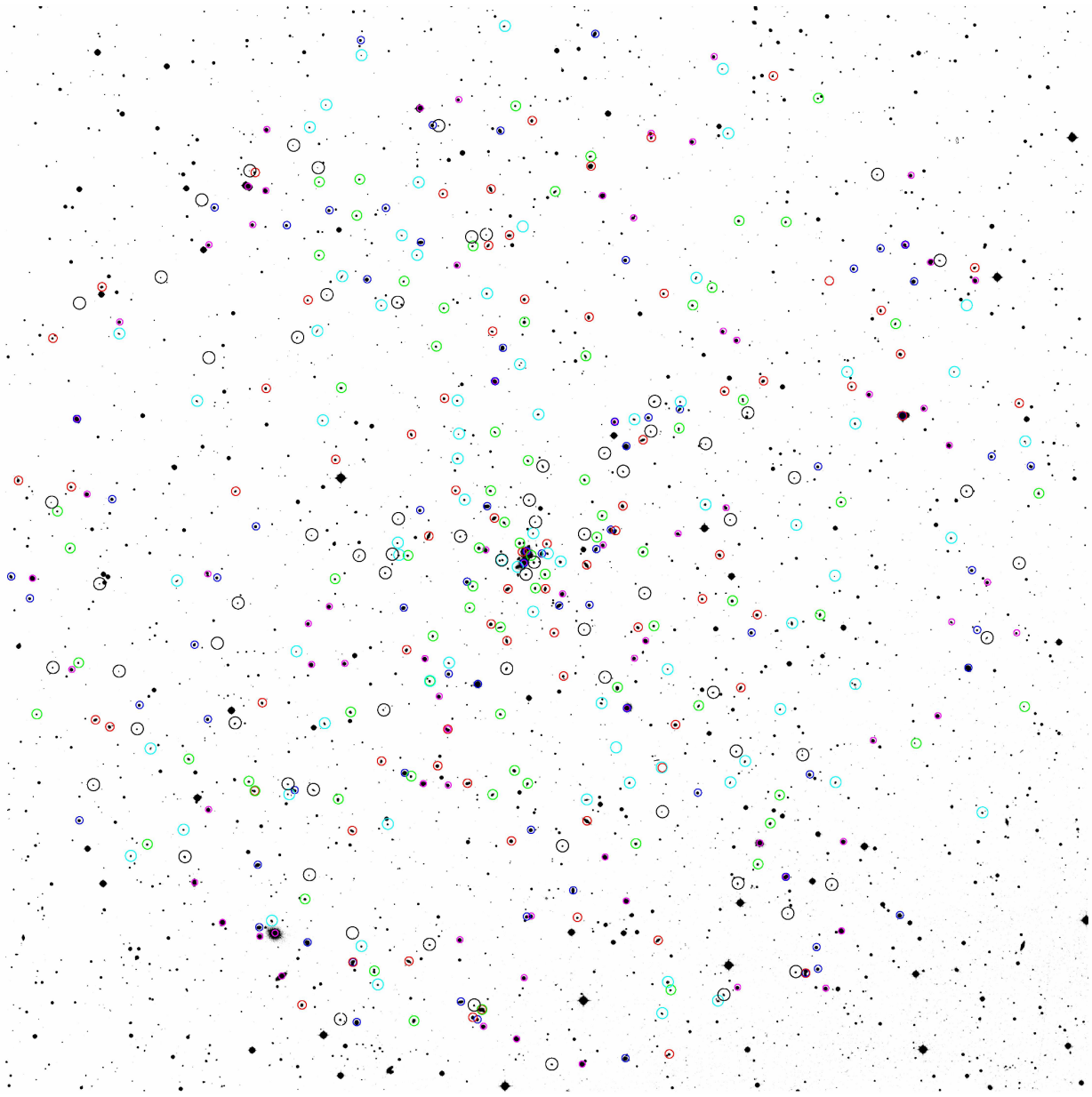

Figure 3.1: Targets for radial velocity measurements. Each circle color represents a different observational field: Magenta is for Field 1, Blue is for Field 2, Red is for Field 3, Green is for Field 4, Cyan is for Field 5, and Black is for Field 6. These six fields correspond to the six fields during the observations. The location of the measures were superimposed on the DSS image of Abell 154. Note that some targets may actually be a blank area of sky or a star rather than a galaxy.

Object	UT Date	UT Time	Exposure Time
NGC 7331	10/8/97	03:19:42	600 s
NGC 7331	10/8/97	03:36:28	900 s
M 31	10/8/97	04:03:23	600 s
Abell 154, Field 1	10/8/97	05:06:35	3600 s
Abell 154, Field 1	10/8/97	08:48:37	3600 s
Abell 154, Field 2	10/8/97	10:43:17	3600 s
Abell 154, Field 2	10/8/97	11:45:18	3600 s
Abell 154, Field 3	10/9/97	07:21:53	3600 s
Abell 154, Field 3	10/9/97	08:23:53	3600 s
Abell 154, Field 4	10/9/97	10:05:38	3600 s
Abell 154, Field 4	10/9/97	11:07:37	3600 s
Abell 154, Field 5	10/10/97	08:32:05	3600 s
Abell 154, Field 5	10/10/97	09:34:05	3600 s
Abell 154, Field 6	10/10/97	11:44:33	3600 s
Abell 154, Field 6	10/11/97	00:08:34	2640 s

Table 3.2: Observations at Kitt-Peak National Observatory. Observations were made by Dr. Robert Berrington. Calibration images (bias, flats, and comparisons) were taken throughout the observing run. Observations were made with the 600 lines mm^{-1} grating with a blaze angle of 13.9° and a central wavelength of 5701Å. UT stands for Universal Time. The UT Time column represents the midpoint during the exposure.

CCDPROC and DOHYDRA

Reduction was processed using standard methods (Birney et al., 2006) and was mainly automated through IRAF. First, each image was corrected for systematic, additive offsets by subtracting the overscan and bias using the CCDPROC routine.

The DOHYDRA routine is then used to eliminate uneven illumination and background sky effects. Dome flats, illuminated by a continuous light source, were used to locate the position of each fiber and to normalize the intensity to remove the blackbody curve. DOHYDRA also calibrates the alignment of the grating to wavelengths across the spectrum image by using a thorium-argon comparison lamp whose emission features can be identified by wavelength. Comparison exposures of the lamp were taken both before and after the target images. Once features are tagged with the correct wavelength, DOHYDRA calculates a pixel-to-wavelength mapping that can be applied to other images and comparisons that will be used during the process.

Once each image has been calibrated through CCDPROC and DOHYDRA, the pair

of images for each field are combined using the SCOMBINE routine in IRAF. For Fields 1-3 and 5, images were averaged together. Fields 4 and 6 both completed their second exposure during astronomical twilight, which increased the sky background noise for those exposures. To limit the effect of an increased sky background, these frames were combined by summing, rather than averaging. The final result is 6 fully-reduced frames, containing up to 97 objects each, which can be analyzed next in the FXCOR routine.

FXCOR

Each image is then processed by the IRAF Fourier Cross-Correlation Routine (FXCOR), where the correlation between two spectra are used to calculate a radial velocity. This routine utilizes a fourier transform that is used to compare the variations between an object spectrum and a reference spectrum to develop the most frequent correlation. A filter is used to remove frequencies that are too extreme, especially high frequency correlation that is dominated by the random fluctuation of noise.

FXCOR fits each spectrum to three reference spectra for the evaluation of spectral shift. The three reference spectra used for this research includes two images of NGC 7331 and one image of M31. In order to analyze radial velocities, the radial velocity of the reference object must be entered in to the VHELIO field in the header of each reference image file. The radial velocity values for the reference objects were obtained from the NASA/IPAC Extragalactic Database (NED)[3]. For NGC 7331, the heliocentric velocity is 816 $\pm$ 1 km s^{-1} (Huchra et al., 1999), and for M31, the heliocentric velocity is -297 $\pm$ 1 km s^{-1} (Haynes et al., 1998). Each spectrum within each image is compared to all three reference spectra using FXCOR (Tonry & Davis, 1979).

Since none of the reference spectra contained emission features, initially, only spectra based on the absorption features are processed. Absorption and emission features were previously shown in Figures 2.1 and 2.2. Absorption and emission features are either dips

[3]The NASA/IPAC Extragalactic Database (NED) is operated by the Jet Propulsion Laboratory, California Institute of Technology, under contract with the National Aeronautics and Space Administration

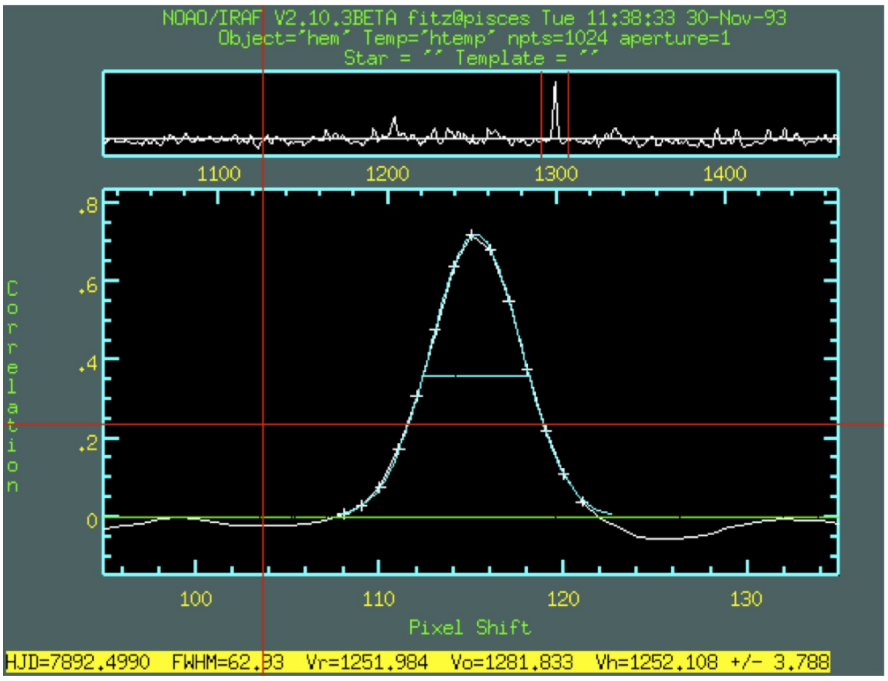

Figure 3.2: FXCOR interactive display. The interactive FXCOR routine that correlates each spectra with each reference spectrum to identify radial velocity measurements and to reduce high frequency uncertainties.

or peaks in the spectrum, respectively, of which several were labeled in those figures. Some galaxies with strong emission features either do not have strong absorption features or are impacted too much by the random noise in the spectrum for accurate analysis. An alternative for emission-line galaxies is discussed in Section 3.1.3.

The FXCOR routine is interactive, allowing the user to choose the most probable correlation peak, which is usually the highest peak (see the top box in Figure 3.2 or the middle boxes in either Figure 3.3 or 3.4). Since it is possible for a correlation to be an artifact of spurious contamination or random noise, each calculated radial velocity is also verified visually. The output data from the FXCOR routine includes both an image for each spectrum, which are shown in Figures 3.3 and 3.4, as well as a catalog with each spectrum's comparison, including the radial velocity as determined through the reference spectra, and the uncertainty according to the correlation fit. Uncertainty on each output is determined based on the relative fit of a Gaussian curve to the cross-correlation function as described by Tonry & Davis (1979) (See the bottom boxes for Figures 3.2, 3.3 and 3.4).

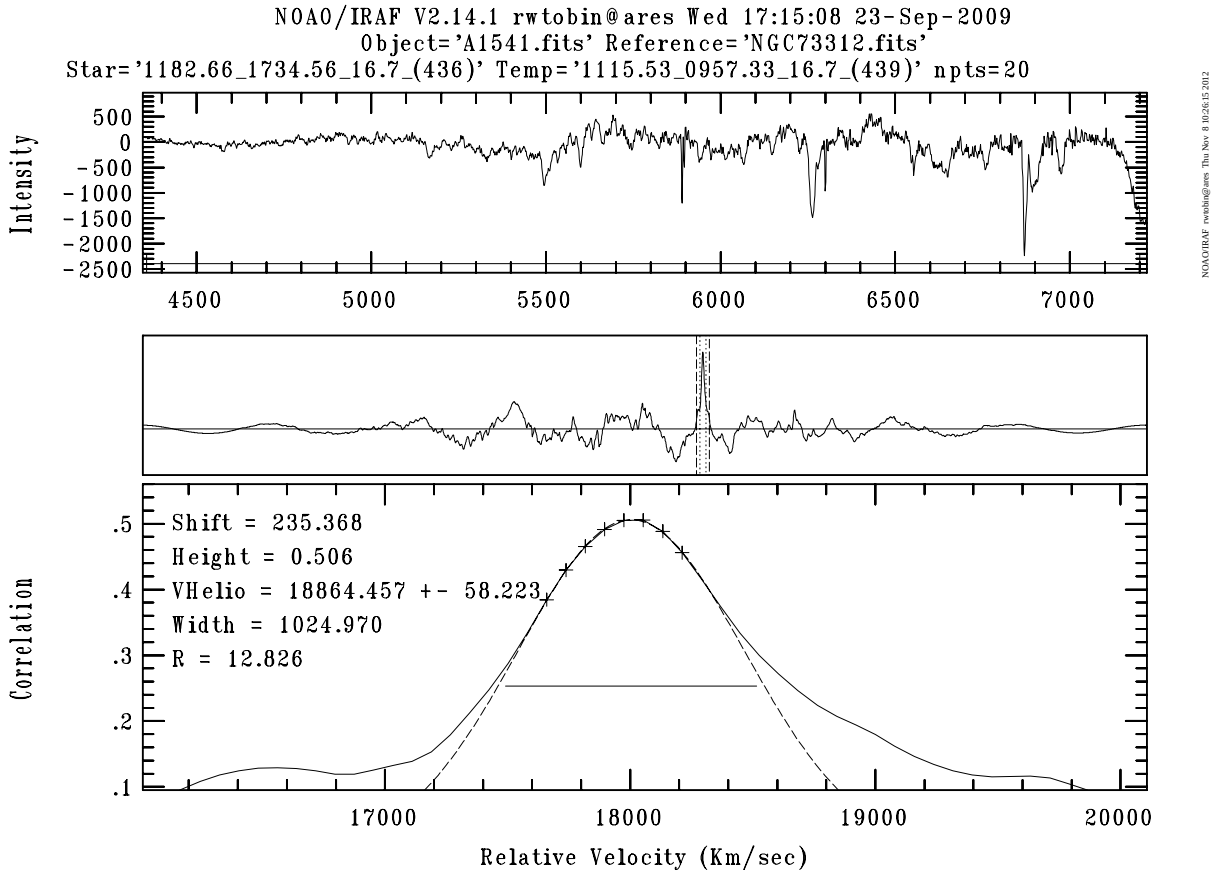

Figure 3.3: FXCOR graphical output of a galaxy in Abell 154. This galaxy's radial velocity was obtained by comparing the spectrum of the object (shown in the top box) to the spectrum of galaxy NGC 7331 (not shown). The middle box shows the significance and frequency of correlation between the spectra across a wide range of radial velocities. The peak that was focused on is clearly 2 to 3 times higher than any other point along the curve, which indicates that it is the point where the majority of features were in alignment. The sharpness of this peak also indicates a high degree of accuracy in selecting this velocity. The correlation box (at the bottom) shows how the fit can be fine tuned, using a few points to align the correlative fit with the fourier transform. The bottom box uses the relative velocity difference between the object and the reference galaxy.

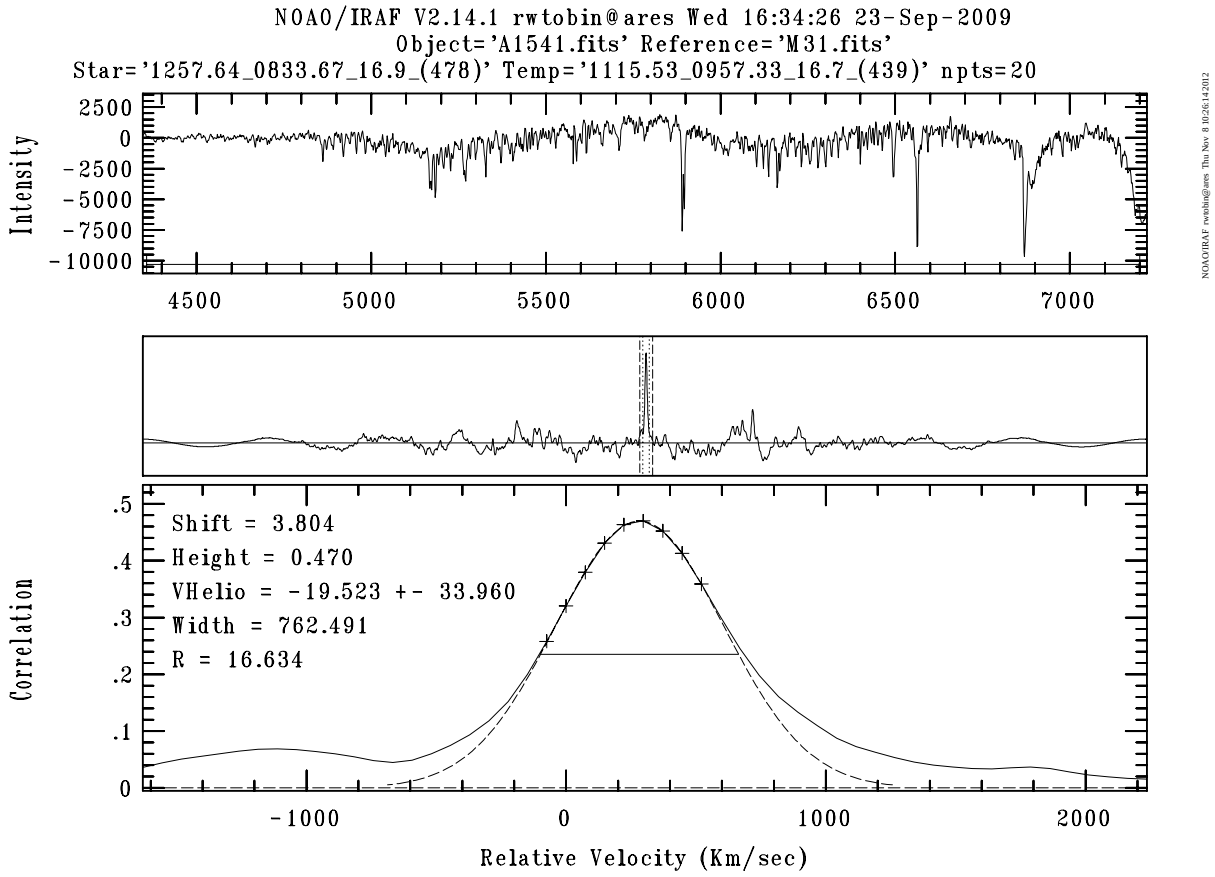

Figure 3.4: FXCOR graphical output of a star. The star's radial velocity was obtained by comparing the spectrum of the object (shown in the top box) to the spectrum of the Andromeda Galaxy (not shown). The middle box shows the significance and frequency of correlation between the spectra across a wide range of radial velocities. The fit clearly shows a relative radial velocity of 300 km s^{-1}, which results in a heliocentric radial velocity of -19.5 km s^{-1}.

Each object has a radial velocity from each correlative fit to each reference spectrum. The three radial velocities for a single object, or triplet, can be used to ensure that the FXCOR routine is self-consistent. If any radial velocity measurement for any object results in inconsistency with respect to the triplet's mean value, the inconsistent spectrum's correlation fit can be reevaluated using FXCOR. Inconsistency is arbitrarily defined as a Z-score value of $Z > 1$ as calculated by

$$Z = \frac{|v_{\mathrm{i}} - \bar{v}|}{\sqrt{\sum \sigma_{\mathrm{i}}^2}}, \tag{3.1}$$

where v_i is a single measured radial velocity, $\bar{v}$ is the weighted average (see Equation 3.2) of the triplet, and σ_i is the uncertainty of each radial velocity measurement. The Z-score is a statistic that describes the consistency of multiple measurements, and it represents the normalized deviation from the most likely (weighted) mean value with respect to the uncertainty of the measures. Each radial velocity represents a sample measurement of the true value, and that multiple samples can be treated as samples in a random distribution that are deviated from the true value. Based on this assumption, it is expected that 68% of measurements have Z-score values of $Z \leq 1$ and 27% of measurements have Z-score values of $1 < Z \leq 2$. Only a small percentage of measurements (about 4.6%) are randomly deviated so far from the average value that they would result in $Z > 2$. If many measurements have Z-score values at this level, this could mean that some other significant source of error exists in one or more measures.

Remarkably, only one radial velocity measurement (out of 1197 total measurements) was inconsistent (Z = 1.16). Reevaluating the measurement, both manually and in FXCOR, resulted in confirming the FXCOR results for this spectrum. Several objects were also observed in more than one field, but the results from the object in each field were also found to be mutually consistent. These high rates of consistency may be due to the assumption being faulty, an overestimation of error from the FXCOR routine, or possibly other reasons that will not be addressed in this dissertation.

Sorting and Combining

Each cataloged output from FXCOR is processed with a sorting/combining routine that sorts, combines and calculates additional information from each fit. Each objective was compared with three reference spectra, resulting in three measurements for each object. The program combines the three measures into one using a weighted average (Leo, 1994; Bevington & Robinson, 2003),

$$\bar{v} = \frac{\sum \frac{v_i}{\sigma_i^2}}{\sum \frac{1}{\sigma_i^2}}, \tag{3.2}$$

where $\bar{v}$ is the weighted average velocity and σ_{i} is the uncertainty of each measurement. Uncertainties were combined by (Bevington & Robinson, 2003),

$$\sigma_\mu = \frac{1}{\sqrt{\sum \frac{1}{\sigma_{\mathrm{i}}^2}}}, \tag{3.3}$$

where σ_μ is the uncertainty of the mean velocity. The same weighted average process is also used to combine duplicated radial velocity measurements from different fields. Data were reduced to a total of 319 unduplicated results for absorption features.

A review of these 319 objects shows a large gap in recessional velocity between 83 km s^{-1} and 10037 km s^{-1}. Recessional velocities above 10000 km s^{-1} are unlikely to be stars since it is an order of magnitude larger than the velocity of the fastest stars (Brown, 2015), and is much larger than the escape velocity of the Milky Way. There were 147 objects with velocities greater than 10000 km s^{-1}, which are assumed to be galaxies. The remaining 173 objects have velocities within a range from -216 km s^{-1} to 83 km s^{-1}, averaging -21 km s^{-1}, which is well below the extremes of observed high velocity stars (Brown, 2015). These objects are most likely stars within the Milky Way. These stars have been circled in Figure 3.5.

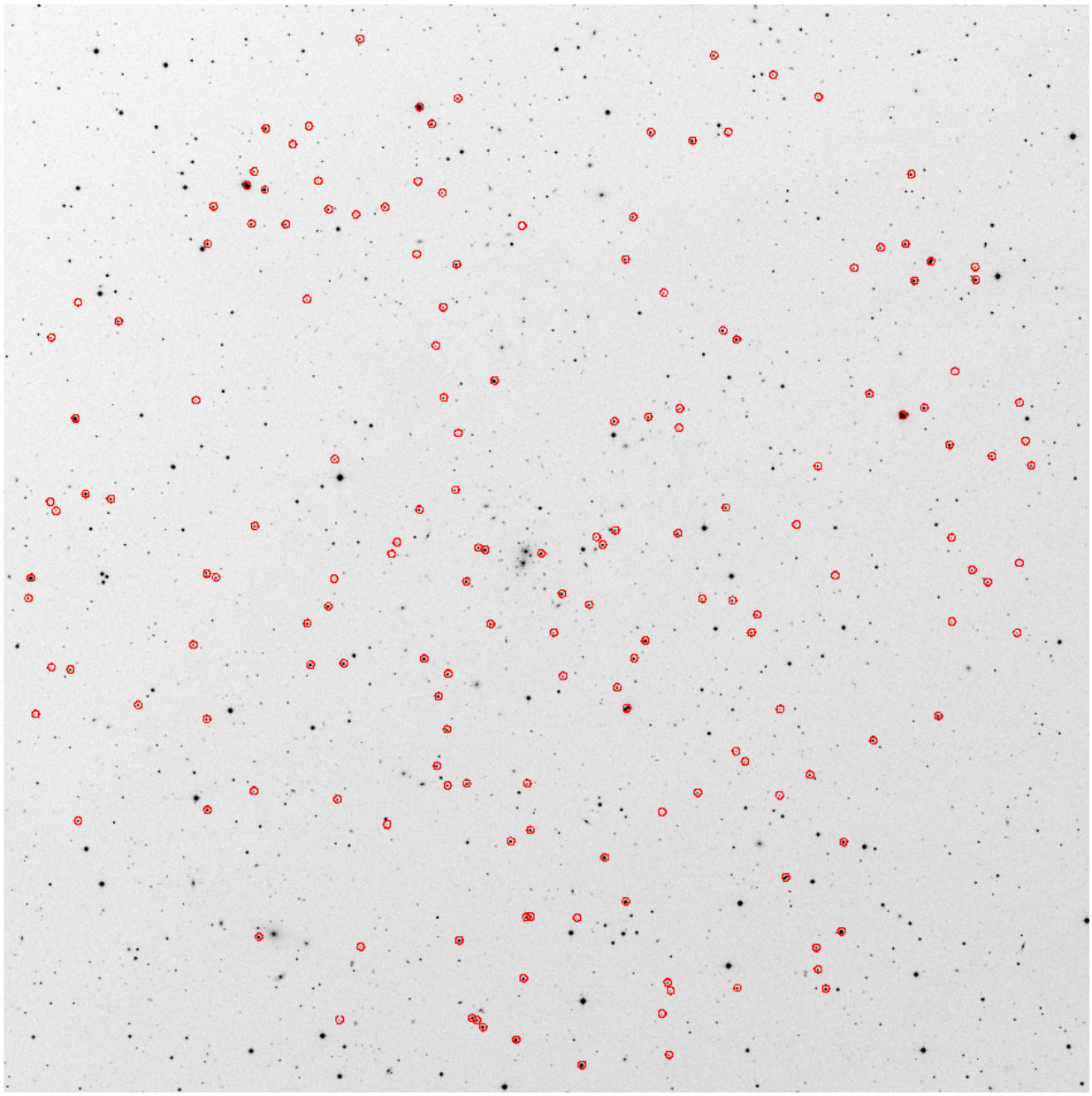

Figure 3.5: Stellar targets. The circled objects in this image are targets that were observed with radial velocities less than 100 km s^{-1}, which are determined to be stellar sources rather than galaxies. Note that the distribution of stellar detections appears to be relatively uniform across the image.

Cluster	Field	Ap	cz ($km\ s^{-1}$)	σ ($km\ s^{-1}$)
A154	3	33	18221.7	31.1147
A154	5	12	18208.2	29.0019
A104	2	31	15829.6	29.3034

Table 3.3: Emission reference spectra. These spectra were used as a references for correlating emission spectra in the data set.

Emission Line Galaxies

For a few objects, FXCOR was unable to correlate a fit between the reference and object spectra using absorption features. However, several objects have clear, strong emission features. Emission lines usually occur when planetary nebulae or interstellar gas is excited by ionizing radiation from a hot star, an active galactic nucleus, or even by the passage of a strong shock (Véron-Cetty & Véron, 2000; Binney & Merrifield, 1998). The three reference spectra do not contain strong emission features, and so FXCOR could not use this information during the routine. Like absorption lines, emission lines can also be used by FXCOR for correlation, but only if there are one or more reference spectra that exhibit both strong absorption features (thus producing a reliable fit with low uncertainty) as well as the strong emission features.

After separating emission-line galaxies from all the other spectra, 68 galaxies were identified that could be analyzed using the emission features. To do this, two galaxies were identified from the previously reduced data and one galaxy from a reduced Abell 104 data set that was also observed at KPNO during October of 1997. These galaxies represent radial velocities with the least correlation ambiguity – only one identifiable correlation peak – as well as the lowest uncertainties among galaxies with emission features. They also have both strong absorption and emission features. Properties of the emission reference spectra are presented in Table 3.3.

Using these three emission spectra as references for FXCOR, an additional 204 radial velocity measurements were collected, which corresponds to a total of 68 additional galaxies.

The strong emission lines relative to the noise allowed FXCOR to fit the object spectra with very small (emission) uncertainties. The (absorption) uncertainty of each reference spectrum cannot be ignored. The object (emission) uncertainty was combined with the reference (absorption) uncertainty by adding in quadrature as defined as (Bevington & Robinson, 2003),

$$\sigma_i = \sqrt{\sigma_e^2 + \sigma_a^2}, \tag{3.4}$$

where σ_i is the uncertainty for each radial velocity as based upon the uncertainties from the object's fit, σ_e, as well as from the reference's fit, σ_a. The 204 radial velocities from emission features (a measurement for each reference spectra) were processed using the sorting/combining routine as described in Section 3.1.3, which reduced the data to 68 emission line galaxies.

3.1.4 Reconciling Absorption- and Emission-Based Data

There are 147 galaxies from absorption-based data and 68 galaxies from emission-based data. When combining absorption- and emission-based data, 39 galaxies displayed both emission and absorption features. Out of those, all 39 absorption/emission pairs had Z-score values (Equation 3.1) less than or equal to 1, which was again interpreted as being consistent. These measures were then combined using weighted averages and uncertainties as previously described in Section 3.1.3. The net result is 176 unduplicated galaxy radial velocities.

3.2 Literature Data

A thorough literature search was performed, including data catalogs, over Abell 154 (see Table 3.4). Catalogs and articles that did not specify Abell 154 but had obtained data in the vicinity of Abell 154 were also included. A two degree radius from the center of the galaxy cluster (as defined by the location of the southern elliptical galaxy) was arbitrarily

ID	Reference	N
A	Faber & Dressler (1977)	12
B	Merrifield & Kent (1991)	18
C	Zabludoff et al. (1993)	3
D	Zabludoff et al. (1990)	3
E	Owen & Ledlow (1995)	1
F	Hamwey (1989)	19
G	Huchra et al. (2012)	4
H	Hoffman & Williams (1991)	14
I	Blakeslee & Tonry (1992)	3
J	Woods et al. (2006)	1
K	Huchra et al. (1983)	2
L	Giovanelli & Haynes (1993)	1
M	Wegner et al. (1999)	1

Table 3.4: Literature radial velocity sources. The first column presents the letter used for distinguishing literature data by reference. The third column is the number of galactic radial velocity measurements contained within those sources. Data from references F and I were obtained through the catalog by Huchra et al. (2012) and data from reference J was obtained from the catalog by Falco et al. (1999).

chosen for a measure to be considered in the vicinity of Abell 154. Most radial velocity measurements were accessible through the Vizier Service (Ochsenbein et al., 2000) or NED, but some data were transcribed directly from the article that presented it. In a few cases, the original paper did not present or publish the individual radial velocity measurements (Huchra et al., 1983; Hamwey, 1989; Woods et al., 2006). Comprehensive catalogues, such as Huchra et al. (2012) and Falco et al. (1999), were the sources of the missing data. Overall, a total of 13 publications with galaxy radial velocity measurements within two degrees from the center of the galaxy cluster Abell 154 were identified, see Table 3.4. Within those 13 references, there were a total of 82 radial velocity measurements for 62 galaxies.

The literature results were reduced by combining duplicated measurements using the same process that was described in Section 3.1.3. This resulted in 15 radial velocities that were mutually consistent and were successfully reduced. Galaxy 011103+173907 had four radial velocity measurements. Three out of the four radial velocities were mutually consistent with $Z < 1$. The fourth measure, however, was not consistent with any of the other three measures, having a Z-score value of 12.1. Based on the confidence of the other

three measurements, this measurement was eliminated from the data as an outlier.

However, 21 out of 36 duplicated radial velocity measurements were inconsistent, having Z-score values of $Z > 1$. A summary of this analysis is shown in Table 3.5. There are an expectedly large number of measures with $Z > 2$ (see proportions mentioned in Section 3.1.3), which could indicate a strong chance of some significant source of error in the literature. Each set of inconsistent measurements were reviewed – including the paper that presented them (except for Hamwey (1989)) – in search for a systemic error, but were unable to find any. Since 6 of the 9 galaxies with inconsistent measures include results from Hamwey (1989), it is possible that this reference contains a systemic error, but at present, this cannot be verified. Galaxy 011101+174047 was measured twice in the Hoffman & Williams (1991) study. Each measurement was considerably different, but both deviated significantly from the Merrifield & Kent (1991) radial velocity for the same galaxy.

For the 9 galaxies with $Z > 1$, measures are maintained for comparison with the new data in Section 3.3. If there is no match found in the new data, then the measure with the lowest uncertainty will then be kept for analysis.

3.3 Compilation of Data

3.3.1 Reconciling Literature Data with New Data

Compiling the 176 new galaxy radial velocity measures with the radial velocities for 62 galaxies from the literature, there were 33 galaxies with repeated measures. Of those 33 galaxies, 24 radial velocity measures were in agreement with a Z-score value $Z < 1$. The other 9 radial velocities had Z-score values that were $1 < Z \leq 2$. The distribution of Z-score values for all 33 galaxies is consistent with expectations from random sampling of measurements (see the proportions mentioned in Section 3.1.3).

When combining new data with the literature, any repeated measures with $Z < 1$ were combined using a weighted average and combining errors as was previously done in

Galaxy	RV Source	Z-score	$\sqrt{\sum \sigma_i^2}$
011110+174136	A, F	0.00, 0.00	141.4
010926+165738	J, K	0.01, 0.03	51.9
011110+180300	C, H	0.20, 0.05	109.1
011102+173933	A, B	0.24, 0.16	128.1
011103+173907	D, E, A, (B)	0.13, 0.26, 0.48, (12.1)	121.2
011058+173743	A, B	0.49, 0.31	128.1
011049+173903	A, F	1.02, 1.02	141.4
011131+173636	A, F	1.50, 1.50	141.4
011126+174035	A, F	1.63, 1.63	141.4
011039+173112	A, F	2.67, 2.67	141.4
011043+174100	A,H	3.67, 3.67	141.4
011104+173947	A, B, D	3.91, 12.3, 1.66	132.2
011109+175100	A, F	7.89, 7.89	141.4
011101+174047	B, H, H	10.9, 6.59, 10.8	106.8
011046+175927	F, H	16.3, 7.45	89.31
011047+173956	A, F	18.4, 18.4	141.4

Table 3.5: Literature self-consistency. This table summarizes the self-consistency among the literature values for the 36 repeated radial velocity measurements on 16 galaxies. Radial velocity source is based on the identifications presented in Table 3.4. For galaxy 011103+173907, one of the repeated measurements was significantly inaccurate with respect to the other three, so it was was not included in the Z-score calculation for the other three measurements. It is also excluded from the combined error that is represented in the last column. This reference and its Z-score value are indicated in parentheses and were excluded from the data set. Z-score values are listed in order with respect to the order of references. Galaxy 011101+174047 was actually measured twice by Hoffman & Williams (1991), but the measured radial velocities were very different.

Section 3.1.3. For repeated values where $Z > 1$, the literature data were discarded in favor of the new measurements which had a lower uncertainty in each of the nine cases and were otherwise self-consistent. The final data set was made up of the 152 distinct new measures, 24 measures that are a combination between the literature results and new data, and also 29 distinct measures from the literature for a total of 205 galaxies.

A map of Abell 154 and each detection has been provided in Figure 3.6. This image shows a circle for each galaxy that now has a radial velocity measurement. Further analysis is needed to determine the likelihood of cluster membership and the existence and quantification of any substructure within the cluster.

Another way to represent the data is to examine the frequency of distribution as a function of both right ascension and declination. A two dimensional histogram has been

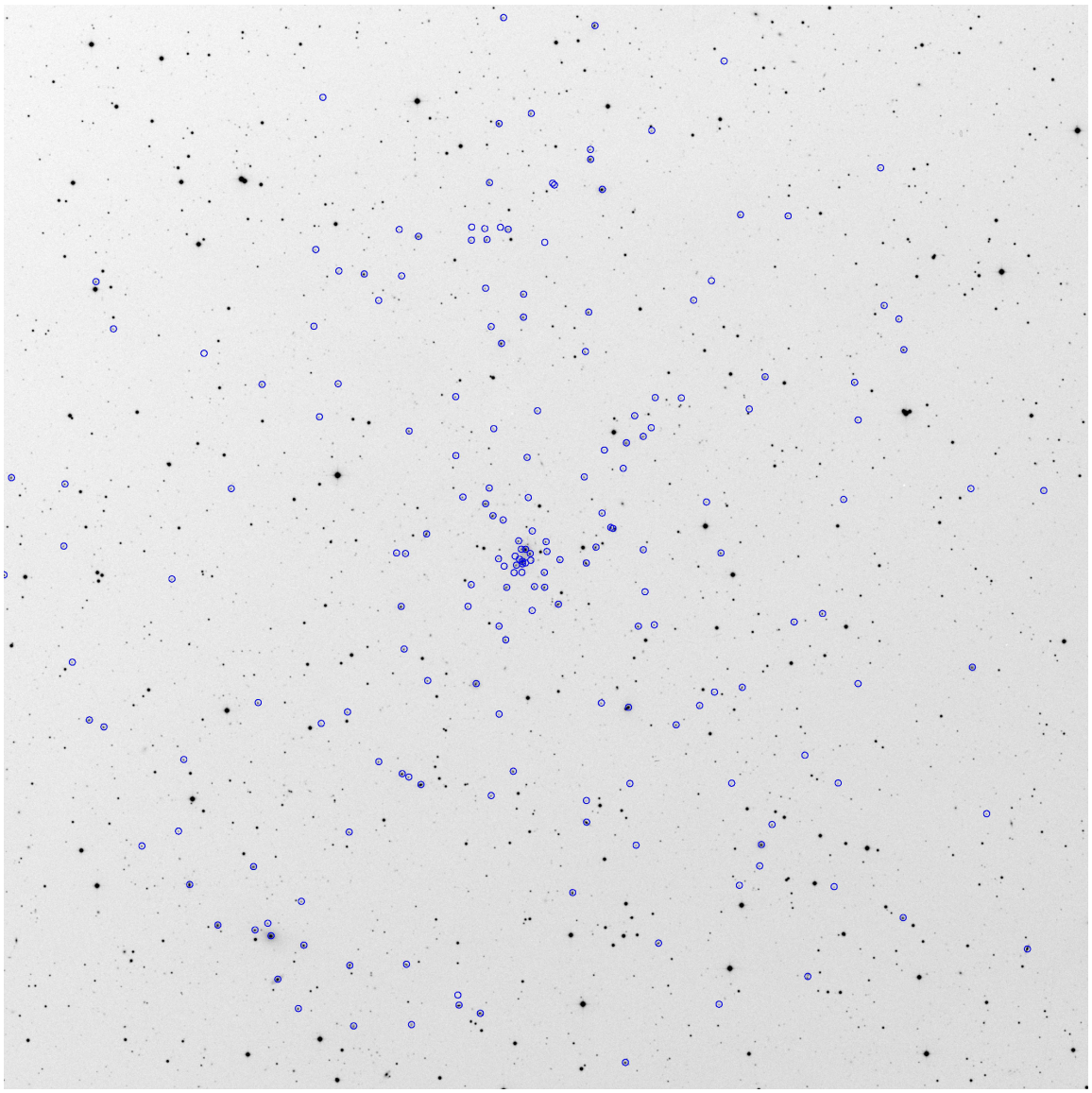

Figure 3.6: Galactic radial velocities in Abell 154. In this map of Abell 154, the circled objects are all of the galaxies that have a radial velocity measurement, including both literature results and new data.

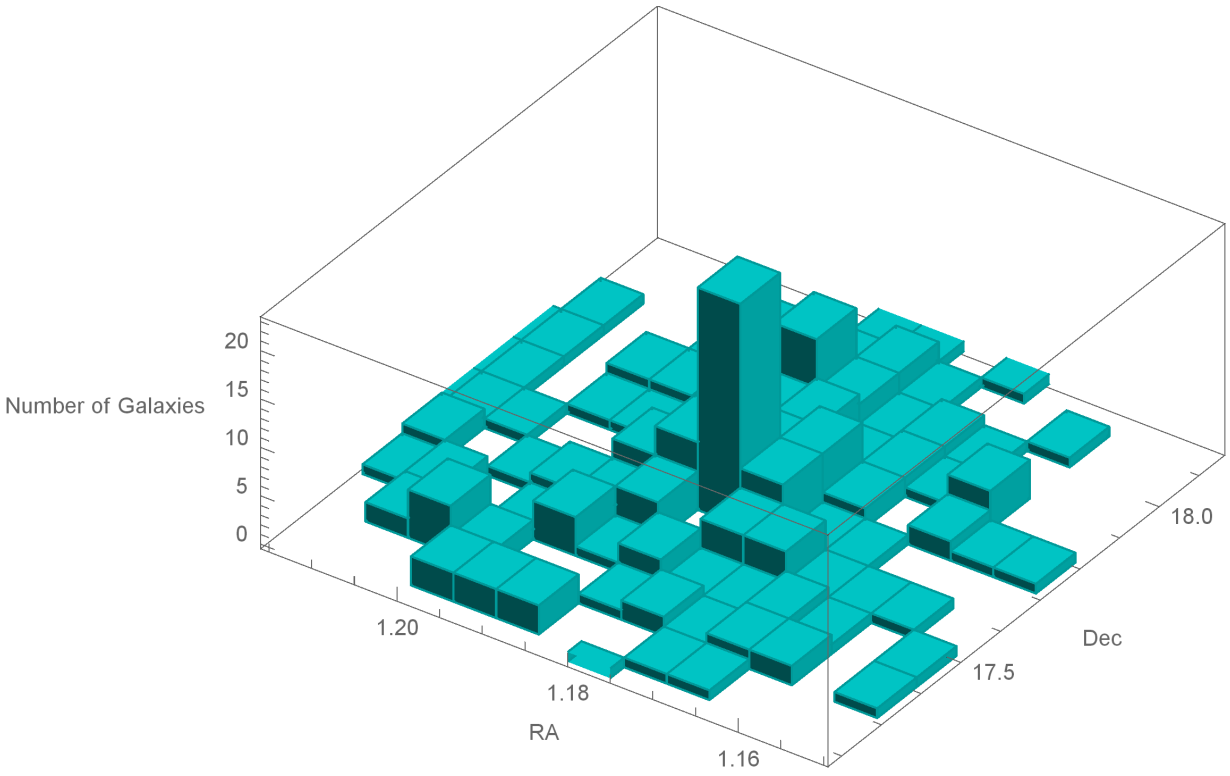

Figure 3.7: Abell 154 2D histogram. This is a two-dimensional histogram of the positions of galaxies. Right ascension (RA) is in decimal hours and declination (DEC) is in decimal degrees.

provided in Figure 3.7, showing number of galaxies as a function of right ascension (in hours) and declination (in degrees). From the image, a clear peak in the center represents the increased number density of galaxies found near the center of mass. Additional structure may be suggested by the variation of peaks across this image.

The overall combined data can be seen in the histogram in Figure 3.8. In this image, only the two main groupings of galaxies are presented, leaving out the distant background galaxies with extremely large redshifts. Previous results from the literature can be seen as shaded parts near the lower axis. As you can tell from this histogram, the new measurements presented here have greatly improved the amount of data that is available for statistical analysis.

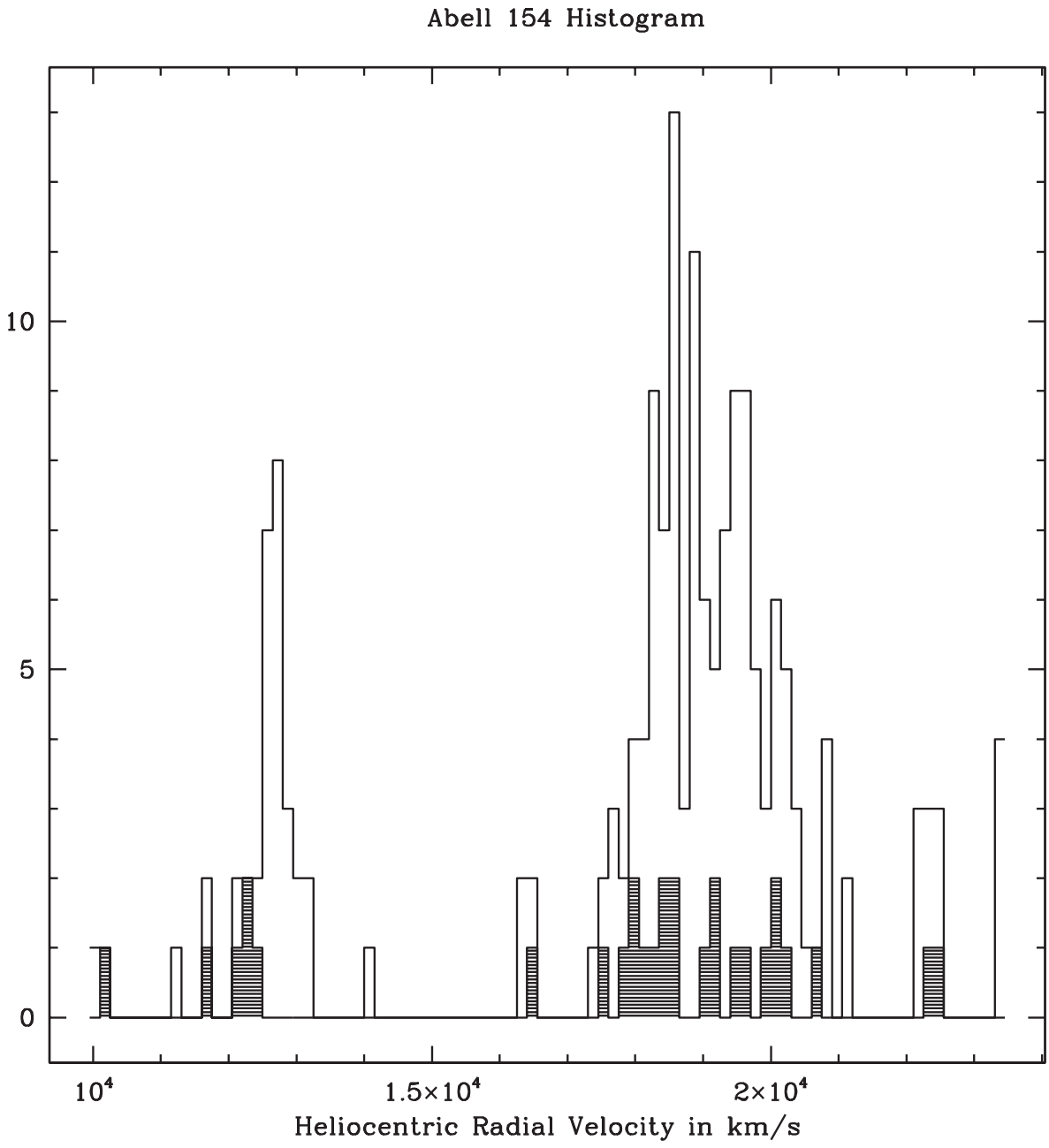

Figure 3.8: Abell 154 velocity histogram. This is a histogram of the radial velocities including both literature values (shaded) and previously unpublished radial velocities (unshaded). The current research greatly increased the number of radial velocity measurements for galaxies.

Chapter 4

Data Analysis And Discussion

Analysis of the 205 galaxies is presented in this chapter. By visual inspection, there appears to be a foreground group that stands out on the histogram in Figure 3.8, which would confirm the same findings by Struble & Rood (1991) and Zabludoff et al. (1993). Additionally, the two-dimensional substructure suggested by Kriessler & Beers (1997) will be analyzed. An analysis of the cluster in three dimensions will also be completed. Any identified potential substructure will be compared with multi-wavelength data for confirmation. The potential significance of identified structure will also be analyzed using gravitational binding tests.

4.1 Statistical Analysis

Statistical analysis of the data defines and quantifies the likelihood of substructure. One-dimensional analysis of the data will be based on the radial velocity distribution. Two-dimensional analysis of the data is based on the distribution of galaxies in right ascension and declination, which will be referred to as the position of the galaxies. Three-dimensional analysis will be based on the galaxy's radial velocity and position. The radial velocity distribution will be examined first, which can be seen in the histogram in Figure 4.1.

There appears to be several likely foreground and background galaxies, especially those with extremely high radial velocities. For analysis, the data were reduced to only those

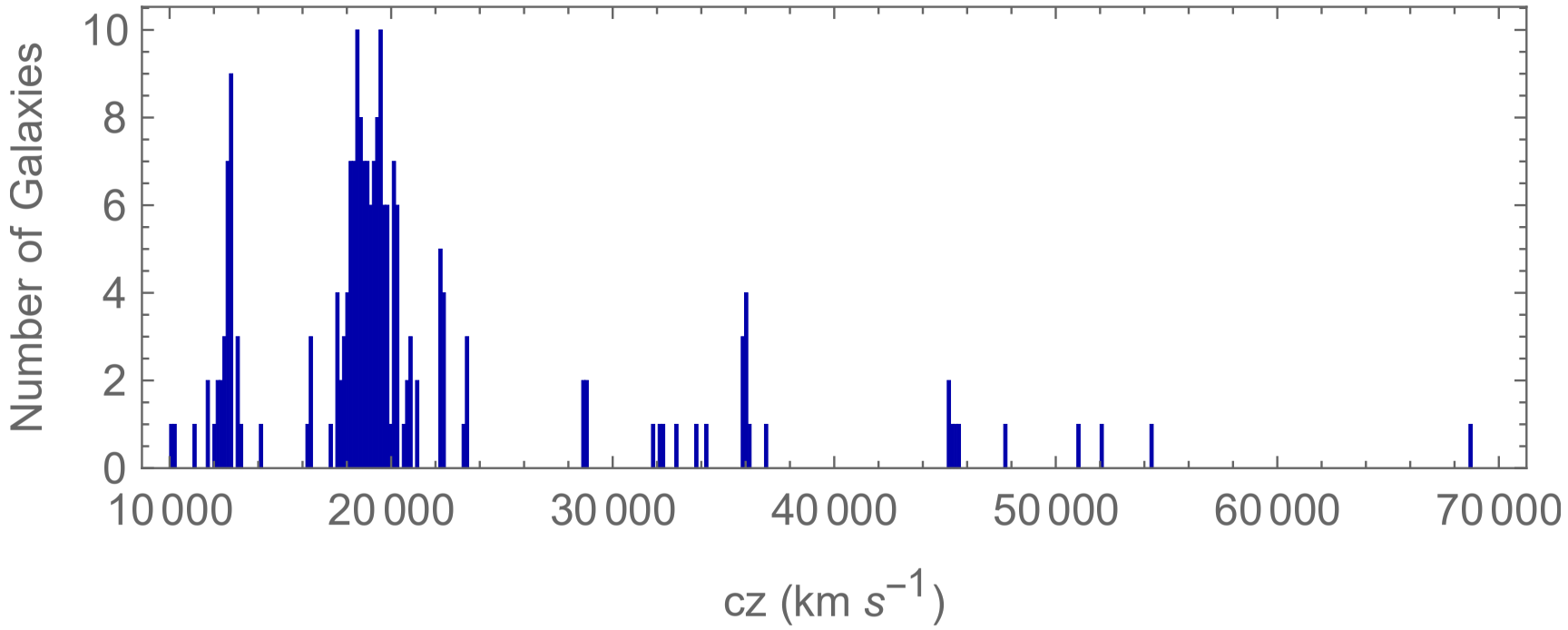

Figure 4.1: Abell 154 histogram. This plot presents the histogram of radial velocities measurements for galaxies in the vicinity of Abell 154.

galaxies that are potential members of the cluster. One method to eliminate foreground and background galaxies from analysis is to use the large gaps between galaxies, as proposed by Zabludoff et al. (1993). A more objective approach is to use a 3-σ clipping routine that recursively removes any galaxies with radial velocities that are more than three standard deviations from the mean velocity (Yahil & Vidal, 1977).

4.1.1 3-σ Clipping

A 3-σ clipping routine removes galaxies with radial velocities that are more than 3 standard deviations from the group mean (Zabludoff et al., 1990). To do this, the entire distribution of galaxies is processed by radial velocity and a mean is calculated by

$$\bar{v} = \frac{\sum v_i}{N}, \tag{4.1}$$

where v_i is the radial velocity of the galaxy, $\bar{v}$ is the average radial velocity, N is the number of galaxies. The standard deviation for the distribution is also calculated by

$$\sigma = \sqrt{\frac{\sum (v_i - \bar{v})^2}{N - 1}}, \tag{4.2}$$

where σ represents the standard deviation of the radial velocity distribution. The Z-score value was previously defined in Equation 3.1, but for convenience, the Z-score value, Z, is redefined in terms of the variables used in Equations 4.1 and 4.2 as

$$Z = \frac{|v_i - \bar{v}|}{\sigma}. \tag{4.3}$$

Any galaxies with Z-score values 3 and above are removed. The removal of galaxies will result in the remaining distribution's mean and standard deviation changing, and so the routine is repeated. The process is repeated until all galaxies that are left fall within 3-σ deviation from the mean. The resulting histogram is shown in Figure 4.2. It was surprising to see that the foreground group is within the 3-σ cut-off for this routine. However, the

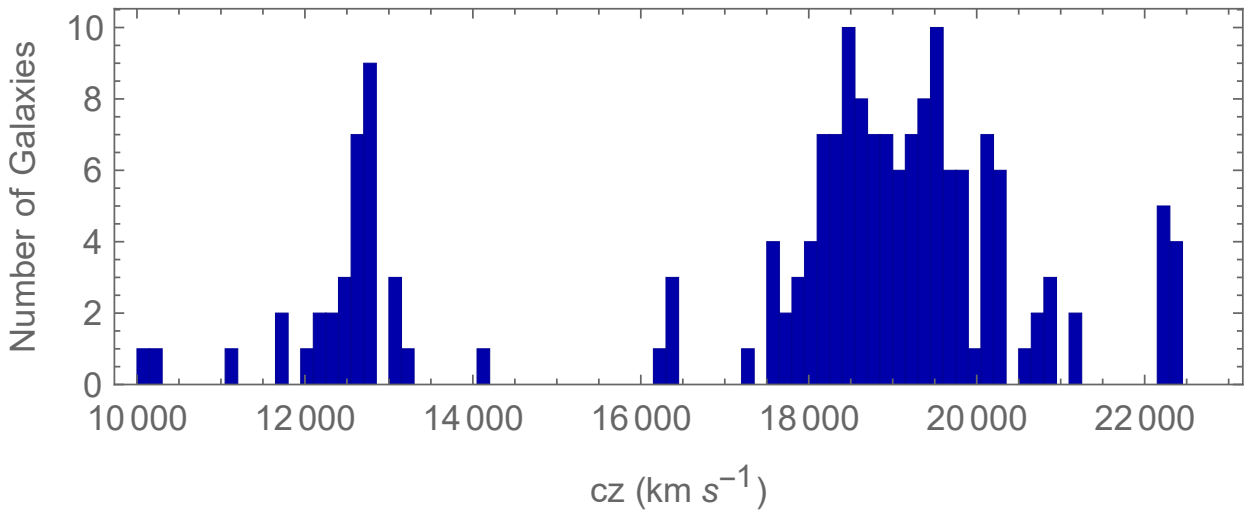

Figure 4.2: Initial 3-σ histogram. Histogram of radial velocities for galaxies following the 3-σ clipping routine when using the classical estimation of mean.

classical mean was used (see Equation 4.1), which does not handle central gaps in the data as well as other methods (Beers et al., 1990; Wainer & Thissen, 1976), such as using the median or the mode of the data as a measure of central tendency.

The bimodal appearance and velocity difference between the peaks (Δv $\approx$ 7000 km s^{-1}) suggests that these are independent groups and are unlikely to be gravitationally interacting (as will be verified later in Section 4.5.2). However, for consistency and reproducibility, the analysis of the distribution of galaxies through the Gaussian Mixture Model (GMM) algorithm and the KMM algorithm were used to identify potential substructure (Muratov & Gnedin, 2010; Ashman et al., 1994).

The KMM and GMM algorithms are used to identify and quantify potential membership of galaxies to overlapping groups within a cluster. In Chapter 2, the KMM algorithm was briefly described in the context of the study by Kriessler & Beers (1997) that sought to identify structure in two dimensions. KMM is able to process data using multiple dimensions simultaneously. However, the algorithm is notably less reliable for heteroscedastic groups, which are groups that have different variances (Muratov & Gnedin, 2010). The GMM algorithm was designed to reliably analyze a distribution with heteroscedastic groups. However, the GMM algorithm can only analyze a distribution in one dimension. Both algorithms were

used for consistency. Both algorithms use Gaussian distributions to evaluate the likelihood of membership (Ashman et al., 1994; Muratov & Gnedin, 2010). Radial velocity distributions are expected to appear nearly Gaussian for a relaxed cluster, but right ascension and declination are not. However, according to Kriessler & Beers (1997), a Gaussian is a good approximation in order to locate potential substructure.

KMM and GMM also report the statistical significance of the results using a p-value. For KMM, the algorithm calculates the likelihood of a unimodal distribution and the likelihood of a distribution with a user-defined number of groups, the ratio of which is compared to a χ^2 distribution to obtain a p-value (Ashman et al., 1994). By convention, a p-value of 0.05 or less indicates statistically significant deviation from a unimodal condition (Ashman et al., 1994). The p-value, however, is notably unreliable for heteroscedastic conditions (Muratov & Gnedin, 2010), especially when analyzing two or more dimensions simultaneously (Muratov & Gnedin, 2010; Ashman et al., 1994).

For the GMM algorithm, a parametric bootstrap technique is employed to evaluate the significance of the results (Efron & Tibshirani, 1986). In the case of GMM, which evaluates only one dimension of data, the bootstrap technique uses the original data's average value and standard deviation to randomly draw a test sample with the same number of objects (Muratov & Gnedin, 2010; McLachlan, 1987). The sample is drawn from a unimodal Gaussian distribution (Muratov & Gnedin, 2010) with repetition permitted. The original data is then compared to the random sampling and an evaluation is made. For GMM, the evaluation includes a χ^2 test as well as a log-liklihood ratio test. The bootstrap technique is then repeated thousands of times. Ultimately, by comparing the likelihood results of the input distribution to the test distributions, a p-value can be determined (Muratov & Gnedin, 2010; Efron & Tibshirani, 1986).

Tables 4.1 and 4.2 present results from these analyses based on sorting galaxies into two groups and three groups within the distribution, respectively. The first column for both tables gives the label for each group. The second and third columns present the number of

	KMM 1-D		GMM		KMM 3-D	
	n	$\bar{v}$	n	$\bar{v}$	n	$\bar{v}$
Group A	34	12449 km s^{-1}	34	12449 km s^{-1}	34	12449 km s^{-1}
Group B	142	19354 km s^{-1}	142	19354 km s^{-1}	142	19355 km s^{-1}

Table 4.1: KMM and GMM two group analysis. KMM and GMM reported all results as statistically significant (p-values less than 0.05). Each routine also presented the same two-group systems.

	KMM 1-D		GMM		KMM 3-D	
	n	$\bar{v}$	n	$\bar{v}$	n	$\bar{v}$
Group A	34	12449 km s^{-1}	34	12450 km s^{-1}	34	12450 km s^{-1}
Group B	133	19171 km s^{-1}	129	19027 km s^{-1}	99	18912 km s^{-1}
Group C	9	22305 km s^{-1}	13	22642 km s^{-1}	43	20073 km s^{-1}

Table 4.2: KMM and GMM three group analysis. KMM and GMM reported all results as statistically significant (p-values less than 0.05), however, they did not report consistent values.

galaxies and the average radial velocity for each group with respect to the one dimension KMM algorithm. The next two columns present the number of galaxies and average radial velocity of each group with respect to the GMM algorithm. Finally the last two columns present the number of galaxies and average radial velocity with respect to the three dimension KMM algorithm. Analyses based on four, five and six groups were considered, but KMM and GMM did report statistically significant results.

The GMM and KMM results (see both Tables 4.1 and 4.2) are consistent with the foreground 34 galaxies having been drawn from a separate distribution than the remaining galaxies. This provide confidence that the foreground 34 galaxies could be isolated for analysis as a foreground group (Group A) and the remaining 142 galaxies can then be isolated as the main group (Group B). These isolated groups were processed individually with the 3-σ clipping routine again, resulting in the foreground group with 28 galaxies and the main group with 125 galaxies. The number of galaxies, average velocity, velocity dispersion and assigned color for figures for each group is presented in Table 4.3.

The positions of galaxies are presented in Figure 4.3. The overall positional distribution is displayed in Figure 4.4. Those that remained after the initial 3-σ clipping routine is shown in Figure 4.5. Each group is displayed in Figures 4.6 and 4.7. In these two-dimensional

	n	$\bar{v}$	σ	Color
Group A	28	12659 km s^{-1}	261.706	Green
Group B	125	19106 km s^{-1}	807.189	Blue

Table 4.3: Identified groups. Please note that the color column is in reference to the color that the group has on the various figures in this chapter. Also in those figures, there are orange colored dots that represent galaxies that did not survive the 3-σ clip.

histograms, additional patterns within each group is not easily observed. Figure 4.8 presents right ascension and declination as a function of radial velocity. Please note that the different colors represent the different groups: Group A is in Green, Group B is in Blue, and any other galaxy is colored orange.

4.1.2 Gaussian Fitting

With two groups identified, each group can be analyzed for conformity to a Gaussian curve in velocity space. The statistics that are being used in this dissertation are presented in Table 4.4. Relaxed clusters should be well-approximated in one dimension by a Gaussian curve, except for the maximum and minimum values which have been truncated due to the 3σ-clipping process. Table 4.4 includes the number of input dimensions, references to the literature and the type of sensitivity of the statistic. The results of these statistical analyses are presented in Table 4.5. For comparison, the same statistical analyses were run on the unclipped data, the results of which are also found in Table 4.5.

Each one-dimensional statistic is calculated from an attempted fit of a Gaussian curve to the data. The null hypothesis for each test is that the data fits a Gaussian distribution, which means that these tests seek to identify distributions that are statistically significant deviations from fitting a Gaussian distribution. For most statistical tests, the crucial factor for interpretation is the p-value. The p-value given for statistics represents the probability of conformity to a random Gaussian distribution. As stated previously, by convention, a p-value of less than 0.05 is considered statistically significant (Ashman et al., 1994), which corresponds to results that deviate from the expectations by more than two standard devia-

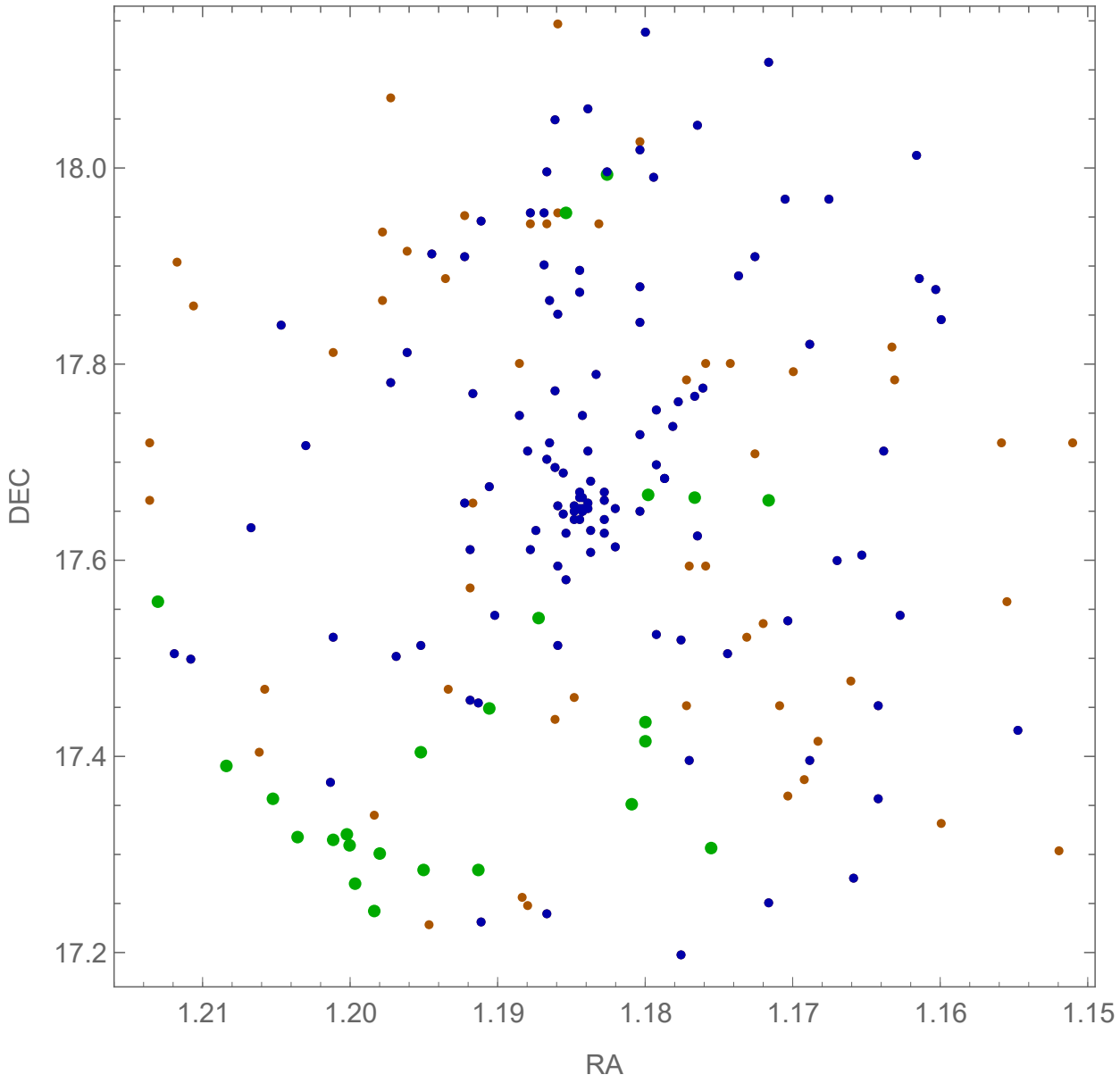

Figure 4.3: Abell 154 by group. Please note that the different colors represent different groups. The main group of galaxies (Group B) can be seen with blue dots and the foreground group (Group A) of galaxies can be seen in green dots. Orange dots represent galaxies that were left out by the clipping routine. They may be field galaxies, or they may be cluster members with uniquely extreme radial velocities that did not survive the 3-σ clipping routine.

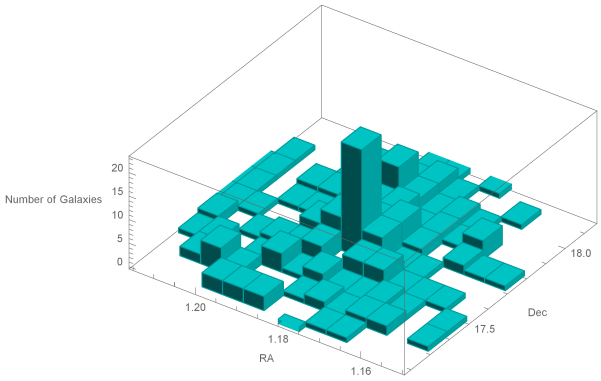

Figure 4.4: Histogram of the positions of all 205 galaxies with radial velocity measurements.

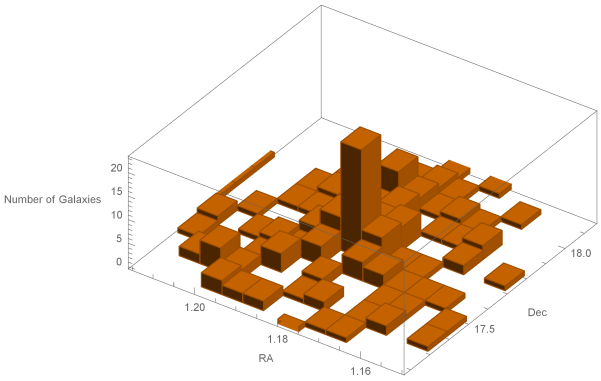

Figure 4.5: Histogram of the positions of galaxies. This image includes all 176 galaxies that survived the initial 3-σ clipping routine.

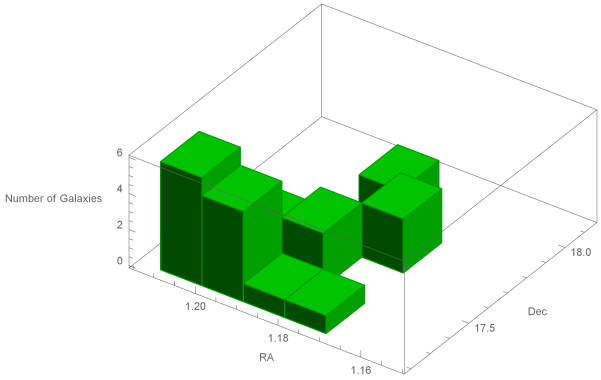

Figure 4.6: Histogram of the positions of Group A galaxies. This group is most concentrated in the southeast but also spreads from to the northwest. Please note that the bin size in this histogram has been increased to accommodate the small sample size.

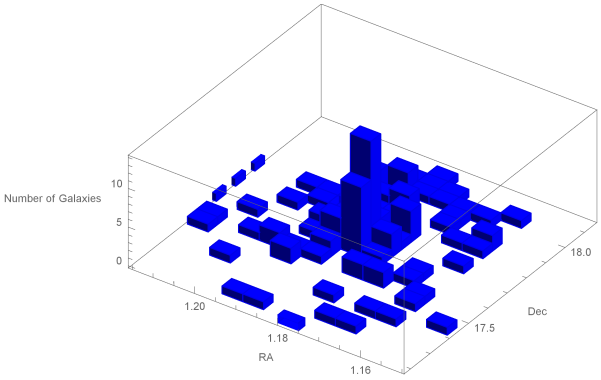

Figure 4.7: Histogram of the positions of Group B galaxies. The cluster has a strong peak, but there appears to be asymmetric appearance in number density immediately north and northwest of the central peak. This also corresponds to the results observed previously by Kriessler & Beers (1997).

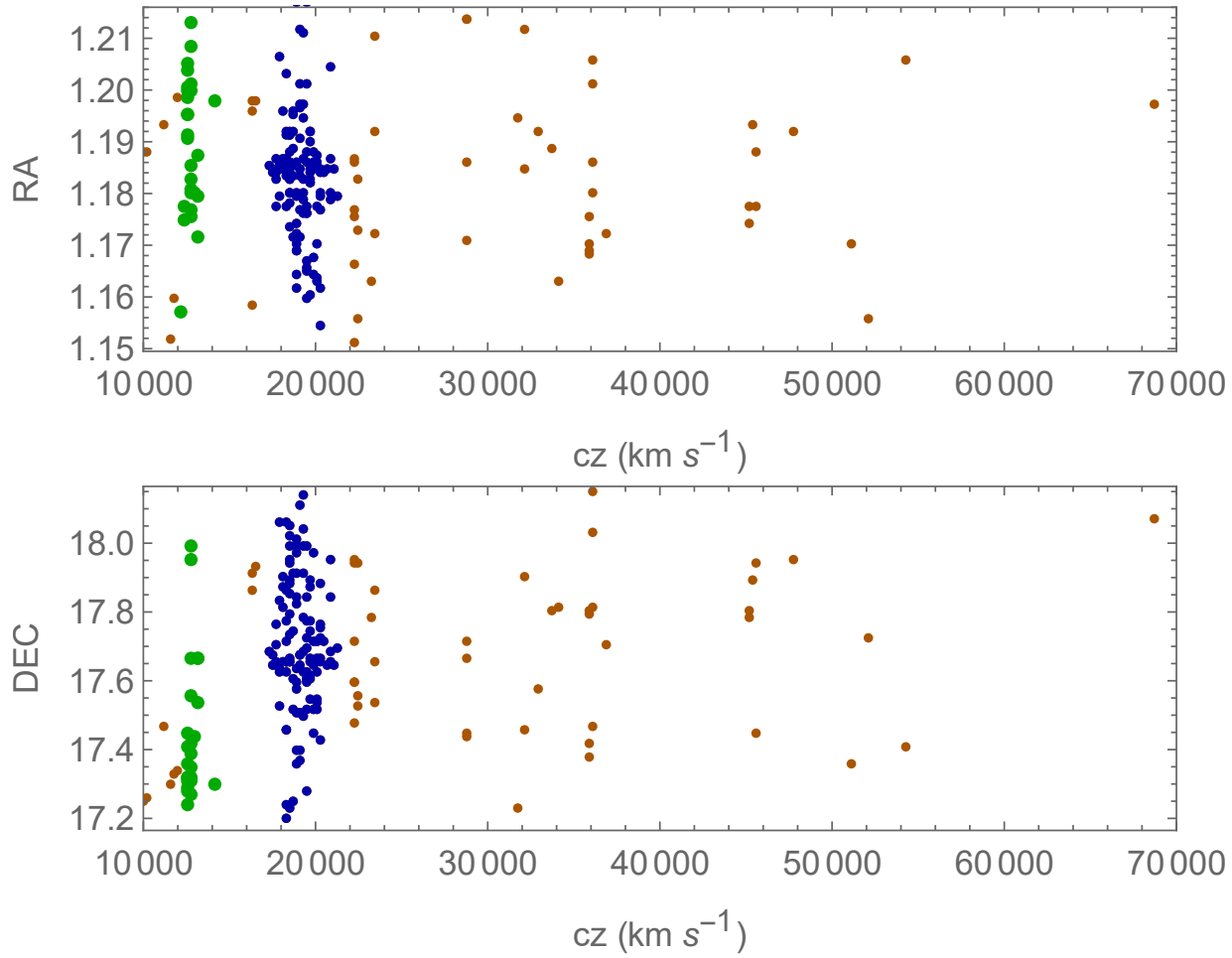

Figure 4.8: Right ascension (top) and declination (bottom) as a function of radial velocity (horizontal axis). The main group (Group B) can be seen with blue dots and the foreground group (Group A) can be seen in green dots. As can be seen, the green group is concentrated southeast of the cluster. Orange dots represent galaxies that may be more likely to be field galaxies rather than cluster members.

Statistical Test	Dim.	ref.	Sensitivity
A	1	1, 2, 3	Long-Tailed Distributions
A^2 (Anderson-Darling)	1	3, 4, 6	Tail Deviations of EDF
B_1 (Skew)	1	3, 5, 6	Asymmetric Distributions
B_2 (Kurtosis)	1	1, 3, 5	Symmetry and Flat/Acute Distributions
B_1B_2 (Omnibus)	1	3, 6	Asymmetry and Flat/Acute Distributions
I Omni	1	3, 7	Symmetric Long-Tailed Distributions
U	1	1, 3, 4	Abrupt Tail Cut-off Distributions
U^2 (Watson)	1	3, 4, 6	Deviations of EDF
V (Kuiper)	1	3, 4, 6	Supremum Deviation of EDF
W (Shapiro-Wilk)	1	1, 3, 8	Long-Tailed Distributions
W^2 (Cramer Von Mises)	1	3, 4, 6	Central Deviations of EDF
DIP	1	3, 9	Multimodality
Grubbs	1	10	Outlier Data Points
Komologorov-Smirnov	1	3, 4, 6	Supremum Deviation of EDF
Fourier Elongation	2	11, 12	Spatial Elongation
Lee 2D	2	11, 13, 14	Spatial Bimodality
α	3	11, 15	Centroid Change with Velocity
Δ	3	11, 16	Mean Velocity and Dispersion Change with Position
ϵ	3	5, 17	Projected Mass Estimator Change with Position
Lee 3D	3	11, 13, 14	Positional Bimodality

Table 4.4: Statistical tests. The second column indicates the number of dimensions of the input data. The third column provides a reference from the literature of its use. The fourth column describes the kind of deviation from a Gaussian distribution to which the statistical test is most sensitive. The probabilities EDF is the Empirical Distribution Function and is always compared to the the Cumulative Distribution Function of a normal distribution. References — (1) Yahil & Vidal, 1977; (2) Pearson & Hartley, 1962; (3) Beers et al., 1990; (4) Stephens, 1974; (5) Bird, 1994; (6) D'Agostino & Stephens, 1986; (7) Iglewicz, 1983; (8) Shapiro & Wilk, 1965; (9) Hartigan & Hartigan, 1985; (10) Grubbs, 1950; (11) Pinkney et al., 1996; (12) Rhee et al., 1991; (13) Fitchett, 1988; (14) Lee, 1979; (15) West & Bothun, 1990; (16) Dressler & Shectman, 1988; (17) Heisler et al., 1985

tions. A value of 0.05 to 0.10 will also be considered marginal or marginally significant, also by convention (Ashman et al., 1994), but any value higher than 0.10 should be considered inconclusive.

For most statistics, the p-value is either calculated independently or is calculated through a bootstrap technique, and each is given in Table 4.5. For one dimensional tests in particular, the p-value is usually calculated using a previously determined goodness-of-fit estimator, see references in Table 4.5 for further details. A p-value of 0.05 or smaller indicates a statistically significant deviation from the expected statistical results of a Gaussian distribution.

In Table 4.5, $\bar{v}$ and σ were given primarily for information purposes. In the next row, the A test, there was no p-value available for the distribution. For the U test, p-values were drawn from tables found in Pearson & Stephens (1964). To interpret the results, these statistics are examined separately.

The A test is a check for normality and/or outliers found in the extremes of radial velocities. The statistic results in a value of 0.798 when testing a normal distribution. A much lower value for the A statistic would suggest a distribution with radial velocities that are abnormally lengthened to the extremes. It can be seen in the values in Table 4.5 that the 205 galaxy set clearly has a lower result than either of the groups, which should be expected since the groups were created with a 3-σ clipping routine to remove values at the extremes. Without any other information, the null result is assumed – the A test is not a statistically significant deviation from a Gaussian for Group A or Group B.

The U test is a also a statistic that is impacted by values at extremes (Yahil & Vidal, 1977). Though there are p-values for this statistic, the significance of the results must be considered. In this statistic, the results change by the number of radial velocities in the data set. A significantly high statistic value, as can be seen in the All Galaxies, 205 galaxy data set, in the final set of columns, which suggests a result that has contamination by extreme values. For low statistic values, such as is seen in Groups A and B in Table 4.5, the

Statistic	Group A $n = 28$		Group B $n = 125$		All Galaxies $n = 205$	
	Value	p	Value	p	Value	p
$\bar{v}$	12659	-	19107	-	21021	-
σ	261.7	-	807.2	-	8644	-
A	0.754	-	0.827	-	0.620	-
A^2	0.307	0.563	0.481	0.232	**21.26**	**0.000**
B_1	-0.185	0.319	0.266	0.104	**2.378**	**0.000**
B_2	2.848	0.624	*2.474*	*0.084*	**9.881**	**0.000**
B_1B_2	0.321	0.852	3.486	0.175	**120.2**	**0.000**
I	0.970	>0.10	0.944	>0.10	**11.345**	**$\ll$0.05**
U	4.121	>0.10	*4.517*	*0.05<p<0.10*	**6.786**	**0.01<p<0.025**
U^2	0.047	0.509	0.069	0.254	**3.881**	**0.000**
V	0.159	0.504	0.096	0.314	**0.442**	**0.000**
W	0.974	0.718	*0.969*	*0.076*	**0.723**	**0.000**
W^2	0.048	0.539	0.077	0.229	**4.312**	**0.000**
DIP	**0.0408**	**0.011**	*0.024*	*0.076*	**0.051**	**0.000**
Grubbs	2.184	0.323	2.434	0.861	**5.514**	**0.000**
K-S	0.112	0.875	0.065	0.666	**0.292**	**0.000**
Fourier	1.573	0.298	**3.018**	**0.019**	**3.582**	**0.004**
Lee 2D	**5.132**	**0.001**	1.565	0.293	1.466	0.313
α	**0.261**	**0.033**	**0.122**	**0.001**	0.104	0.271
Δ	**49.07**	**0.001**	**170.5**	**0.005**	**417.9**	**0.000**
ϵ ($\times 10^{15}$)	0.408	0.532	2.01	1.000	395	0.255
Lee 3D	**5.085**	**0.015**	2.245	0.514	**2.826**	**0.008**

Table 4.5: Statistical results. Statistics for Group A, Group B, as well as the overall distribution. Emboldened figures represent statistically significant deviations from a Gaussian distributions as defined by p<0.05. Italicized figures represent deviations from a Gaussian distribution that are marginally significant as defined by 0.05≤p≤0.10. The U test uses Pearson & Stephens (1964) for p-values derived therein.

statistic indicates a steep tail or an abrupt cutoff as compared to a Gaussian distribution. Again, these results are expected since the groups were created with a 3-σ clipping routine to remove values at the extremes. Therefore, these results are considered as inconclusive for Groups A and B. In the remaining one-dimensional statistics, the resulting p-values clarify each group's conformity to a Gaussian distribution.

One-dimensional results where the p-value is less than 0.05 are emboldened in Table 4.5 as statistically significant deviation from a Gaussian distribution. For Group A, only the DIP statistical test indicates a strong deviation from a Gaussian distribution. For

Group B, none of the one-dimensional tests indicates strong deviation from a Gaussian distribution. However, four additional tests indicate marginally significant deviation from a Gaussian distribution (DIP, W, B_2, U). These values are italicized in the table.

4.1.3 Analysis in Two and Three Dimensions

For two- and three-dimensional statistics, each statistic analyzes the azimuthal or spherical symmetry, respectively. The null-hypothesis is that the distribution should be azimuthally/spherically symetric. Deviation from symmetry is seen in the clumping of galaxies, where the number density of galaxies is enhanced disproportionately. Each of the two- and three-dimensional tests will examine and quantify this clumpiness.

However, the existence of clumpiness is not sufficient to indicate potential substructure. A random sample of a spherically symetric distribution could show some clumping as a result of a systemic bias in the sample. To evaluate deviation from azimuthal symmetry, a bootstrap technique is needed again. In this case, the sample cannot be drawn from a Gaussian distribution since the azimuthal distribution of a galaxy cluster is not Gaussian (Kriessler & Beers, 1997; Ashman et al., 1994). Instead, a routine that randomly shuffles data is used. For two-dimensional data, the azimuthal angle of each galaxy is randomized while maintaining each galaxy's distance from the centroid that is calculated from the positions of the galaxies. For three-dimensional data, the radial velocities of each galaxy are shuffled relative to their positions. If the clumpiness of the original data is significant, shuffling results in the creation of a sample that is more randomly distributed and less clumpy. Therefore, a p-value can be created by determining the number of samples that are more clumpy than than the original data. Once again, 10^5 samples are used, so a p-value of 0.05 would mean that only 5000 samples were more clumpy than the original data out of 100,000 samples.

Two- and three-dimensional statistics where the p-value is less than 0.05 are emboldened in Table 4.5 as statistically significant deviation from azimuthal or spherical symmetry.

For Group A, four statistical tests (α, Δ, Lee 2D, Lee 3D) indicate a strong deviation from a Gaussian distribution. For Group B, only three statistical tests (α, Δ, Fourier) indicate strong deviation from a Gaussian distribution.

4.1.4 Statistical Rejections

For Group A and Group B, several tests rejected the null hypothesis of a match to a Gaussian distribution. In each of these tests, an overview of the tests' sensitivity is necessary to understand the significance of the rejection.

- **DIP Test** – The DIP test is an analysis of the distribution's potential departure from unimodality in velocity space (Hartigan & Hartigan, 1985). It is an analysis of the likelihood of finding a dip in the distribution function and an analysis of the strength of the dip. A stronger dip is one that has a more significant contribution to additional modes, or peaks in the frequency distribution, instead of a single mode or peak for the distribution. The null hypothesis of this test is that there exists precisely one mode or frequency peak for the distribution. A rejection of this statistic would suggest that the distribution has more than one mode and therefore departs from a Gaussian distribution.

  For Group A, which exhibits this statistical rejection, there is a large gap between the first three galaxies and the remaining 25 galaxies. The size of the gap, relative to the number of data points before and after the gap, impacts the statistic considerably. The DIP test rejection for Group A appears to be primarily due to the small number of data points creating an artificially significant effect.

- α **Test** – The α test is a three dimensional analysis of the shift of the local centroid as a function of radial velocity relative to the global centroid (West & Bothun, 1990). Significant shifts of the local centroid from the global centroid is a strong indicator of substructure, but this test may give less significant results if substructure is superim-

posed (i.e., the local and global centroids have similar positions). The α statistic is calculated by West & Bothun (1990)

$$\alpha = \frac{1}{N} \sum_{\mathrm{i=1}}^{\mathrm{N}} \delta_i, \tag{4.4}$$

where N is the total number of galaxies in the distribution, and δ_i for any galaxy is calculated by

$$\delta_i = \sqrt{(x_{\mathrm{global}} - x_{\mathrm{local}})^2 + (y_{\mathrm{global}} - y_{\mathrm{local}})^2}, \tag{4.5}$$

where x_{local} and y_{local} is the local centroid, or centroid of the nearest neighbors in position, and x_{global} and y_{global} is the (global) centroid of all the galaxies in the distribution. The global centroid is unweighted, but the local centroid is weighted by the inverse of the velocity dispersion of the nearest neighbors. The statistic uses the square root of the total number of galaxies to identify the nearest neighbors in position as local, as suggested by Bird (1994).

The α statistic for Group A uses the 5 nearest galaxies in position as local neighbors. For Group A, the spread of the 28 galaxies in position explains much of the significance of the test, but it cannot rule out the possibility of underlying structure in Group A. For Group B, the 11 nearest galaxies in position are considered local. The significance of this test suggests the centroid shift of the local galaxies correlate with the radial velocity distribution and that there is some underlying structure that should be explored more thoroughly. The results of this test suggest that this structure in Group B is not highly superimposed in position.

- Δ **Test** – The Δ test is similar to the α test in that it is a search for localized spatial-velocity correlation West & Bothun (1990). The Δ statistic is calculated by (Dressler & Shectman, 1988)

$$\Delta = \sum_{\mathrm{i}=1}^{N} \delta_i, \tag{4.6}$$

where δ_i for any galaxy is calculated by

$$\delta_i = \sqrt{\frac{N}{\sigma^2}[(\bar{v}_{\mathrm{local}} - \bar{v}_{\mathrm{global}})^2 + (\sigma_{\mathrm{local}} - \sigma_{\mathrm{global}})^2]}, \tag{4.7}$$

where N is the total number of galaxies, $\bar{v}_{\mathrm{local}}$ is the average radial velocity of the nearest neighbors, $\bar{v}_{\mathrm{global}}$ is the average radial velocity of the distribution, σ_{local} is the velocity dispersion of the nearest neighbors, and σ_{global} is the velocity dispersion of the distribution. This test is sensitive to differences between local velocity structure (averages and dispersions) from the global velocity structure. This statistic also uses the square root of the total number of galaxies as the number of galaxies to be considered local. For Group A, which again uses the 5 nearest galaxies as its local neighbors, any galaxy that deviates significantly in velocity space results in a large impact to it's nearest 5 neighbors. Additionally, the three foreground galaxies that are separated in velocity space are also contributing significantly to this statistic. The results for Group A are inconclusive.

For Group B, the significance of this test is not detrimentally impacted by the number of galaxies. There is a large number of galaxies with a local velocity structure (averages and dispersions) that differs from the global structure. Analysis of Group B with the Δ statistic uses 11 nearest neighbors to calculate local velocity structure. This can be seen visually in Figure 4.12, where a group of bubbles appears larger near the center of the figure relative to the size of bubbles in other locations. The large bubbles indicate values where the δ_i statistic is larger relative to galaxy's nearest neighbors, indicating a larger difference in average velocity or velocity dispersion between local and global values. This location will be examined in more detail as a location for potential substructure.

- **Fourier Test** – The Fourier Elongation test is sensitive to ellipticity or elongation of a distribution across two dimensions (Pinkney et al., 1996). Group B exhibits elongation to the North and West of the cluster center, giving Group B statistically significant results for the elongation test and suggesting that substructure is prevalent. This also appears to confirm results from Kriessler & Beers (1997) where structure was identified in two dimensional analyses.

- **Lee 2D/3D Tests** – The Lee two-dimensional test analyzes the potential clumpiness of the distribution in connection to bimodality based on position (Lee, 1979; Pinkney et al., 1996). The Lee three-dimensional test extends the test to a third dimension, analyzing radial velocity as well as position (Fitchett, 1988). Both statistics appear to be significant for Group A galaxies, suggesting that the structure of Group A is bimodal. However, the low number of data points causes this result to be suspect due to the fact that only a few galaxies can make a clump. In comparison of the Lee 2D results to the Lee 3D results, the p-value is much smaller in the Lee 2D results. This would suggest that the two dimensional analysis is more significantly bimodal than the three dimensional analysis.

In addition to deviations that are statistically significant, it should be noted that Group B shows marginal significance with four other statistical tests (B_2, DIP, U and W). Each of these are one dimensional examinations of the radial velocity data, only. The statistical sensitivities are presented here:

- **DIP Test** – As stated in the previous section, the DIP test is an analysis of the departure from unimodality. Significance of this test is that the distribution has more than one mode or peak to the distribution. Group B does have a bimodal appearance in velocity space, suggesting that it may have additional substructure and deviation from relaxed conditions.

- **B_2 Test** – Simply stated, this is a test of Kurtosis that examines the flatness or

pointedness of the distribution. For this statistic, a value of 3.000 is normal. A value lower than this is a platykurtic distribution which would appear more like a top hat; whereas a value greater than 3.000 is a leptokurtic distribution which would appear more like the Eiffel Tower, according to Muratov & Gnedin (2010). Group B shows a slightly platykurtic distribution, which is consistent with additional substructure and deviation from relaxed conditions.

- **W Test** – Also known as the Shapiro-Wilk's Test, this test is sensitive to asymmetry, as well as a long tail or shortened tail distribution. Just like the U Test that was mentioned previously, the 3σ-clipping routine may be responsible for a potential false-positive.

- **U Test** – As mentioned previously, the U Test is particularly sensitive to abrupt distribution cutoffs in either distribution tail. Statistical significance here may be due to the cutoff caused by the 3σ-clipping routine, resulting in a potential false-positive.

The overall distribution (following the classical 3-σ clipping routine) is shown in Figure 4.9. In this image, Groups A and B are shown as green and blue respectively with a characteristic Gaussian drawn in, according to their values in Table 4.3 as well as Equation 2.16. The bimodal appearance is still very prominent in Group B. These histograms are expanded for clarity in Figure 4.10.

Another way of visualizing significant deviations in velocity space is by using a Dressler-Shectman bubble plot (Dressler & Shectman, 1988). This plot is based on the Δ test that is described with Equations 4.6 and 4.7. The plot for the distribution of galaxies (following the classical 3-σ clipping routine) in Abell 154 is shown in Figure 4.11. The bubble radius depends on the value of the δ_i statistic in Equation 4.7. A set of large bubbles in an area indicates a group that is either separated at that location by a large radial velocity difference, separated by a large difference in standard deviation, or both. In Figure 4.11, the foreground group (Group A) is clearly visible as the larger bubbles just left of center

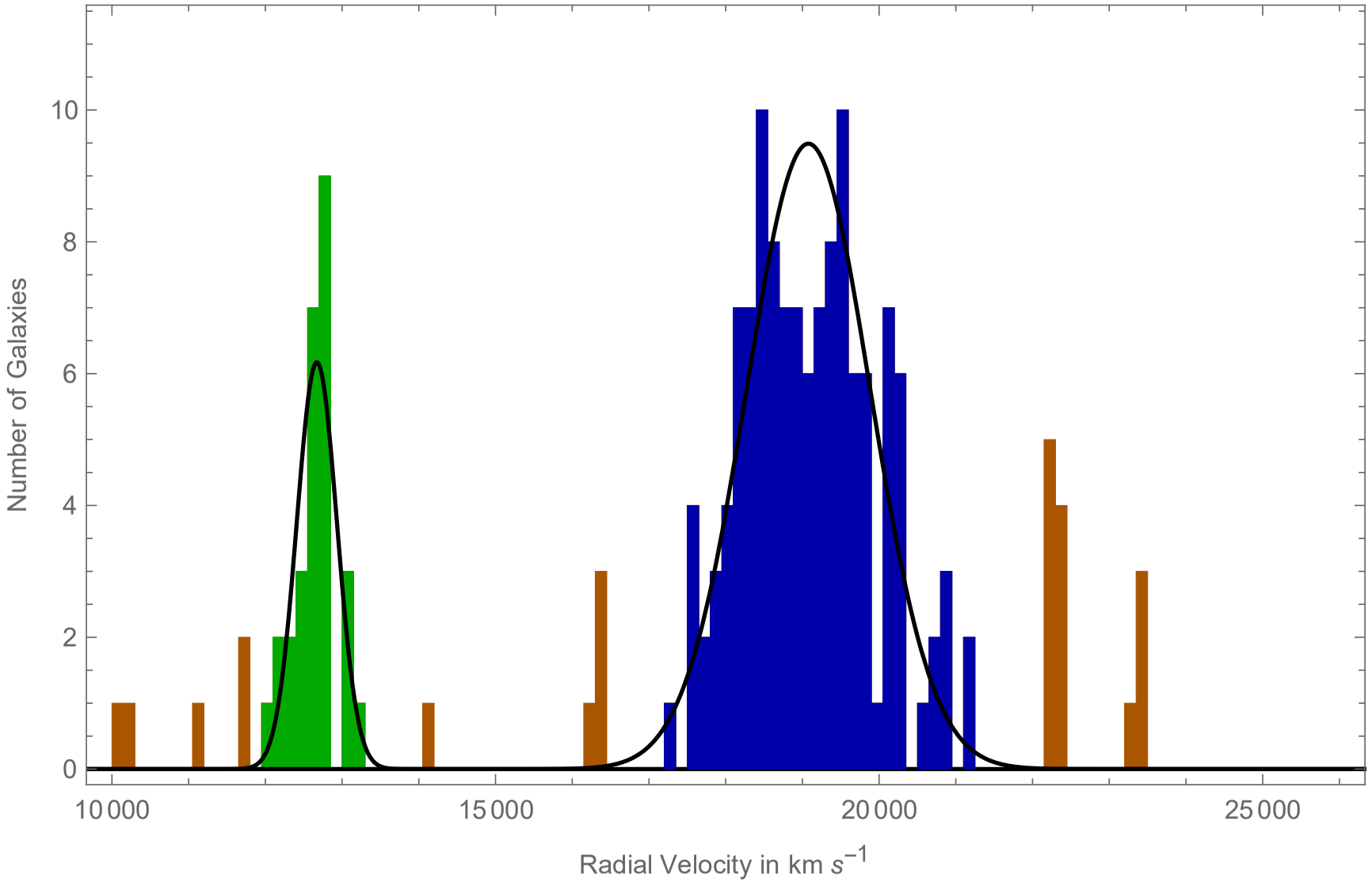

Figure 4.9: Abell 154 radial velocity histogram by group. The galaxies represented in blue and green survived the initial 3-σ clipping routine. Orange represents galaxies that did not survive the final 3-σ clipping routine of either of the two largest groups. They may or may not be group members. The Gaussian curves, shown in black, were estimated by both the Gaussian Mixture Model and KMM results.

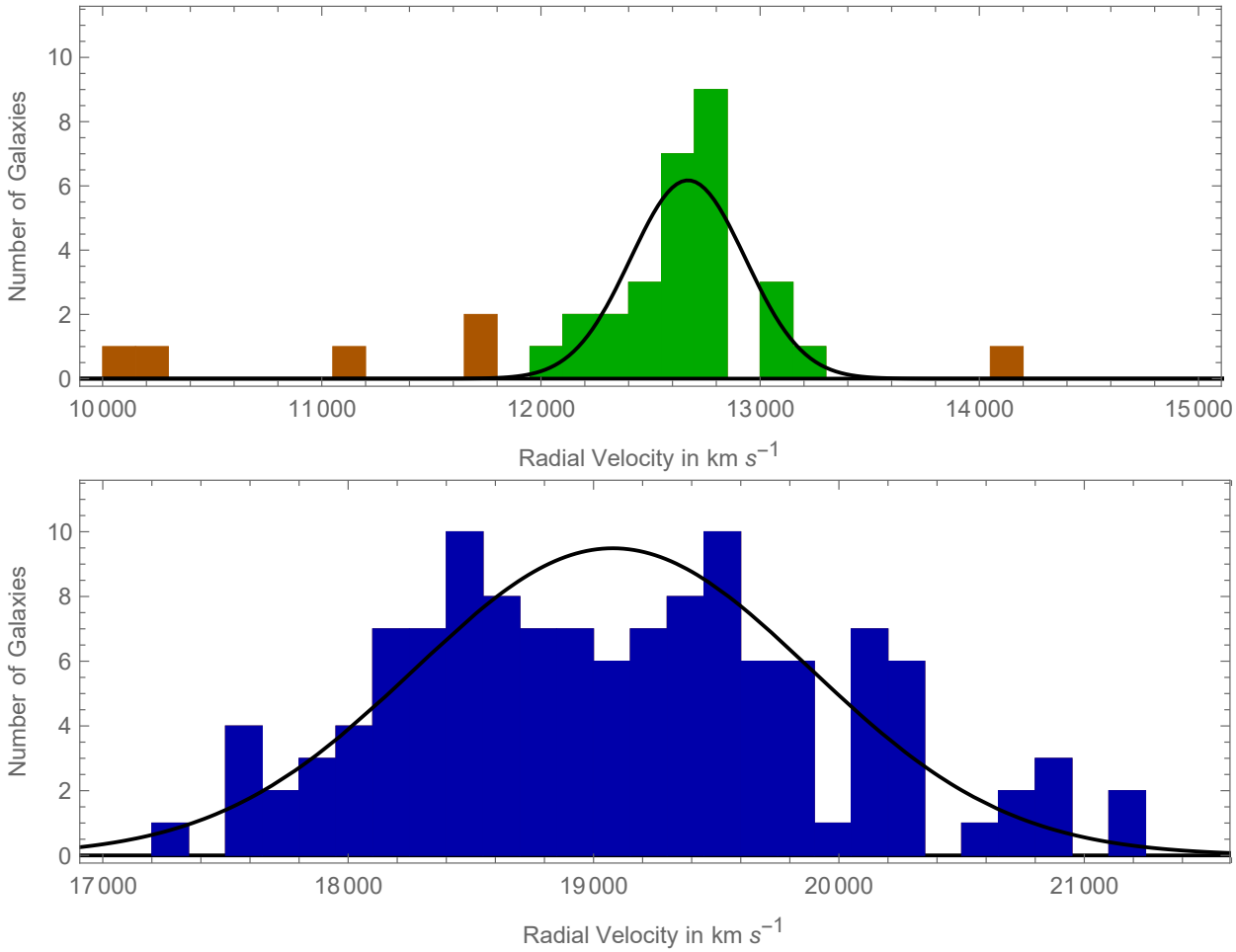

Figure 4.10: Group A and Group B histograms. The top histogram has velocities that range from 10000 km s^{-1} to 15000 km s^{-1}. The bottom histogram has velocities that range from 17000 km s^{-1} to 22000 km s^{-1}. A black single-Gaussian curve is shown. Green and blue colors represent Groups A and B, respectively, as defined in Table 4.3. The orange represents galaxies that did not survive the final 3-σ clipping routine.

while the majority of the other bubbles represents radial velocities that are much closer in magnitude to the main group (Group B), which is seen as a concentration of small bubbles at the top center of the plot.

Dressler-Shectman bubble plot (Dressler & Shectman, 1988) of Group B galaxies (Figure 4.12) shows a group of large bubbles just northwest of the center of the cluster – which appears to also confirm the substructure observed previously by Kriessler & Beers (1997). However, since these galaxies have little deviation in radial velocity, these large bubbles are most likely due to a significant deviation in local-to-global standard deviations. This means that the velocity dispersion is not consistent throughout the cluster.

In the Group A Dressler-Shectman bubble plot (Dressler & Shectman, 1988), which is presented in Figure 4.13, three galaxies are shown with relatively large bubbles in comparison to the other galaxies. With closer inspection, the middle galaxy differs significantly in radial velocity from the other two, explaining the appearance of the large bubbles. Since the five nearest neighbor galaxies are used to determine local values, a significant deviation of only one or two galaxies significantly impacts the local values. Therefore, due to the small number of galaxies in the foreground group (Group A), nothing more can be derived from the bubble plot.

4.2 Gaussian Fitting and Subgroup Analysis

Group A and Group B have both been identified previously using GMM and KMM algorithms in Section 4.1.1. These same routines will again be used to analyze each group independently to look for further potential substructure. In Section 2.3.1, we defined potential groups by the deviation from relaxed conditions relative to the cluster. Similarly, we now define a subgroup as substructure or deviation from a relaxed condition relative to a group. Again, a p-value less than 0.05 suggests a statistically significant result.

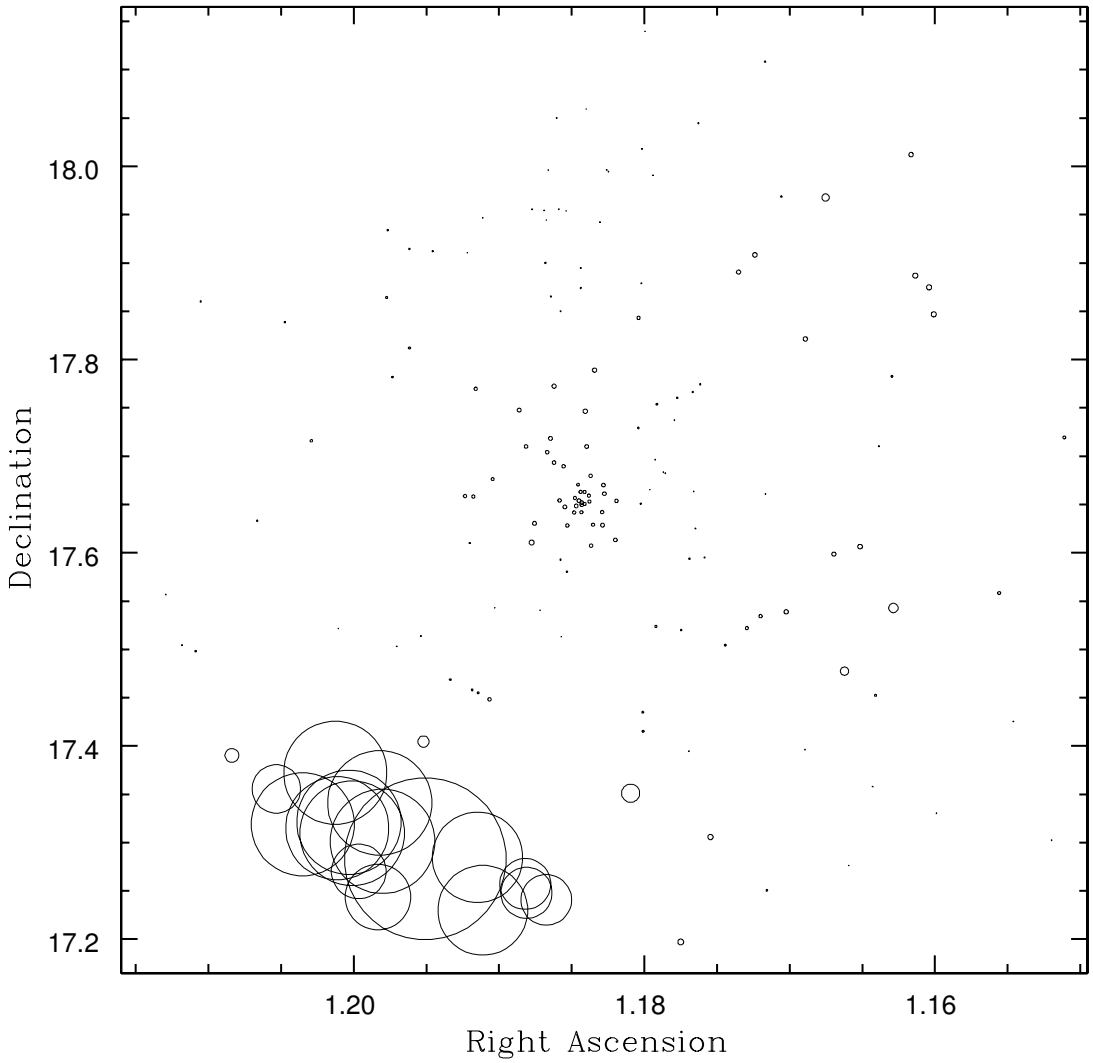

Figure 4.11: 3-σ clipped Dressler-Shectman bubble plot (Dressler & Shectman, 1988). The concentration of large bubbles coincides with the location of the foreground group (Group A), and deviates significantly from the concentration of small bubbles that corresponds to the location of the main group (Group B). This plot suggests strongly that this group is clear substructure that is deviated in velocity or velocity dispersion from the global trend.

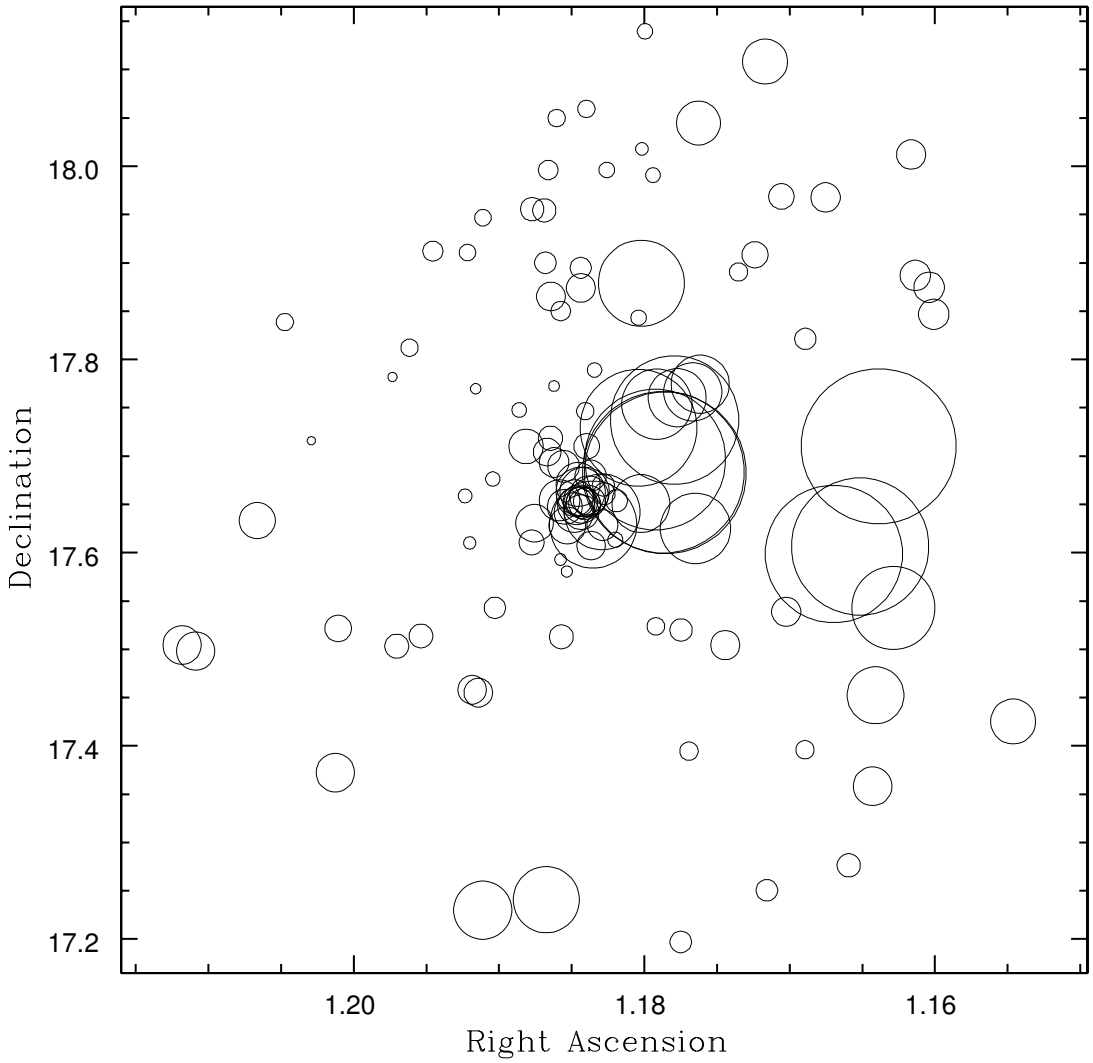

Figure 4.12: Dressler-Shectman bubble plot of Group B galaxies (Dressler & Shectman, 1988). The strong group of large bubbles may indicate that there is unusual deviation in velocity space in that location and should be analyzed closely for potential additional substructure within Group B.

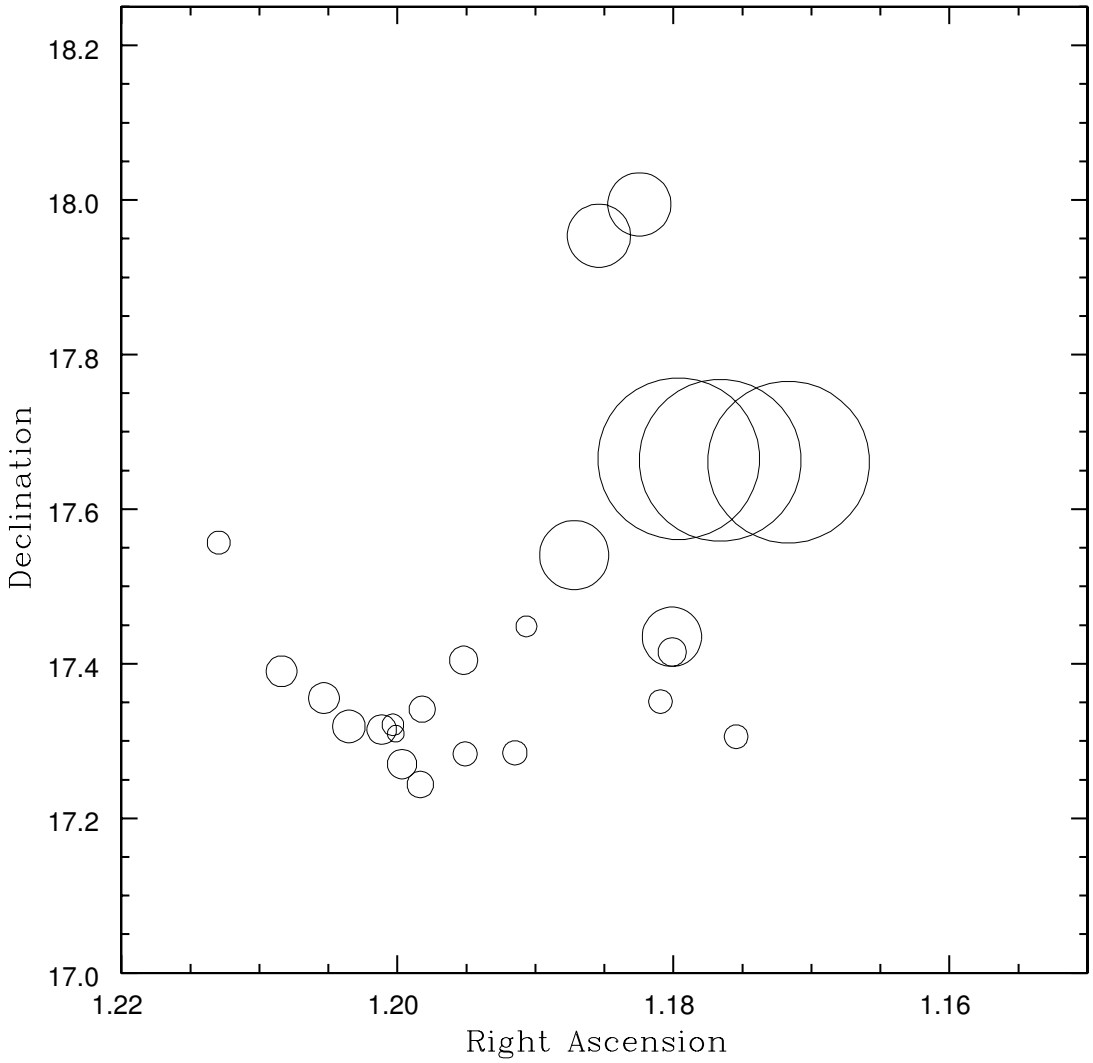

Figure 4.13: Dressler-Shectman bubble plot of Group A galaxies (Dressler & Shectman, 1988). Three galaxies near the center appear more strongly deviated in velocity space than the other galaxies, which appears to be due to a large difference in radial velocity between the middle galaxy from the left and right galaxies.

Source	n	$\bar{v}$	p
KMM 1D	3	12166 km s^{-1}	0.712
	25	12714 km s^{-1}	
GMM	3	12166 km s^{-1}	0.291
	25	12714 km s^{-1}	
KMM 3D	5	12229 km s^{-1}	0.000
	23	12752 km s^{-1}	

Table 4.6: Group A GMM and KMM results. Please note that the KMM 3D is known to have faulty p-values, see Section 4.1.2.

4.2.1 Group A Analysis

The KMM and GMM statistical results for Group A are presented in Table 4.6. GMM and KMM single-dimension algorithms were able to separate the group into the same subgroups, though their p-values are significantly different. Neither p-value indicates statistical significance. Three dimensional KMM algorithm appears to separate into two subgroups also, but the statistical significance of these results is not reliable (Ashman et al., 1994; Muratov & Gnedin, 2010). The extremely small amount of data (28 galaxies) may be the most significant impact and could likely be an impact to any other statistical analyses. A single and a double Gaussian curve has been plotted against the histogram for Group A based on the results of the one-dimensional KMM and GMM algorithms, in Figure 4.14.

4.2.2 Group B Analysis

Initially, by inspection, Group B appears bimodal. However, the appearance may be an artifact of the histogram's bin width. The KMM and GMM algorithms are used to clarify and quantify potential subgrouping. Table 4.7 presents the results of fitting to a two Gaussian distribution. The results clearly show some similarity in values between KMM 1D and GMM, but the number of galaxies and the p-values are significantly different. The p-value for the KMM 3D algorithm is not reliable, but moreover the average velocities do not coincide with the KMM 1D or GMM algorithms, nor with the locations of the modes that appear in the histogram. It is noted that only the KMM 1D places the elliptical galaxies of the core in

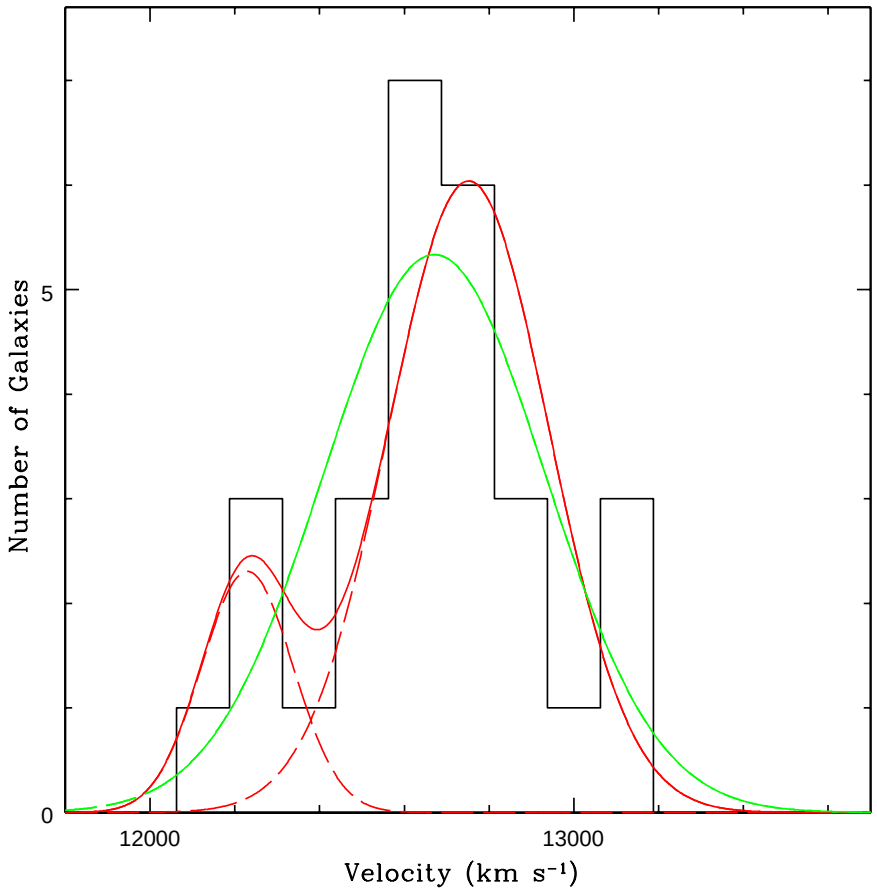

Figure 4.14: Group A histogram. The histogram is shown in black. The green curve represents a single Gaussian curve. TThe red solid curve represents a function composed of two Gaussian curves. The red dashed lines indicate each decomposed individual Gaussian curve. The parameters for these curves were obtained through the KMM routine.

Source	n	$\bar{v}$	p
KMM 1D	59	18485 km s^{-1}	0.110
	66	19666 km s^{-1}	
GMM	43	18350 km s^{-1}	0.232
	82	19505 km s^{-1}	
KMM 3D	36	19210 km s^{-1}	0.000
	89	19070 km s^{-1}	

Table 4.7: Group B, 2 Gaussian GMM and KMM results. Please note that the KMM 3D is known to have faulty p-values, see Section 4.1.2.

separate groups. A wide variety of input parameters were used (varying membership ratios, covariance, and subgroup dispersion predictions), but it consistently resolves these same two-subgroup results as indicated in Table 4.7. Combined with a very low p-value (though ultimately an inconclusive result), this potential subgrouping will be examined further. A plot of the Gaussians from KMM 1D (as well as a single Gaussian) is presented in Figure 4.15

Additionally, the data were fit with a composite function made from three overlapping Gaussians. A wide range of input values were used and resulted in several different results. The results with the lowest p-values are presented in Table 4.8. The GMM algorithm did consistently resolve the same subgroups, but the KMM algorithms were very inconsistent with the change of input parameters. A plot of the Gaussians from GMM (as well as a single Gaussian) is presented in Figure 4.16.

4.2.3 Additional Gaussian Components

In addition to the data presented in the previous section, up to six Gaussian curves on each group were explored. None of these came back with p-value results that were statistically better than the results presented in Tables 4.6, 4.7, and 4.8. For Group B, a Double-Root Residual (DRR) plot is presented and is shown in Figure 4.17. A DRR plot shows graphically the deviation of the empirical distribution function (EDF) from a (theoretical) cumulative distribution function (CDF). A strong match between the EDF and CDF results in almost no deviation and would appear horizontal at DRR = 0. In Figure 4.17, two different plots

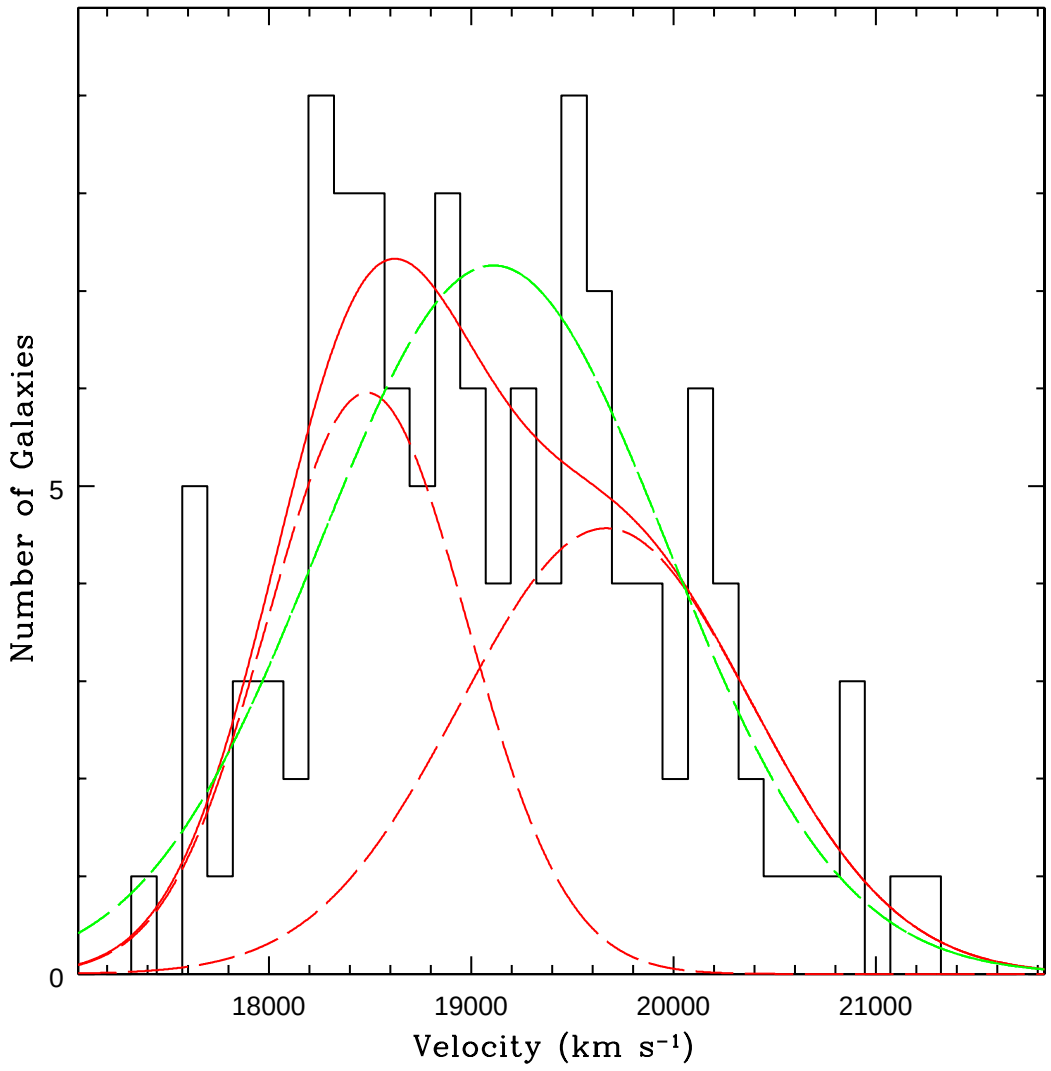

Figure 4.15: Group B histogram. The histogram is in black. A green Gaussian curve is presented. The red solid curve represents a function composed of two Gaussian curves. The red dashed lines indicate each decomposed individual Gaussian curve. The parameters for these curves were obtained through the KMM routine.

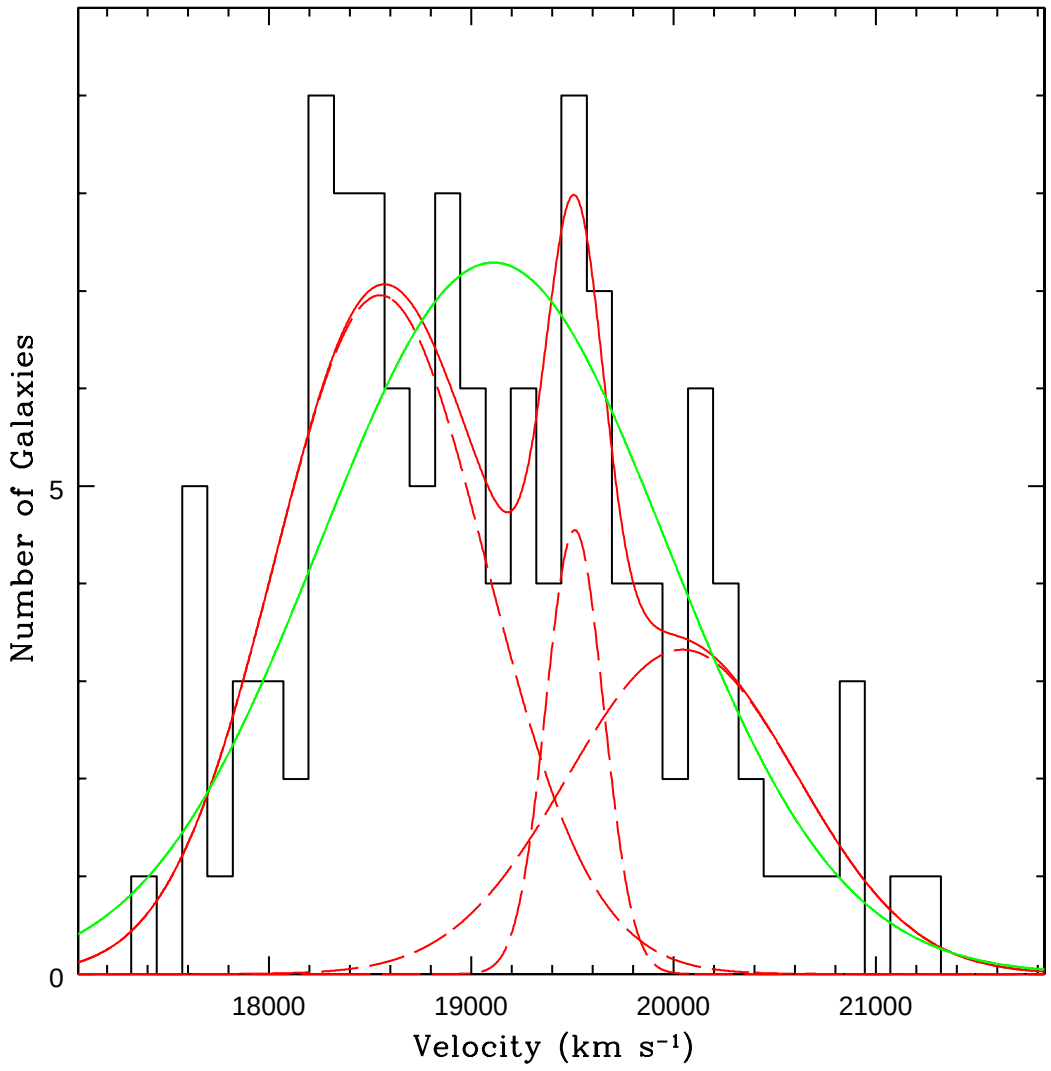

Figure 4.16: Group B histogram. The histogram is shown in black. A green Gaussian curve is presented. The red solid curve represents a function composed of three Gaussian curves. The red dashed lines indicate each decomposed individual Gaussian curve. The parameters for these curves were obtained through the GMM routine.

Source	n	$\bar{v}$	p
KMM 1D	75	18551 km s^{-1}	0.399
	18	19519 km s^{-1}	
	32	20005 km s^{-1}	
KMM 1D	65	18464 km s^{-1}	0.568
	39	19511 km s^{-1}	
	21	20346 km s^{-1}	
GMM	75	18561 km s^{-1}	0.158
	13	19513 km s^{-1}	
	37	20068 km s^{-1}	
KMM 3D	55	18635 km s^{-1}	0.000
	31	19336 km s^{-1}	
	39	19176 km s^{-1}	
KMM 3D	55	18635 km s^{-1}	0.000
	31	19336 km s^{-1}	
	39	19176 km s^{-1}	

Table 4.8: Group B, 3 Gaussian GMM and KMM results. Please note that the KMM 3D is known to have faulty p-values, see Section 4.1.2.

are shown. The green line represents the deviation of the EDF from a CDF, where the CDF is a Gaussian distribution with Group B's average velocity and standard deviation. The red line represents the deviation of the EDF from a CDF where the CDF is a composite function made from two Gaussian distributions based on the values listed for KMM 1D in Table 4.7. The green and red lines in the DRR plot (Figure 4.17) also correspond to the green and red lines shown in Figure 4.15. The green line in Figure 4.17, which corresponds to a single Gaussian fit, appears to deviate more than the composite function, shown in red, made from two overlapping Gaussian curves.

Based on the results of the KMM and GMM algorithms, both groups show the possibility of subgrouping. However, due to the small number of data points, analysis of Group A remains inconclusive. Only Group B exhibits results that are consistent with potential subgrouping and has a significant number of galaxies for analysis. Group B is analyzed further with statistics, but also using the combination of other sources, such as X-ray or Radio data.

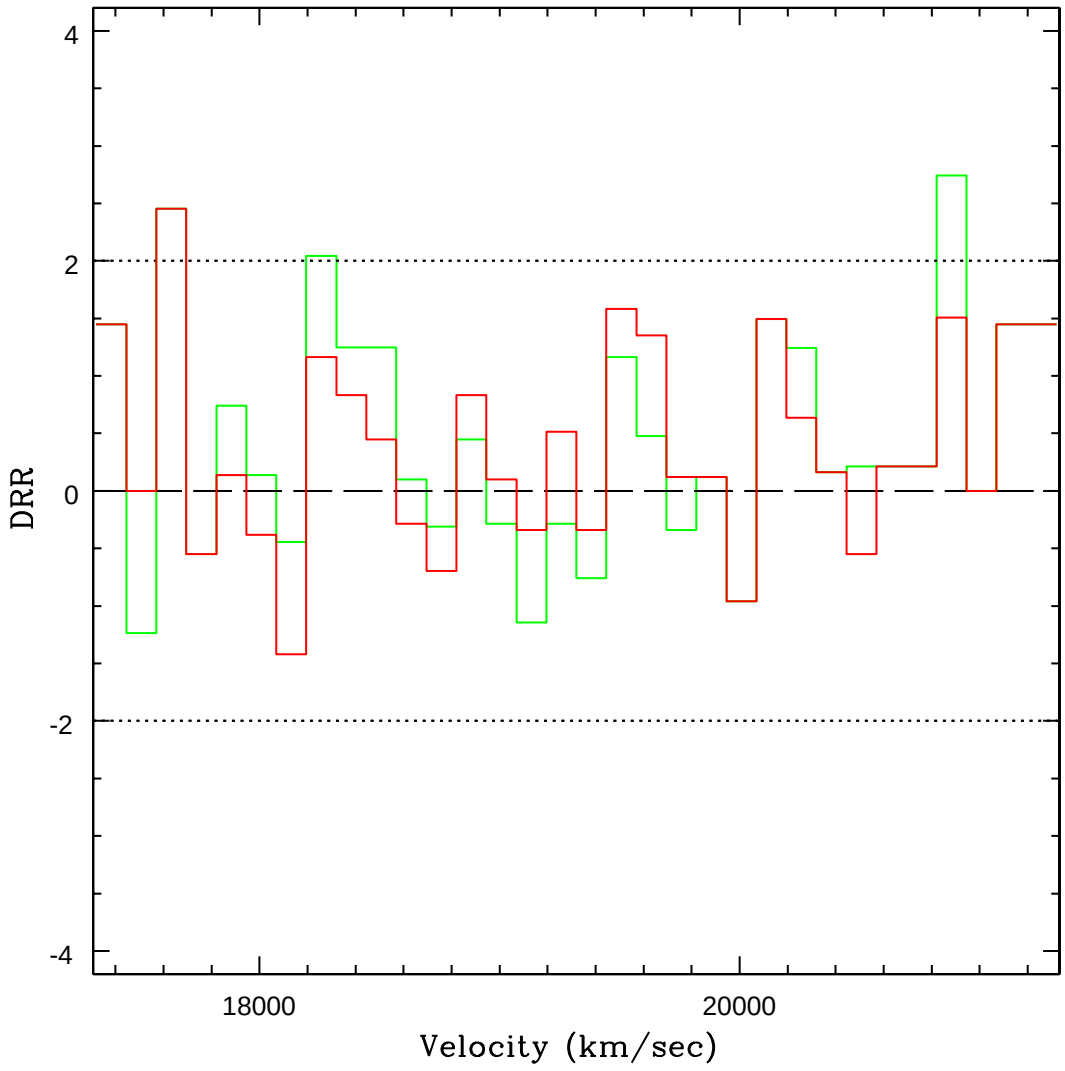

Figure 4.17: Group B double root residual plot. Double-root residual plot of Group B based on the two Gaussian model resolved by KMM in three dimensions. The residual deviation appears slightly stronger in the single Gaussian (green) than in the double Gaussian (red). This would suggest that two Gaussians are a better fit than a single Gaussian.

4.2.4 Subgrouping

Similar to the fact that the cluster could be evaluated for grouping, we can analyze each group for evidence of subgrouping. KMM and GMM are again used to evaluate each group and the likelihood of each group consisting of multiple components or subgroups. The two subgroups that KMM identified (see Table 4.7) were analyzed statistically using the same statistics presented in Table 4.4. The results of those statistical analyses are shown in Table 4.9. Since those subgroups overlap in velocity space, it is not expected that the subgroups will exhibit well-defined Gaussian distributions in radial velocity, nor a clearly symmetric distribution in two- and three-dimensions. Statistics in Table 4.4 are presented only as an analysis for comparison of both subgroups to Group B as a whole.

In nearly all one-dimensional statistics, the subgroups do not reject Gaussian distributions. The p-values of the subgroups are mostly larger than Group B's p-values. Each subgroup appears to exhibit fewer statistics that are marginally significant deviation from a Gaussian distribution as well. Both of these considerations appear to support the subgroup analysis.

4.2.5 Core Structure

cD-type galaxies are generally found at the centers of clusters (Rood & Sastry, 1971; Carter & Metcalfe, 1980; Beers & Geller, 1983; Sarazin, 1986), and so it is expected that the cD galaxies in Abell 154 to be at the center of their respective subgroup. The two large elliptical galaxies have radial velocities of 18213 km s^{-1} and 20258 km s^{-1}. In the KMM 1D identified subgroups, both large elliptical galaxies were sorted into separate groups. The southern elliptical, at 18213 km s^{-1}, appears to be at the projected center of the B1 subgroup, but the radial velocity of the galaxy is less than the average radial velocity of the subgroup, $v = 18485$ km s^{-1}. Likewise, the northern elliptical galaxy, at 20258 km s^{-1}, also appears to be located at the projected center of the B2 subgroup, but the radial velocity is somewhat larger than the average radial velocity of the subgroup, $v =$19668 km s^{-1}.

Statistic	Group B $n = 125$		Subgroup B1 $n = 59$		Subgroup B2 $n = 66$	
	Value	p	Value	p	Value	p
$\bar{x}$	19107	-	18485	-	19668	-
σ	807.2	-	465.2	-	676.2	-
A	0.827	-	0.769	-	0.763	-
A^2	0.481	0.232	0.314	0.454	0.398	0.643
B_1	0.266	0.104	-0.080	0.609	-0.240	0.805
B_2	*2.474*	*0.084*	2.892	0.422	3.225	0.777
B_1B_2	3.486	0.175	*0.115*	*0.056*	1.317	0.482
I	0.944	>0.10	0.985	>0.10	1.026	>0.10
U	*4.517*	*0.05<p<0.10*	4.542	>0.10	4.559	>0.10
U^2	0.069	0.254	0.045	0.468	0.051	0.542
V	0.096	0.314	0.116	0.540	0.096	0.765
W	*0.969*	*0.076*	0.978	0.403	0.970	0.728
W^2	0.077	0.229	0.046	0.426	0.052	0.518
DIP	*0.024*	*0.076*	0.038	0.199	0.034	0.140
Grubbs	2.434	0.861	2.358	0.473	2.433	0.431
K-S	0.065	0.666	0.076	0.114	**0.063**	**0.046**
Fourier	**3.018**	**0.019**	**4.424**	**0.000**	1.442	0.381
Lee 2D	1.565	0.293	**2.368**	**0.044**	1.931	0.241
α	**0.122**	**0.001**	0.104	0.397	**0.133**	**0.036**
Δ	**170.5**	**0.005**	**88.96**	**0.004**	**109.3**	**0.001**
ϵ ($\times 10^{15}$)	2.01	1.000	0.593	0.726	2.124	0.606
Lee 3D	2.245	0.514	2.685	0.919	1.922	0.838

Table 4.9: Subgroup statistics. Statistics for Group B as well as the two potential subgroups B1 and B2. Emboldened figures represent statistically significant deviations from a Gaussian distributions at p<0.05. Italicized figures represent results that are marginally significant. The U test uses Pearson & Stephens (1964) for p-values derived therein.

A possible explanation for the offsets in elliptical galaxy-to-group velocities is that the galaxies may be at or near their closest approach, causing their peculiar velocity components of the radial velocity to be more extreme than their respective groups due to their mutual gravitational influence on each other. If these galaxies are observed just before or just after reaching minimum separation distance, it is expected that: 1.) one galaxy would have developed a much higher radial velocity value as it travels away from us, through the cluster, and 2.) the other galaxy would exhibit a nearly opposite appearance, depending on relative mass, resulting in a radial velocity that has a much lower value as it is traveling toward us, through the cluster. The deviation of elliptical galaxy velocities from their associated

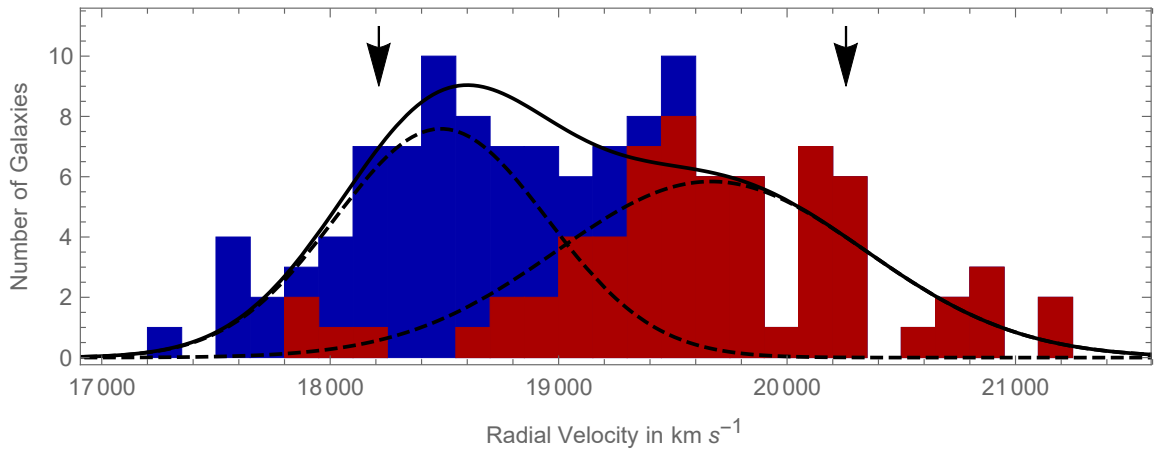

Figure 4.18: Group B histogram with subgroups. Group B galaxies with subgroups indicated by color (blue is Subgroup B1 and red is Subgroup B2). A function that is composed of two Gaussian curves is presented in black, showing the relative size and location of each subgroup. The decomposed Gaussian curves are presented as black dashed lines. The locations of the two cD galaxies is indicated by downward pointing arrows at their respective velocities. The radial velocity uncertainties of the two cD galaxies is smaller than the width of the arrows.

subgroup average velocity appears to be consistent with this point of view, that the cluster is collapsing in a direction that is along the line of sight. The radial velocities of the cD galaxies are shown by downward pointing arrows in Figure 4.18. It should be noted that the widths of the arrows are larger than the elliptical galaxy's radial velocity uncertainty.

Additionally, the difference in radial velocities between the large elliptical galaxies is 2045 km s^{-1}, which is more than twice the velocity dispersion of Group B as a whole (807 km s^{-1}). The most massive galaxies in a relaxed system are not expected to have such large velocities differences after mass segregation has occurred. This would suggest that the cluster core is still undergoing dynamics, which is more consistent with subgroup interaction than a relaxed system.

One notable dissent comes with a closer look of the subgroups. Subgroup B1 appears to be the less massive subgroup and Subgroup B2 appears to be more massive. However, in comparison, the more massive cD galaxy is the southern elliptical which is sorted into Subgroup B1. The less massive cD galaxy was sorted into the more massive subgroup. This information is difficult to reconcile with an expectation that more massive elliptical galaxies tend to be found in more massive clusters (Zhao et al., 2015).

4.2.6 Summary of Statistical Results

Statistical analyses result in a variety of possibilities. With high probability, it is clear that there is a foreground cluster (Group A) that exists primarily south and east of the main cluster. Potential members of this cluster are circled in Figure 4.19. Potential members of the main cluster (Group B), are circled in Figure 4.20. These two groups are examined closely using multi-wavelength data.

The statistics are also consistent with Group B as a cluster that is not fully relaxed. The distribution of velocities appears to be consistent with two groups that are in the process of passing and interacting with each other. A closer look at both subgroups shows that they appear to be elongated in their respective dimensions, see Figure 4.21. See also Figure 4.18 for a histogram that includes the Gaussian distribution curves and locations of cD galaxies.

4.3 Radio Data

As mentioned in Chapter 2, there are no large, diffuse radio structures in the vicinity of Abell 154. There are several compact radio signals that have been located, typically identified as emanating from an active galaxy (Slee et al., 1994; Owen, 1974; Owen & Ledlow, 1997; Feretti & Giovannini, 1994; Owen & Ledlow, 1997; Slee et al., 1996). Most of these detections are around 15 to 30 arc minutes to the north and east of the center of the cluster. In relation to Groups A and B, these emanations do not appear to be directly related to either group, nor do they fall along any boundary between groups or subgroups.

Prior studies have also indicated radio emission that is emanating from the southern elliptical galaxy (Owen & Ledlow, 1997; Feretti & Giovannini, 1994; Guthrie, 1974; Fanti et al., 1983; Slee et al., 1989; Zhao et al., 1989), but this is not unusual for a cD-type galaxy located at the center of a moderately rich cluster (Beers & Geller, 1983; Kormendy & Djorgovski, 1989). The structure of the emission appears to be radio lobes that are found directly east and west of the center of the southern elliptical galaxy (Feretti & Giovannini,

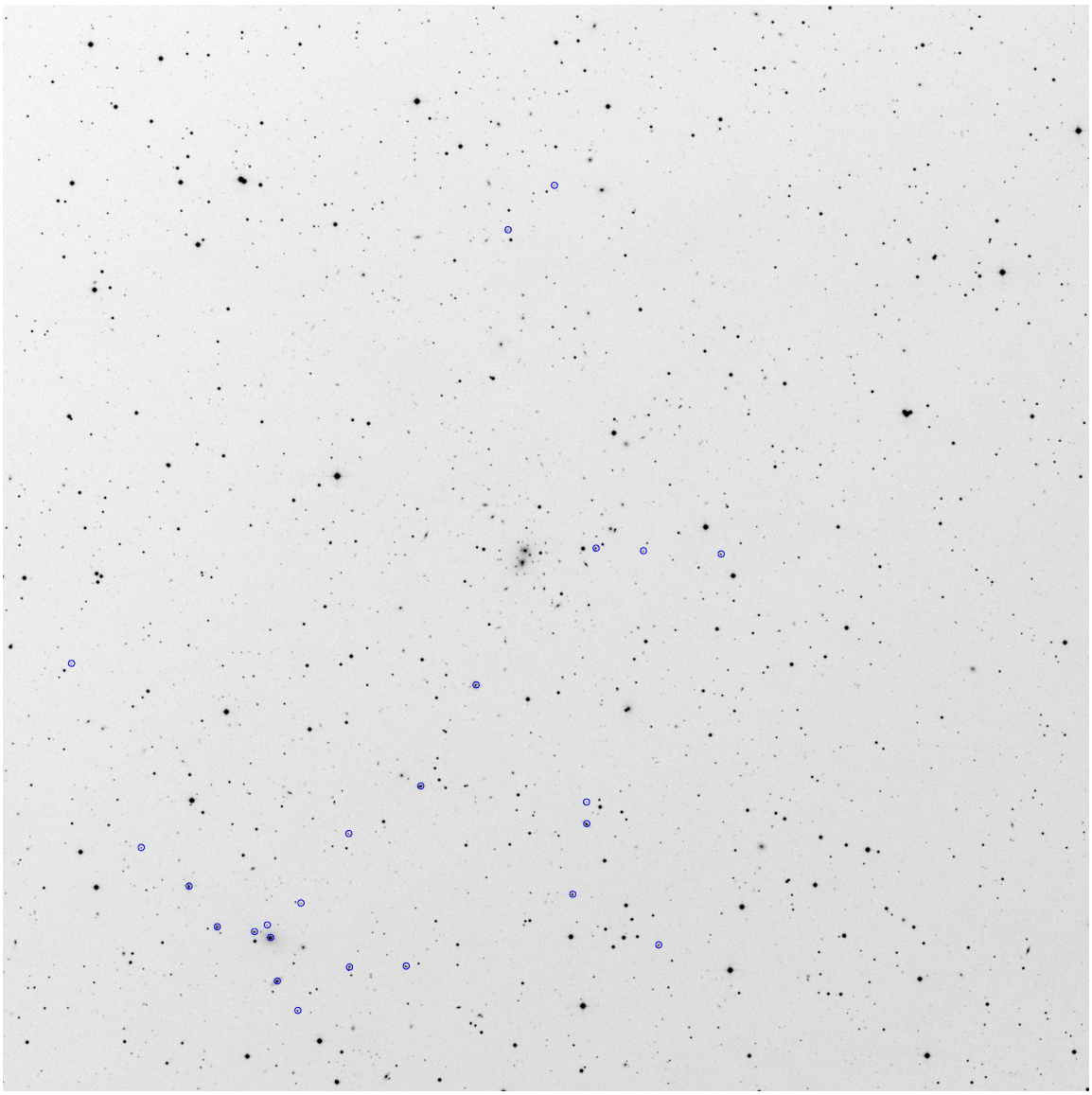

Figure 4.19: Group A map overlay. Group A galaxies are circled in this image, which is overlayed on the Digitized Sky Survey image.

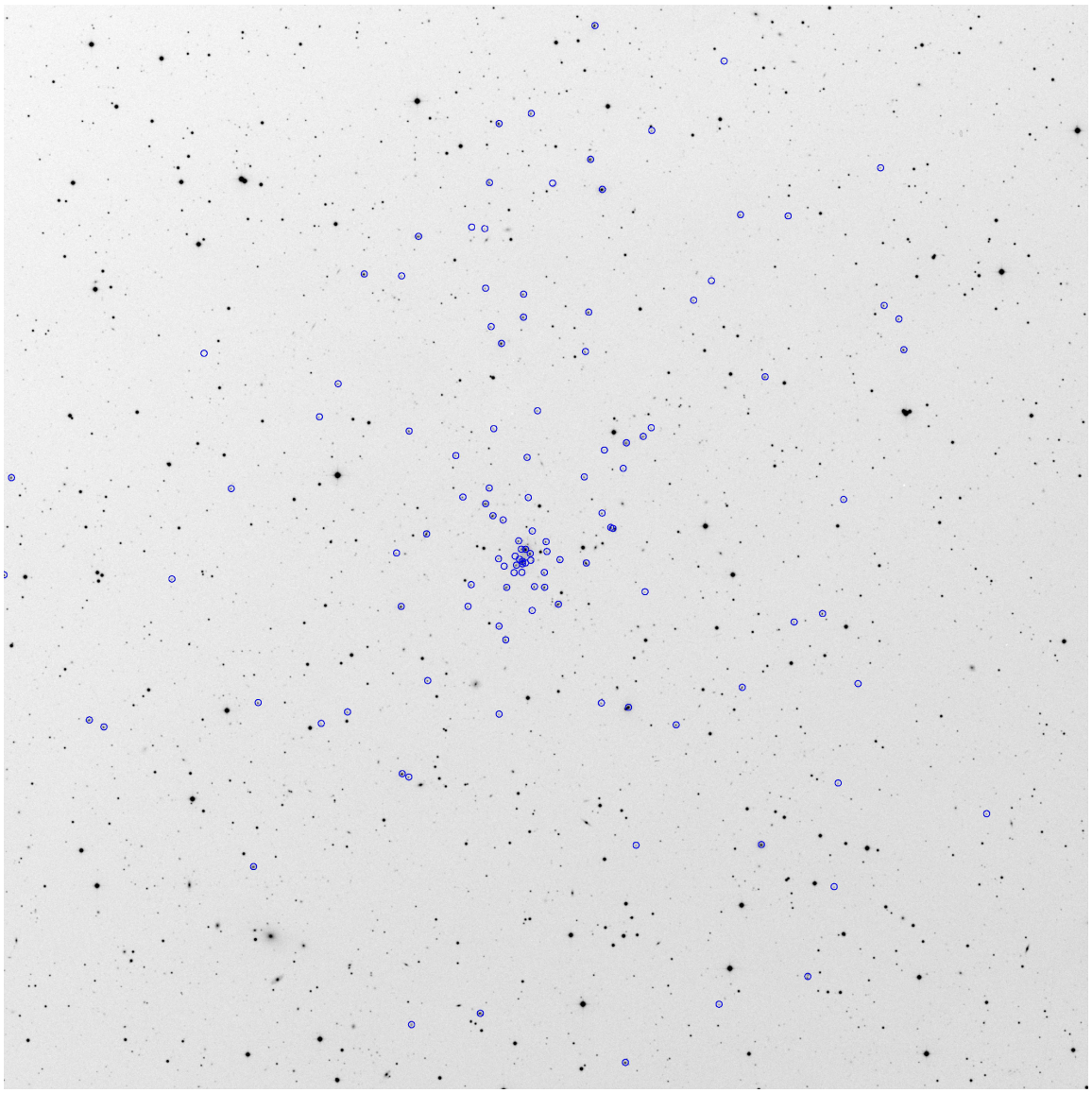

Figure 4.20: Group B map overlay. Group B galaxies are circled in this image, which is overlayed on the Digitized Sky Survey image.

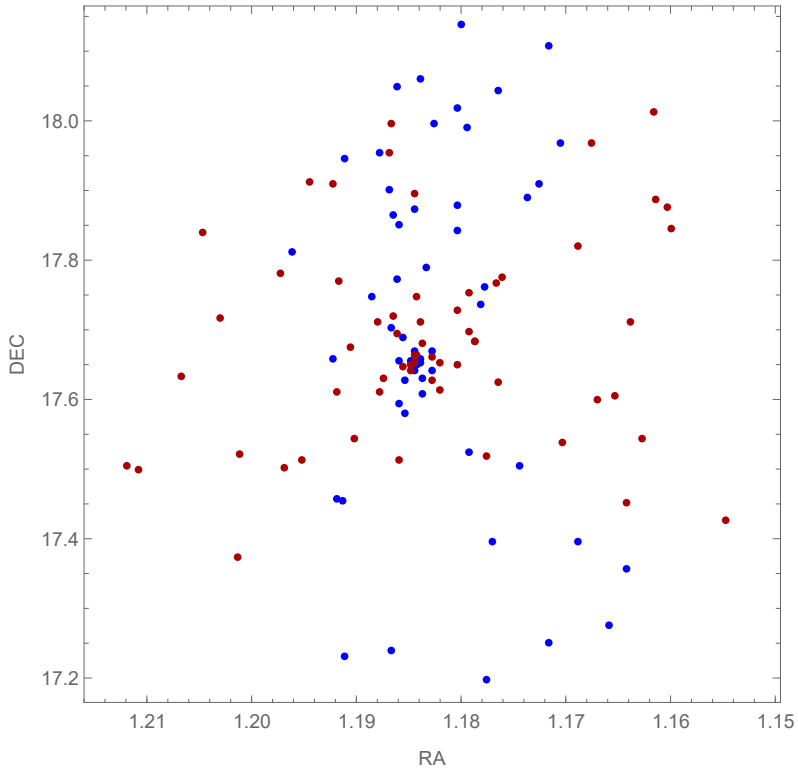

Figure 4.21: Subgroup B1 and Subgroup B2 map. Subgroup B1 is shown in blue. Subgroup B2 is shown in red. Vertical axis is in declination and the horizontal axis is in decimal hours of right ascension.

1994; Owen & Ledlow, 1997).

To summarize, there appears to be no correlation between radio emission features and the cluster velocity structure. This may be due to a weak radio emission that is unable to be detected with current technology. Another possibility is that there may not have been particles capable of being re-accelerated to produce synchrotron radiation, but this seems unlikely due to the radio emission emanating from the southern cD galaxy. Finally, one last possibility is that Group B is actually a single, coherent cluster and that there are no recent, large-scale interactions taking place.

4.4 X-ray Data

As mentioned in Chapter 2, there is a region of X-ray emission that appears relatively symmetric (see Figure 2.8) with enhanced appearance towards the north west side of the

core. The X-ray image from the Einstein Observatory is overlayed on to the DSS image and the brightness was adjusted to enhance clarity in Figure 4.22. ICM gas in Group B is the most likely source of the X-ray emission based on its size, but the peak appears to surround the southern elliptical galaxy.

The northwestern enhancement appears to be a unique feature for Abell 154 and may give reason to believe that the environment is not yet sufficiently relaxed. The enhancement does appear to coincide with the group of large bubbles in the Dressler-Shectman plot for Group B (see Figure 4.12), which may give further cause to believe that some dynamical activity is occurring at that location.

The peak of the X-ray data does appear to coincide with the location of the peak of the radio data, showing that the southern elliptical galaxy resides at the center of the X-ray emission. The X-ray emission traces the gravitational potential well in a cluster with a relaxed ICM, so the location of the X-ray emission peak is consistent with a single coherent cluster.

Figure 4.22 shows an additional peak of emission to the southeast of the main cluster. This coincides with the location of highest concentration of Group A galaxies (see also Figure 4.19 for comparison), and there are a few elliptical galaxies from Group A that reside near, in position, to the X-ray peak. There are also slight fluctuations in X-ray emission towards the northeast and southwest, however those fluctuations are not significant with respect to the image noise.

4.5 Gravitational Binding

Gravitational binding tests were used to determine the potential of the significance of gravitational interactions between groups. Since Group B is significantly larger, the potential of gravitational binding of Group A to the larger Group B is considered. For these tests, two different analyses are used to determine the potential and significance of gravitational

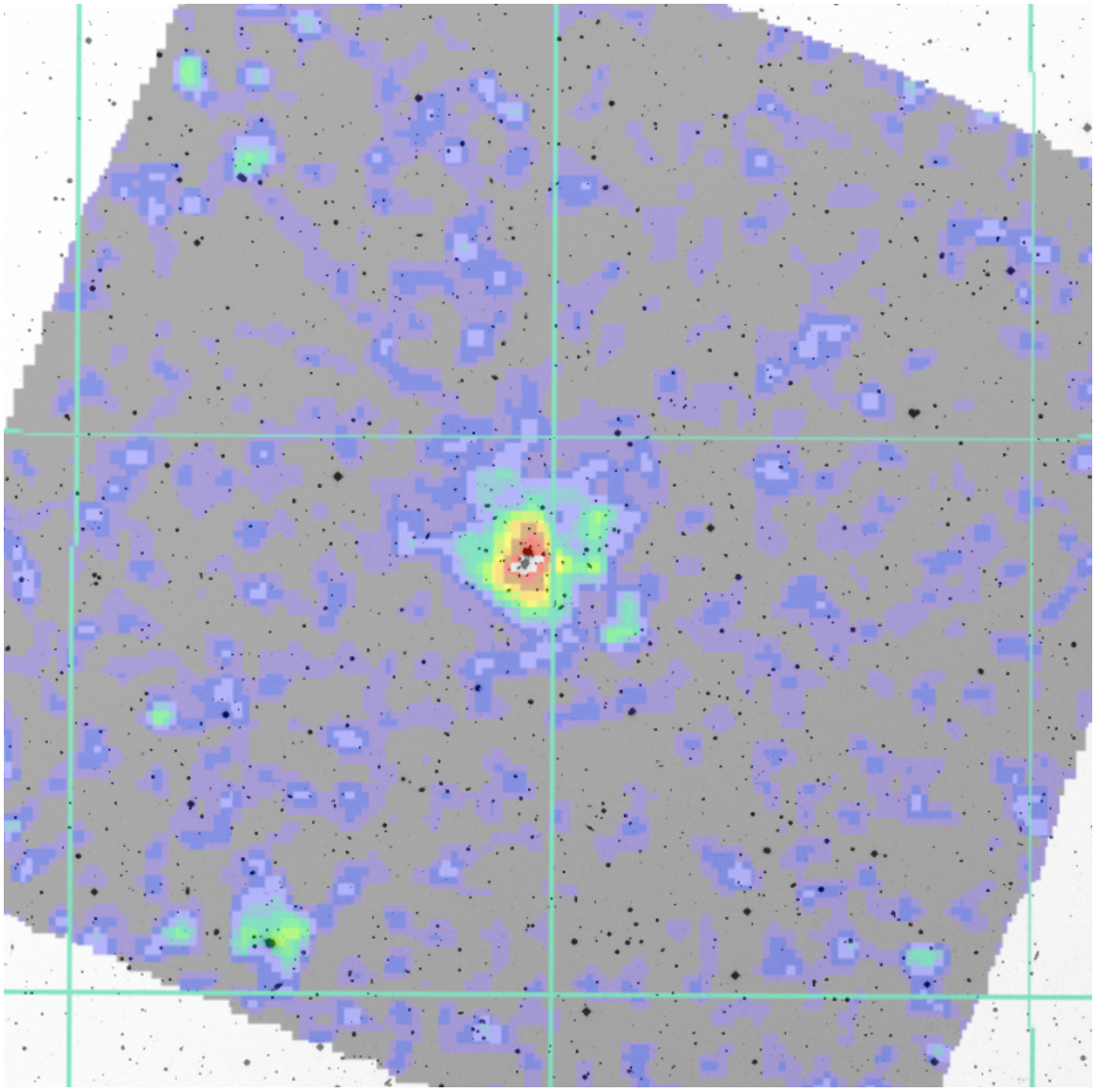

Figure 4.22: X-ray emission in Abell 154. This image is a composite of the DSS image placed in the background with the Einstein X-ray emission in the foreground. The image is the same size and scale as the DSS images used previously (see Figure 2.6 and the backgrounds of Figures 4.19 and 4.20). The X-ray emission peaks over the southern elliptical galaxy and the northwestern enhancement of emission can clearly be seen. Also, X-ray emission peaks again near the southern part of the image. The two peaks correspond to the center of mass of Groups B and A, respectively.

	Virial Mass (M_v)	Projected Mass (M_p)	M_v/M_p
Group A	3.359 x 10^{14}	1.313 x 10^{16}	0.0256
Group B	4.648 x 10^{15}	1.519 x 10^{15}	3.06
B1	1.268 x 10^{15}	7.616 x 10^{14}	1.66
B2	3.032 x 10^{15}	2.017 x 10^{15}	1.50

Table 4.10: Mass estimation. In this table, the results of the projected mass and virial mass estimators are shown. All mass values are in solar masses, or in quantities of 1.99 x 10^{30} kg. The final column indicates the ratio of virial mass (M_v) to projected mass (M_p). A ratio value of two or greater suggests the cluster is not in virial equilibrium.

influence. The first test is a comparison of Projected Mass versus Virial Mass (Heisler et al., 1985). The second method considers gravitational binding in terms of a two-body analysis (Beers et al., 1982).

4.5.1 Projected Mass Versus Virial Mass

This method of analysis uses the Projected Mass estimator and Virial Mass estimator, as described in Heisler et al. (1985) to estimate the mass of the system. If the projected mass estimator is less than half of the virial mass for a Group, it may be evidence that the group is not in virial equilibrium (Berrington et al., 2002), see Table 4.10.

The results presented in Table 4.10 show that only Group B has a projected mass that is less than half the virial mass. The projected mass estimator is highly impacted by angular separation of galaxies and small sample sizes, which may result in an unusually high value for Group A. These results for Group B suggest that it is not relaxed.

If it is assumed that the results of the Projected Mass Estimator for Group A is accurate, then the relationship between Group A and Group B can be concluded. Group A has no evidence beyond sample-size-limited statistical tests of experiencing interactions on a large scale. This would suggest that Group B's dynamical status is not directly related to the gravitational influence of Group A, and would be evidence to suggest that Groups A and B are not gravitationally bound.

4.5.2 Two-Body Analysis

Alternatively, a two-body analysis that compares the group's locations in right ascension, declination and velocity space can also provide an estimate on the likelihood of gravitational binding. This two-body approach (Beers et al., 1982) uses the equation

$$V_r^2 R_P \leq 2\,GM\,sin^2\alpha\,cos\,\alpha, \tag{4.8}$$

where V_r is the radial velocity, R_P is the projected distance between the groups, G is the gravitational constant, M is the total mass of the system and α is the projection angle. The projection angle is the angular difference between a line in space that joins the groups, and the plane of sky (right ascension and declination coordinates). Since the projection angle cannot be determined from this data, the range of all possible projection angles are examined. A zero degree angle would mean that the groups are located in the plane of the sky, whereas a 90 degree angle would mean that the groups are located on top of each other (so that the line connecting the groups is perpendicular to the plane of the sky).

A plot of all possible projection angles is provided for the main group with respect to Group A, see Figure 4.23. In the figure, the shaded region represents the projection angles and line-of-sight velocities that would result in a gravitationally bound condition, whereas the unshaded region represents unbound conditions. The vertical line on the same plot represents the velocity difference between the groups. As you can see in Figure 4.23, Group A is unlikely to be bound to Group B due to the large difference between the galaxy velocities (as represented by the vertical line) and the values that could result in a gravitationally bound condition (as represented by the shaded region).

Additionally, a gravitational binding analysis for Subgroups B1 and B2 was performed. For this test, the gravitational binding of Subgroup B1 is examined, relative to B2, since B2 is the more massive subgroup. Figure 4.24 presents the resulting potential of B1's gravitational binding to the B2 subgroup. In the figure, the majority of possible projection

angles suggest that these subgroups are gravitationally bound conditions, suggesting a strong likelihood that B1 and B2 are gravitationally bound.

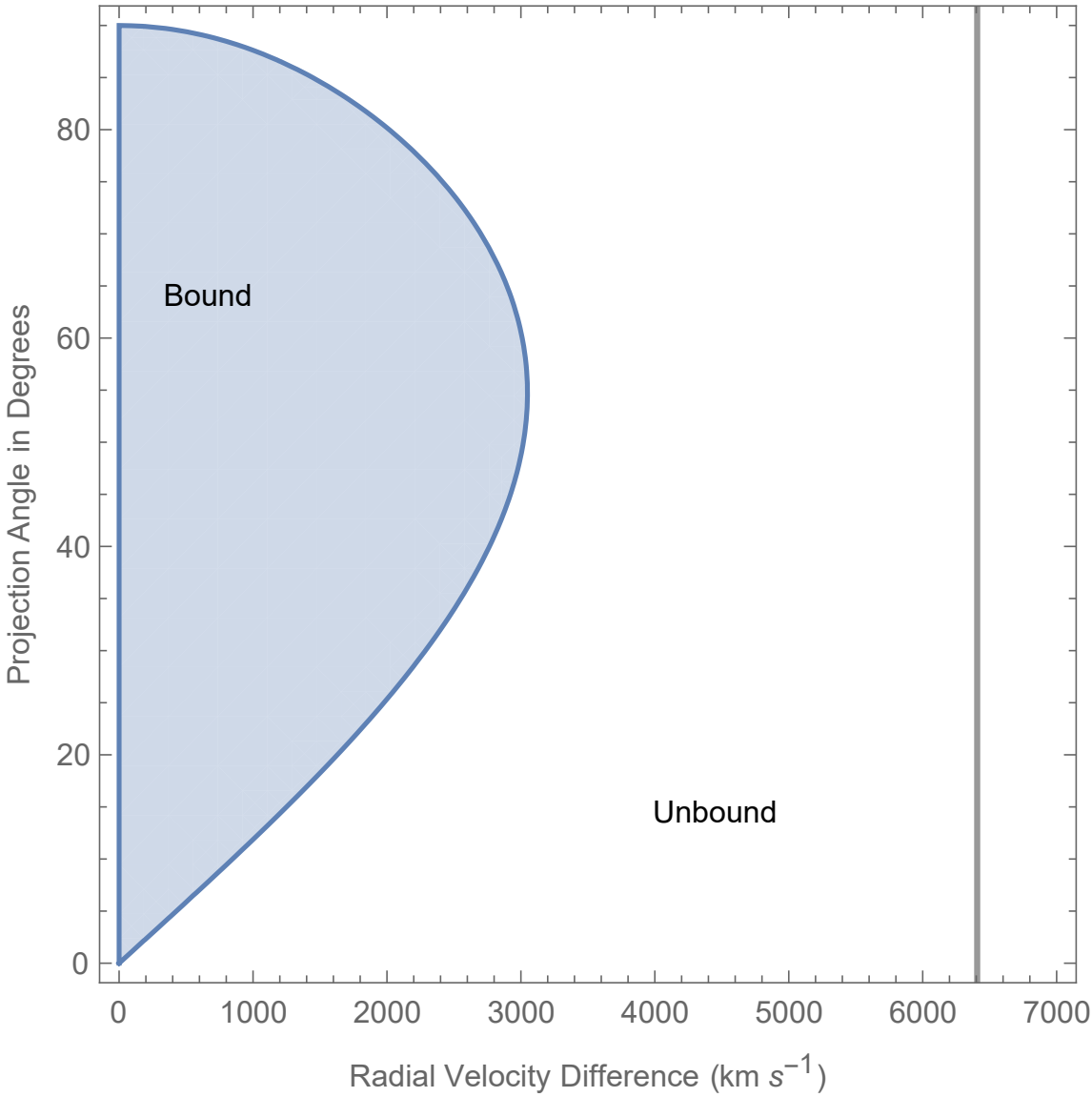

Figure 4.23: Group A to Group B gravitational binding. This diagram shows the potential of Group A being bound to Group B based on the possible radial velocities and projected angles that the groups could have. The shaded region represents the values of velocity and projected angle that would result in a bound condition. Please note that the vertical line represents the actual difference between the group average radial velocities. This plot shows that the groups are not gravitationally bound.

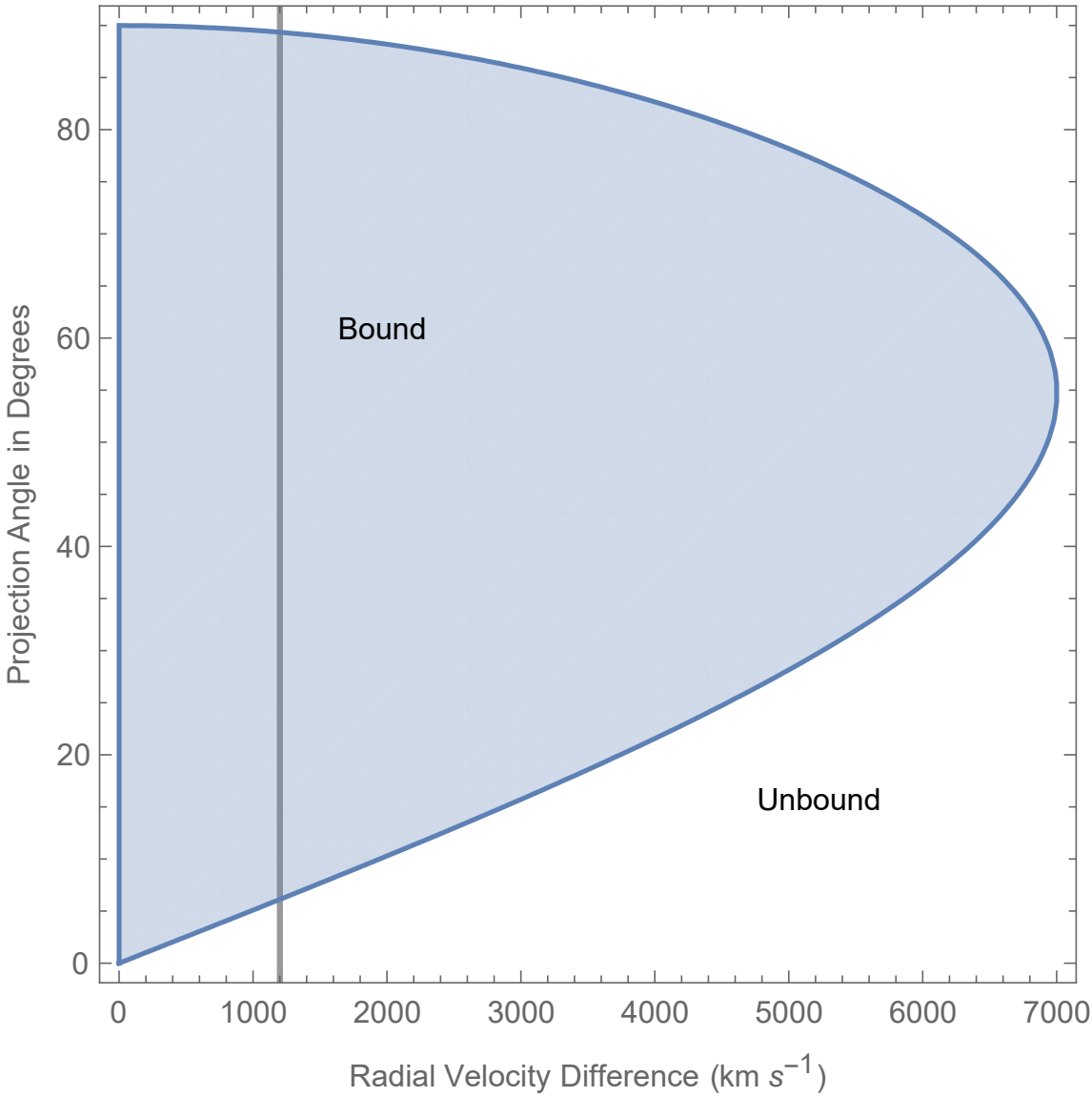

Figure 4.24: Subgroup B1 to Subgroup B2 gravitational binding. This diagram shows the potential of Subgroup B1 being bound to Subgroup B2 based on the possible radial velocities and projected angles that the groups could have. The shaded region represents the values of velocity and projected angle that would result in a bound condition. Please note that the vertical line represents the actual difference between the group average radial velocities. This plot shows that the groups are likely to be gravitationally bound.

Chapter 5

Summary And Conclusions

In the previous chapters, data and analysis of Abell 154 and its substructure has been presented. Abell 154 exhibits a simple problem with complex answers that is fundamental to the subject of galaxy clusters: is it dynamically active, or is it relaxed? The literature provides little evidence to support either position fully, however, there is a consensus that Abell 154 does not exhibit a cooling flow (Jones & Forman, 1984; Stewart et al., 1984; David et al., 1992; White et al., 1997; Loken et al., 1999), and that there is no broad, diffuse radio emission in the area of Abell 154 (Owen & Ledlow, 1997; Slee et al., 1994; Feretti & Giovannini, 1994).

5.1 Summary

Additional radial velocities were collected on Abell 154 in 1997. In total, 219 new radial velocity measurements were obtained for 176 galaxies. The radial velocities of 24 galaxies from the literature were statistically confirmed, and there were 29 other galaxies unique to the literature. In total, 205 galaxies were analyzed, located in an area of about one square degree of the sky, centered on Abell 154's southern large elliptical galaxy.

After analyzing radial velocities and the positions of the galaxies, two clearly distinct groups of galaxies were identified – a small ($n \approx 28$) group of galaxies in the foreground,

Group A, and a large (n $\approx$ 125) group of galaxies, Group B. Potential subgroups were also identified within Group B based on various statistical tests, projected/virial mass estimations and X-ray morphology. It was noted that there was no broad, diffuse radio emission in the area of Group B (Slee et al., 1994; Owen & Ledlow, 1997; Feretti & Giovannini, 1994), which can be found in interacting clusters (Sarazin, 1988).

5.1.1 Group A

Group A was analyzed using 28 galaxies which are located at the foreground in velocity space. The group as a whole is very clearly separated from the largest collection of galaxies in velocity space. Based on position and radial velocity, gravitational binding tests confirm that this group is not gravitationally bound to the larger group, Group B.

Statistical analyses provided some evidence to suggest additional structure. The galaxies in this group visually appear to be richest in number density at a point located at a position angle of 33° east of due south of the southern large elliptical galaxy with an angular separation of about 24 arcminutes, at J2000 right ascension and declination of $1^h11^m57^s$ and $+17°39'13''$. This angular separation corresponds to a projection distance of 1.2 Mpc at Group A's distance, or 1.8 Mpc at Group B's distance, when using the hubble constant of at 74.2 km s^{-1} Mpc^{-1} (Riess et al., 2009). The location of Group A also visually appears to coincide with the position of broad X-ray emission, as can be seen in Figure 4.22.

5.1.2 Group B

Group B, which is the main group of galaxies by radial velocity, was analyzed using 125 galaxies. There were several statistical tests that indicated significant deviation from a relaxed system and several more that were marginally deviated, implying that this group may have additional substructure.

There is no indication, in the literature, of broad, diffuse radio features in the region that could suggest or confirm potential interactions. Radio sources that have been identified

in the region are emanating from specific galaxies and most are well separated in right ascension from the group. The only nearby radio sources appear to be isolated to the regions surrounding the large elliptical galaxies at the core of the group (Slee et al., 1994; Feretti & Giovannini, 1994; Owen & Ledlow, 1997).

From hierarchical merging, it is expected that two merging groups of galaxies will appear as relaxed systems that are superimposed in postion, and/or superimposed in velocity space. The conglomerate will not appear relaxed, but will statistically deviate from relaxed conditions (symmetry in position, gaussian-like radial velocity distribution, etc. as outlined in Section 2.3). It is assumed that the subgroups should deviate less from these relaxed conditions as compared to the collective if interaction is indeed present and recent. The statistical tests confirm that Subgroups B1 and B2 appear to be less deviated from relaxed conditions than the collective Group B due to fewer rejections and marginal rejections of the null hypotheses. See Table 4.9.

X-ray emission is centered on the southern large elliptical galaxy, but extends well beyond the area encompassed by both elliptical galaxies. X-ray emission emanates from the ICM, traces the gravitational potential well of the cluster, and peaks at the center of the ICM. It is also likely to find the most massive galaxy, such as a cD-type galaxy, at the center of mass for a relaxed system (Sarazin, 1986; Kormendy & Djorgovski, 1989; Beers & Geller, 1983). The coincidence of the large elliptical galaxies at the position of the X-ray peak is consistent with a relaxed system. However, it is also consistent with a head-on collision along the line of sight.

The X-ray also exhibits a notable enhancement of emission that extends northward and westward from the core. This asymmetry appears to coincide with the group of relatively larger bubbles in the Dressler-Shectman plot (see Figure 4.12), which suggests that the cluster may deviate from relaxed conditions at that position.

One notable factor is the difference in velocities of the two large elliptical galaxies at the core of the group. While they are located at nearly the same right ascension and

declination and have a visible bridge of luminous material that appears to stretch from one to the other (see Figure 2.7) (Rood & Sastry, 1971; Bautz & Morgan, 1970; Beers & Geller, 1983), the difference in velocity space is nearly 2000 km s^{-1}, a difference that is more than twice as large as Group B's velocity dispersion. Both galaxies are found on either side of Group B in velocity space. These details suggest that their radial velocities are significantly impacted by peculiar velocity.

Additionally, the KMM algorithm sorts each galaxy into separate subgroups, and each galaxy is found at a location in velocity space that is more extreme than their respective subgroups. The characteristics of these dominant galaxies is consistent with the scenario of two subgroups that are in the process of colliding with a relatively small impact parameter.

5.2 Drawing Conclusions

The likely center of the foreground group (Group A) and the main group (Group B) are identified in Table 5.1. These centers are identified as the centroid of the positions of galaxies as well as being confirmed by the presence of a broad X-ray emission that is most likely due to a presence of an ICM. The columns of the table present the group name, number of galaxies, radial velocity average with uncertainty, right ascension and declination. The last column presents the relative location from the southern large elliptical galaxy as a measure of position angle and angular separation. Position angle is measured in degrees, starting due north and moving eastward or counter clockwise on the DSS image.

For Group A, the number of galaxies in the group is too few for any conclusive determination of the dynamical status. The statistical analyses and visually-coincident X-ray emission suggest that it would be beneficial to have a more thorough investigation of the foreground cluster. The group may have an ICM that is the source of the X-ray emission.

Group B appears to have several indications of additional substructure and/or subgroup interactions, based on the positions and radial velocities of galaxies and the asymmetry

	n	$cz \pm \sigma$	R.A.			Dec.			Relative Location	
		(km s^{-1})	h	m	s	$^\circ$	$'$	$''$	PA	Δ
A154 Group A	28	12659 ± 262	1	11	57	+17	19	08	146.39°	23′ 39.9″
A154 Group B	125	19106 ± 807	1	11	03	+17	39	13	303.66°	9.93″

Table 5.1: Group A and Group B characteristics. The centers of the two clearly distinct groups of galaxies as based on the positions of galaxies, radial velocities and the location of the peaks in the X-ray emission. The first column specifies the name of the Group. The second column gives the number of galaxies used to derive the values presented. The third column is the radial velocity with uncertainty. The fourth and fifth columns provide the right ascension and declination of the center points for each group. Finally the last column gives the position angle (measured eastward from due north) and the angular separation of the the group center from the southern large elliptical galaxy.

of the X-ray emission in Abell 154. However, there is a notable lack of broad, diffuse radio emission (Slee et al., 1994; Owen & Ledlow, 1997; Feretti & Giovannini, 1994). One possible explanation is that the radio emission may be too weak to detect, or that the cluster did not reaccelerate enough relativistic ions to produce synchrotron radio emission.

An alternative explanation for the lack of broad radio emission could be that the cluster exhibits a status that is in the late stages of relaxation. Such a condition would require enough time to have passed so that the radio effects of a crossing shock wave would have dissipated, but recent to the initial event so that a cooling flow has not yet formed.

If this alternative explanation is assumed true, the cluster would be exhibiting several false signs of subgroup interactions. The velocity difference between the largest galaxies is a difficult feature to explain. We would also expect some radio emission to remain in the region for some time as a radio halo (Sarazin, 1988), but this is not observed or is too faint to be seen.

Hoffman & Williams (1991) presented that the H I gas in spiral galaxies in Abell 154 was much higher than expected. H I gas is expected (and generally found) to be deficient in clusters, probably due to ram pressure stripping and other mechanisms as a galaxy passes through the ICM (Hoffman & Williams, 1991; Magri et al., 1988). Hoffman & Williams (1991) also found a nearly bimodal appearance in the histogram of H I flux as a function of radial velocity. This seems to confirm the presence of subgroups and seems to suggest that the interaction between subgroups is very young, likely falling through a core for the first

time (Hoffman & Williams, 1991). This information would indicate an interaction time of less than one complete crossing time.

In conclusion, Group B contains two subgroups of galaxies that are in the process of merging. Subgroups B1 and B2 are of relatively similar population and mass, each with a large elliptical galaxy that once dominated each subgroup. The most likely scenario is that the two large elliptical galaxies have probably passed each other with an impact parameter that is small enough to have drawn material into a luminous bridge. Gravitational binding tests and hierarchical merging would suggest that this process is likely to lead to the creation of a single cD galaxy at the center of the cluster.

5.3 Future Work

5.3.1 Current Limitations

Current results for Abell 154 are limited. Statistical results for Group A appear to be limited by the small number of radial velocities in the group. Statistics do indicate potential substructure, but the identification and analysis of any substructure is limited by sampling errors. Additionally, X-ray emission for the group needs to be studied in greater detail to verify that the emission is coming from the Group's ICM.

The X-ray resolution for Group B is also a limitation. The asymmetric appearance of the emission can be used to locate boundaries of interaction. The X-ray emission to the north and west of the main group has a relatively low signal-to-noise, but appears to coincide with local-to-global average velocity and dispersion differences. The X-ray information is ultimately limited by the resolution of the Einstein X-ray Observatory. Improved signal-to-noise emission can help clarify the cause of the asymmetry and verify its connection to the perceived substructure.

Also, current data only cover a range in energies from 0.2 keV to 3.5 keV. Data from a larger range of the X-ray spectrum could be useful in determining the size and location

of the intracluster medium of both Group A and Group B. Higher resolution may provide a glimpse of a bimodal distribution in Group B. For both reasons, more X-ray data is needed. Current telescopes, such as the XMM-Newton or the X-ray Telescope on Swift could image in the same range as the Einstein X-ray Observatory, only with higher resolution. However, more appropriate X-ray observatories include Chandra and the Suzaku X-ray Satellite. The former has been used before to explore the X-ray emission from clusters of galaxies previously and the latter has a broader energy range.

Additionally, cluster/group membership should be analyzed. Current findings may be impacted by interlopers in the field that have similar radial velocities. Furthermore, an analysis of the subgroups B1 and B2 may be beneficial to resolve Group B into a more accurate subset.

This research can also expand into many directions. Obtaining spectra for such a large number of galaxies presents an opportunity to analyze a number of characteristics of the galaxy cluster. Likewise, combining these results with other observational results, such as optical photometry, etc., may improve the analysis into the nature of the cluster as a whole. The following subsections describe multiple ways to advance understanding of this cluster and galaxy clusters in general.

5.3.2 X-ray Emission and the Sunyaev-Zel'dovich Effect

An analysis of X-ray emission and cosmic microwave background temperatures, based on the Sunyaev-Zel'dovich effect, can provide more precise information about the distance and mass of the cluster. The NASA/ESA Planck mission is currently analyzing the Sunyaev-Zel'dovich effect with respect to galaxy clusters. Additionally, past data from the Wilkinson Microwave Anistropy Probe and the ROSAT X-ray satellite may also be useful. This information would clarify group and subgroup membership more precisely, which may provide constraints on the potential dynamical history of the cluster. X-ray emission can also provide some additional information towards clarifying the mechanism and processes that result in developing a

cooling flow.

5.3.3 Metallicity and Stellar Population Analyses

With spectral data, there is an opportunity to examine the relative metallicity content of the galaxies that were observed. More than 100 galaxies appear to have strong absorption features. The environment of the galaxy cluster effects the environment of the galaxies (Beers & Geller, 1983). The dust and gas content and star formation rates within those galaxies may be impacted by the interaction that is taking place. An analysis of this metallicity can also present a better understanding of the evolutional history of the cluster based on the gas and dust content that still remains in the galaxies.

Additionally, the binary core of Abell 154 has not been studied previously with spectral resolution at the level that was obtained. A closer examination of the binary core morphology may clarify how it fits within the evolutionary models of galaxy clusters. Radial velocity dispersion for the the cD galaxies or the bridge of luminous material may also provide additional information about the merging processes that are taking place at the core of a large cluster.

Emission spectra of galaxies indicates the presence gas and dust in the galaxy. Hoffman & Williams (1991) suggests that H I depletion occurs due to ram-pressure stripping of gas and dust as a galaxy passes through the core of a cluster. In Abell 154, examining where emission galaxies are located relative to the cluster may help to refine knowledge and understanding of cluster dynamics and may help to identify galaxies that have and have not passed through the core by the present epoch.

5.3.4 Computational/Numerical Modeling

Finally, it is important to connect the current data with modeling. A theory that properly explains the dynamical status and condition of the cluster must also be in agreement with the possible dynamical histories of the cluster. A comparison of the current observed data

to widely accepted numerical models can provide insights into the way the cluster formed or what requirements may exist in order to support the cluster exhibiting the current observational characteristics. This will help refine the current theories on the large-scale evolution of galaxy clusters, and ultimately, the large-scale filamentary structure of the universe as a whole.

Appendix

In this appendix, radial velocities are presented for dissemination. All values obtained from the literature are summarized in Section A.1. New galactic radial velocities from the 1997 WIYN Hydra observations are presented in Section A.2. A final catalog that contains all radial velocities for the galaxies that are along the line of sight to Abell 154 is presented in Section A.3. Likelihood of membership from the KMM algorithm is also presented. Finally, in the last section, Section A.4, the stellar radial velocities and 1-σ uncertainties are presented. Additional details are provided within those sections.

A.1 Literature Summary

Table A.1 is the summary catalog of radial velocity data that includes all 82 radial velocity measurements obtained from the literature. Column (1) is the ID value that is assigned to each galaxy. The identification values are assigned sequentially and in the order of the references listed in Table 3.4. The first digit is a letter that corresponds to the specific reference, according to the identifications given in Table 3.4. The last two digits are sequentially numbered from 01 to 82. Columns (2) and (3) presents the source's published radial velocity and uncertainty, respectively. Columns (4) - (6) and (7) - (9) present the right ascension and declination for each galaxy in the J2000 epoch. Please note that most data results were precessed from published values since they were published using the B1950 epoch.

Table A.1: Literature radial velocities. Column (1) represents the unique identifier assigned to each galaxy for the purpose of this study. Columns (2) and (3) are the heliocentric radial velocity and uncertainty, respectively. Columns (4)-(6) and (7)-(9) are the right ascension and declination of each galaxy, respectively.

	cz	σ	R.A. (J2000)			Dec. (J2000)		
ID	($km\ s^{-1}$)	($km\ s^{-1}$)	h	m	s	$^\circ$	$'$	$''$
(1)	(2)	(3)	(4)	(5)	(6)	(7)	(8)	(9)
A01	20405	100	1	11	03.8	17	39	47.0
A02	20116	100	1	10	38.9	17	31	12.0
A03	19700	100	1	11	10.37	17	41	36.0
A04	19231	100	1	11	25.57	17	40	34.6
A05	19692	100	1	11	31.25	17	36	36.4
A06	13512	100	1	10	46.65	17	39	55.5
A07	20947	100	1	10	48.86	17	39	03.2
A08	18334	100	1	11	01.74	17	39	33.0
A09	18714	100	1	11	08.73	17	51	00.1
A10	20659	100	1	10	43.31	17	41	00.2
A11	19362	100	1	10	58.37	17	37	43.0
A12	18284	100	1	11	03.43	17	39	07.9
B13	18283	80	1	11	01.74	17	39	33.0
B14	17795	80	1	10	58.46	17	38	31.5
B15	17767	80	1	11	01.6	17	14	11.0
B16	19065	80	1	11	03.6	17	14	31.0
B17	18439	80	1	11	05.2	17	14	24.0
B18	20689	80	1	11	05.4	17	14	30.0
B19	21279	80	1	11	04.88	17	38	54.6
B20	19889	80	1	11	07.7	17	38	51.0
B21	18086	80	1	11	09.0	17	39	15.0
B22	19259	80	1	10	58.37	17	37	43.0
B23	19900	80	1	10	54.91	17	39	13.5
B24	19829	80	1	10	57.91	17	39	40.1
B25	18344	80	1	11	00.71	17	37	44.9
B26	17622	80	1	11	04.43	17	40	14.0
B27	18121	80	1	11	07.09	17	37	41.6
B28	20194	80	1	11	03.43	17	39	07.9
B29	19211	80	1	11	01.31	17	40	46.9
B30	18267	80	1	11	03.8	17	39	47.0
C31	18453	97	1	11	09.73	18	02	59.6
C32	12919	48	1	11	58.77	17	16	12.8
C33	12674	49	1	12	19.17	17	21	20.2
D34	18210	33	1	11	03.43	17	39	07.9
D35	20107	33	1	11	03.8	17	39	47.0
D36	12600	26	1	12	00.41	17	18	34.8
E37	18257	60	1	11	03.43	17	39	07.9

Continued on next page...

Table A.1: Literature radial velocities. Column (1) represents the unique identifier assigned to each galaxy for the purpose of this study. Columns (2) and (3) are the heliocentric radial velocity and uncertainty, respectively. Columns (4)-(6) and (7)-(9) are the right ascension and declination of each galaxy, respectively.

Continued from previous page...

	cz	σ	R.A. (J2000)			Dec. (J2000)		
ID	($km\ s^{-1}$)	($km\ s^{-1}$)	h	m	s	$^\circ$	$'$	$''$
(1)	(2)	(3)	(4)	(5)	(6)	(7)	(8)	(9)
F38	11663	65	1	09	07.1	17	18	09.0
F39	16423	69	1	09	29.7	17	04	58.0
F40	19362	100	1	10	38.9	17	31	12.0
F41	19231	100	1	10	42.8	17	40	57.0
F42	18714	100	1	10	46.65	17	39	55.5
F43	12847	57	1	10	48.31	17	24	55.1
F44	20659	100	1	10	48.86	17	39	03.2
F45	20947	100	1	11	08.73	17	51	00.1
F46	10150	101	1	11	17.5	17	15	26.0
F47	18521	73	1	11	30.67	17	27	29.2
F48	19172	96	1	11	46.9	16	54	35.0
F49	17926	91	1	13	11.3	17	49	53.0
F50	18838	80	1	10	08.2	17	23	45.7
F51	13323	105	1	11	13.89	17	32	25.8
F52	12654	74	1	11	26.36	17	26	54.0
F53	18776	74	1	10	45.86	17	59	26.8
F54	19700	100	1	11	10.37	17	41	36.0
F55	19692	100	1	11	25.57	17	40	34.6
F56	20116	100	1	11	31.25	17	36	36.4
G57	19410	64	1	07	12.87	17	59	37.9
G58	19559	34	1	10	38.5	16	49	34.7
G59	18633	59	1	11	45.24	16	53	10.5
G60	17913	31	1	14	04.47	18	03	40.4
H61	18750	50	1	11	01.31	17	40	46.9
H62	19026	50	1	11	07.21	17	34	49.8
H63	18828	50	1	10	20.21	17	54	25.0
H64	18406	50	1	10	57.3	17	59	46.0
H65	22404	50	1	10	59.0	17	56	32.0
H66	22256	50	1	11	09.2	17	57	20.0
H67	18544	50	1	11	15.8	17	57	20.0
H68	19620	50	1	10	43.31	17	41	00.2
H69	16653	50	1	10	45.86	17	59	26.8
H70	16888	50	1	11	01.31	17	40	46.9
H71	17634	50	1	10	39.86	17	45	37.7
H72	19480	50	1	10	55.18	17	36	47.9
H73	19334	50	1	11	11.8	17	59	45.9

Continued on next page...

Table A.1: Literature radial velocities. Column (1) represents the unique identifier assigned to each galaxy for the purpose of this study. Columns (2) and (3) are the heliocentric radial velocity and uncertainty, respectively. Columns (4)-(6) and (7)-(9) are the right ascension and declination of each galaxy, respectively.

Continued from previous page...

	cz	σ	R.A. (J2000)			Dec. (J2000)		
ID	($km\ s^{-1}$)	($km\ s^{-1}$)	h	m	s	$\circ$	$\prime$	$\prime\prime$
(1)	(2)	(3)	(4)	(5)	(6)	(7)	(8)	(9)
H74	18425	50	1	11	09.73	18	02	59.6
I75	18206	6	1	11	02.8	17	39	02.0
I76	17591	15	1	11	03.5	17	38	59.0
I77	20279	15	1	11	04.2	17	39	14.0
J78	12191	24	1	09	25.94	16	57	37.8
K79	12205	37	1	08	34.6	16	54	00.0
K80	12193	46	1	09	25.94	16	57	37.8
L81	12307	10	1	10	39.0	16	35	51.0
M82	12380	34	1	10	28.9	16	11	25.0

A.2 New Measurements

In this section, new radial velocity measurements are presented in two tables. In Table A.2, radial velocities that were obtained from the absorption features are presented (see Section 3.1 for details). Column (1) is a unique identifier that is made by using the field number as the first digit and the aperture number as the last two digits (See Table 3.1 and Section 3.1.2). Columns (2) and (3) are the heliocentric radial velocity and uncertainty, respectively. Columns (4)-(6) and (7)-(9) are the right ascension and declination of each galaxy, respectively, in the J2000 epoch.

Table A.2: Radial velocities from absorption features. Column (1) represents the unique identifier assigned to each galaxy for the purpose of this study. Columns (2) and (3) are the heliocentric radial velocity and uncertainty, respectively. Columns (4)-(6) and (7)-(9) are the right ascension and declination of each galaxy, respectively.

	cz	σ	R.A. (J2000)			Dec. (J2000)		
ID	($km\ s^{-1}$)	($km\ s^{-1}$)	h	m	s	$\circ$	$\prime$	$\prime\prime$
(1)	(2)	(3)	(4)	(5)	(6)	(7)	(8)	(9)
107	12811.4	22.5	1	11	58.77	17	16	12.8
114	12639.9	33.4	1	12	12.63	17	19	08.3

Continued on next page...

Table A.2: Radial velocities from absorption features. Column (1) represents the unique identifier assigned to each galaxy for the purpose of this study. Columns (2) and (3) are the heliocentric radial velocity and uncertainty, respectively. Columns (4)-(6) and (7)-(9) are the right ascension and declination of each galaxy, respectively.

Continued from previous page...

	cz	σ	R.A. (J2000)			Dec. (J2000)		
ID	($km\ s^{-1}$)	($km\ s^{-1}$)	h	m	s	$^\circ$	$'$	$''$
(1)	(2)	(3)	(4)	(5)	(6)	(7)	(8)	(9)
117	12490.3	37.	1	12	19.17	17	21	20.2
129	20259.2	39.	1	11	02.81	17	39	46.6
145	18808.1	24.5	1	10	08.2	17	23	45.7
154	12587.8	42.	1	12	00.41	17	18	34.8
168	18855.0	33.9	1	10	45.86	17	59	26.8
178	18220.1	40.9	1	11	03.43	17	39	07.9
181	12566.7	29.6	1	11	26.36	17	26	54.
207	14080.6	39.3	1	11	52.87	17	18	05.1
210	18520.1	35.8	1	11	08.73	17	51	00.1
215	12818.8	32.9	1	10	51.38	17	21	04.3
217	13071.8	38.2	1	11	13.89	17	32	25.8
221	20256.4	42.8	1	11	02.81	17	39	46.6
223	18338.9	25.6	1	10	38.99	17	11	49.6
235	18200.9	40.6	1	11	03.43	17	39	07.9
240	18570.0	27.3	1	11	28.02	17	56	48.2
244	18410.8	27.4	1	11	09.73	18	02	59.6
246	19612.1	26.9	1	10	55.18	17	36	47.9
249	19317.2	35.9	1	11	40.42	17	54	43.6
250	22462.7	42.9	1	09	20.09	17	33	30.4
252	12738.8	34.2	1	12	04.08	17	18	53.7
254	18361.7	31.5	1	11	30.67	17	27	29.2
264	20880.0	38.2	1	10	43.31	17	41	00.2
268	19386.3	40.4	1	10	47.85	18	08	22.6
270	13180.5	23.2	1	10	46.65	17	39	55.5
276	17707.9	31.5	1	11	12.08	17	42	14.9
281	12522.6	39.1	1	11	42.31	17	17	00.2
288	19623.4	32.	1	11	31.25	17	36	36.4
294	17605.2	30.8	1	10	39.86	17	45	37.7
295	18854.9	48.9	1	13	02.46	17	38	07.9
296	31819.7	60.7	1	11	41.3	17	13	42.2
299	10036.9	25.7	1	11	17.21	17	14	53.
302	19723.1	50.2	1	11	03.77	17	53	41.6
303	18908.0	54.1	1	11	07.21	17	34	49.8
304	20068.6	48.3	1	10	12.85	17	32	20.
306	22338.3	23.	1	11	12.27	17	56	39.3
307	12633.8	29.5	1	11	54.01	17	14	37.5

Continued on next page...

Table A.2: Radial velocities from absorption features. Column (1) represents the unique identifier assigned to each galaxy for the purpose of this study. Columns (2) and (3) are the heliocentric radial velocity and uncertainty, respectively. Columns (4)-(6) and (7)-(9) are the right ascension and declination of each galaxy, respectively.

Continued from previous page...

	cz	σ	R.A. (J2000)			Dec. (J2000)		
ID	($km\ s^{-1}$)	($km\ s^{-1}$)	h	m	s	$^\circ$	$'$	$''$
(1)	(2)	(3)	(4)	(5)	(6)	(7)	(8)	(9)
309	19181.6	30.4	1	11	25.57	17	40	34.6
310	18344.7	26.5	1	11	02.35	18	03	33.5
312	19388.0	31.9	1	11	11.8	17	59	45.9
313	19551.1	33.	1	12	03.87	17	31	17.8
315	12836.2	29.2	1	10	48.31	17	24	55.1
319	20307.9	25.2	1	10	36.	17	45	59.
320	28811.5	30.9	1	12	48.71	17	43	07.2
321	36164.5	42.	1	12	03.67	17	48	39.1
324	18206.4	25.4	1	11	12.31	17	14	26.9
333	18218.8	29.1	1	12	10.52	17	42	57.3
334	18391.0	25.6	1	11	11.15	17	51	54.8
337	18531.7	25.3	1	10	48.6	18	01	04.7
338	19563.1	46.1	1	09	57.37	17	16	35.1
339	20346.7	27.7	1	09	40.86	17	53	12.9
343	12705.1	19.3	1	10	31.62	17	18	20.9
346	19274.0	31.1	1	10	58.37	17	37	43.
348	19330.3	26.4	1	12	39.19	17	29	53.4
349	19541.3	34.4	1	11	10.37	17	41	36.
352	12650.1	16.2	1	11	42.73	17	24	16.6
353	19303.1	35.1	1	10	34.6	18	02	40.8
357	32234.3	43.3	1	12	42.07	17	54	10.5
363	22211.6	33.1	1	10	36.8	17	35	37.7
367	18946.2	29.6	1	10	08.11	17	49	16.9
369	17892.3	23.3	1	11	07.09	17	37	41.6
370	20856.1	35.3	1	10	48.86	17	39	03.2
371	34169.9	57.4	1	09	47.54	17	49	00.6
372	18526.4	26.4	1	10	58.13	17	40	12.2
374	19424.7	26.3	1	13	01.01	17	43	26.3
379	18877.3	30.3	1	10	27.95	17	30	15.7
381	12527.2	37.1	1	11	42.31	17	17	00.2
384	18579.3	31.1	1	10	40.54	17	44	14.
386	19595.2	24.7	1	11	29.78	17	46	10.9
387	32908.5	33.4	1	11	30.5	17	34	17.1
388	19066.7	25.7	1	12	42.55	17	30	15.7
391	18569.4	33.5	1	10	48.76	17	52	44.5
394	19584.4	30.1	1	09	36.29	17	50	48.5

Continued on next page...

Table A.2: Radial velocities from absorption features. Column (1) represents the unique identifier assigned to each galaxy for the purpose of this study. Columns (2) and (3) are the heliocentric radial velocity and uncertainty, respectively. Columns (4)-(6) and (7)-(9) are the right ascension and declination of each galaxy, respectively.

Continued from previous page...

	cz	σ	R.A. (J2000)			Dec. (J2000)		
ID	($km\ s^{-1}$)	($km\ s^{-1}$)	h	m	s	$^\circ$	$'$	$''$
(1)	(2)	(3)	(4)	(5)	(6)	(7)	(8)	(9)
396	12513.5	34.4	1	11	29.33	17	17	05.4
402	18067.2	73.7	1	11	03.74	17	52	26.4
403	36091.4	77.9	1	12	20.79	17	28	09.2
404	22204.8	48.5	1	10	33.13	17	35	42.6
407	19622.5	46.6	1	11	25.02	17	32	34.3
412	45578.7	70.6	1	11	15.86	17	56	37.
415	17614.0	32.2	1	10	58.46	17	38	31.5
416	12837.2	47.2	1	12	46.59	17	33	24.3
418	18706.9	30.3	1	11	43.35	17	30	49.5
421	17319.9	24.7	1	11	08.02	17	41	22.2
424	32096.0	43.7	1	11	05.21	17	27	40.
425	18221.6	28.1	1	11	01.74	17	39	33.
426	18255.0	25.9	1	11	00.71	17	37	44.9
429	17595.7	24.7	1	11	04.43	17	40	14.
430	18195.3	24.	1	11	12.31	17	14	26.9
434	18671.5	28.4	1	11	31.83	17	54	38.3
437	36000.4	38.6	1	10	48.66	18	01	37.
441	19663.7	32.3	1	09	37.45	17	52	29.
446	22446.5	33.6	1	10	22.6	17	31	19.5
447	18867.8	23.1	1	10	49.43	17	50	35.4
451	18530.7	24.7	1	10	24.66	17	53	26.
453	19595.6	21.4	1	11	02.64	17	44	47.5
454	12066.1	27.9	1	11	53.54	17	20	28.4
456	20341.7	24.8	1	10	49.47	17	43	45.1
460	28764.2	33.3	1	11	10.24	17	26	19.7
462	19046.9	50.2	1	10	36.94	17	23	40.8
466	35903.8	36.2	1	10	08.57	17	22	35.8
469	20180.0	25.9	1	11	15.22	17	37	49.6
471	21198.0	34.1	1	10	45.32	17	41	47.2
473	12669.8	49.3	1	12	30.21	17	23	25.1
474	23460.4	33.9	1	11	30.37	17	39	29.7
478	28709.8	41.3	1	12	48.82	17	39	44.
481	18301.8	28.8	1	11	29.16	17	27	18.5
482	18809.3	32.9	1	10	14.03	17	58	07.1
487	19449.1	24.2	1	11	15.92	17	36	38.5
489	35887.2	46.5	1	10	05.8	17	24	51.5

Continued on next page...

Table A.2: Radial velocities from absorption features. Column (1) represents the unique identifier assigned to each galaxy for the purpose of this study. Columns (2) and (3) are the heliocentric radial velocity and uncertainty, respectively. Columns (4)-(6) and (7)-(9) are the right ascension and declination of each galaxy, respectively.

Continued from previous page...

	cz	σ	R.A. (J2000)			Dec. (J2000)		
ID	($km\ s^{-1}$)	($km\ s^{-1}$)	h	m	s	$^\circ$	$'$	$''$
(1)	(2)	(3)	(4)	(5)	(6)	(7)	(8)	(9)
490	19486.3	25.3	1	09	54.55	17	36	23.
499	18512.7	41.8	1	11	28.04	17	13	48.
504	20189.3	58.7	1	09	16.61	17	25	31.1
508	47769.6	100.3	1	11	32.47	17	57	10.1
509	18422.4	47.4	1	11	32.43	17	39	31.3
510	36045.1	40.5	1	11	08.9	18	08	46.5
512	18185.9	30.2	1	11	12.51	17	54	00.2
524	18779.1	46.	1	11	01.19	17	36	26.6
526	17950.8	47.7	1	10	45.14	17	31	25.6
529	23436.4	43.6	1	12	37.93	17	51	36.5
530	21136.5	26.3	1	11	04.88	17	38	54.6
532	16259.9	35.	1	11	51.89	17	51	51.1
535	19890.7	34.1	1	11	17.31	17	42	36.1
549	45367.9	56.9	1	11	37.06	17	53	17.4
550	19462.9	30.	1	10	01.05	17	35	55.1
552	12569.8	41.9	1	12	01.18	17	19	15.8
553	19063.8	28.3	1	11	01.31	17	40	46.9
554	19624.6	26.6	1	11	25.02	17	32	34.3
555	54303.6	53.4	1	12	21.85	17	24	14.6
556	45197.0	52.9	1	10	27.32	17	48	05.7
557	19264.0	28.6	1	11	50.42	17	46	54.9
559	33810.9	35.2	1	11	19.16	17	48	04.4
561	16317.2	20.2	1	11	46.25	17	54	52.8
567	19740.6	28.7	1	10	57.91	17	39	40.1
568	18598.5	21.4	1	11	00.33	17	47	20.6
569	17997.4	37.8	1	12	23.94	17	37	59.7
572	45134.0	45.8	1	10	38.02	17	47	06.4
585	45489.8	94.9	1	10	38.46	17	27	02.5
590	19774.1	35.	1	10	54.91	17	39	13.5
592	68686.0	100.4	1	11	50.32	18	04	20.6
598	36927.8	48.2	1	10	21.37	17	42	25.8
610	20528.7	40.	1	11	02.29	17	42	36.2
619	35854.7	40.6	1	10	33.35	17	48	06.5
621	20871.8	20.2	1	12	17.06	17	50	19.2
644	20776.0	63.9	1	11	12.81	17	57	15.4
645	51035.6	65.4	1	10	13.19	17	21	31.9

Continued on next page...

Table A.2: Radial velocities from absorption features. Column (1) represents the unique identifier assigned to each galaxy for the purpose of this study. Columns (2) and (3) are the heliocentric radial velocity and uncertainty, respectively. Columns (4)-(6) and (7)-(9) are the right ascension and declination of each galaxy, respectively.

Continued from previous page...

	cz	σ	R.A. (J2000)			Dec. (J2000)		
ID	($km\ s^{-1}$)	($km\ s^{-1}$)	h	m	s	$^\circ$	$'$	$''$
(1)	(2)	(3)	(4)	(5)	(6)	(7)	(8)	(9)
664	52100.8	88.1	1	09	20.69	17	43	15.1
670	19484.4	52.9	1	10	35.33	17	37	30.6
672	20202.3	32.7	1	10	44.9	17	45	13.6
683	18802.5	30.4	1	09	41.9	18	00	43.5
694	35970.1	34.8	1	10	11.7	17	47	31.

Table A.3 consists of radial velocities obtained using emission features (see Section 3.1.3 for details). Column (1) is a unique identifier that is made by using the field number as the first digit and the aperture number as the last two digits. Columns (2) and (3) are the heliocentric radial velocity and uncertainty, respectively. Columns (4)-(6) and (7)-(9) are the right ascension and declination of each galaxy, respectively, in the J2000 epoch. It should be noted that the uncertainties in Table A.3 are relative to the radial velocity of the emission reference spectra that was used, see Table 3.3. The results presented in this table do not account for uncertainty within the reference spectra's VHELIO value, as explained in Section 3.1.3.

Table A.3: Radial velocities from emission spectra. Column (1) represents the unique identifier assigned to each galaxy for the purpose of this study. Columns (2) and (3) are the heliocentric radial velocity and uncertainty, respectively. Columns (4)-(6) and (7)-(9) are the right ascension and declination of each galaxy, respectively. It should be noted that the uncertainties in Table A.3 are relative to the radial velocity of the emission reference spectra that were used and do not account for uncertainty within the reference spectra's VHELIO value, as explained in Section 3.1.3.

	cz	σ	R.A. (J2000)			Dec. (J2000)		
ID	($km\ s^{-1}$)	($km\ s^{-1}$)	h	m	s	$^\circ$	$'$	$''$
(1)	(2)	(3)	(4)	(5)	(6)	(7)	(8)	(9)
107	12788.8	10.5	1	11	58.77	17	16	12.8
218	19058.8	03.6	1	12	04.57	17	22	20.7
240	18569.2	19.8	1	11	28.02	17	56	48.2
246	19605.5	30.4	1	10	55.18	17	36	47.9

Continued on next page...

Table A.3: Radial velocities from emission spectra. Column (1) represents the unique identifier assigned to each galaxy for the purpose of this study. Columns (2) and (3) are the heliocentric radial velocity and uncertainty, respectively. Columns (4)-(6) and (7)-(9) are the right ascension and declination of each galaxy, respectively. It should be noted that the uncertainties in Table A.3 are relative to the radial velocity of the emission reference spectra that were used and do not account for uncertainty within the reference spectra's VHELIO value, as explained in Section 3.1.3.

Continued from previous page...

	cz	σ	R.A. (J2000)			Dec. (J2000)		
ID	($km\ s^{-1}$)	($km\ s^{-1}$)	h	m	s	$\circ$	$\prime$	$\prime\prime$
(1)	(2)	(3)	(4)	(5)	(6)	(7)	(8)	(9)
250	22425.5	04.2	1	09	20.09	17	33	30.4
270	13190.7	05.5	1	10	46.65	17	39	55.5
276	17682.0	08.7	1	11	12.08	17	42	14.9
279	11739.0	03.5	1	09	35.61	17	19	49.4
288	19651.6	07.3	1	11	31.25	17	36	36.4
294	17611.4	16.1	1	10	39.86	17	45	37.7
295	19950.2	15.8	1	13	02.46	17	38	07.9
299	10020.8	08.6	1	11	17.21	17	14	53.
304	20058.6	08.4	1	10	12.85	17	32	20.
310	18360.7	04.4	1	11	02.35	18	03	33.5
312	19374.2	03.7	1	11	11.8	17	59	45.9
317	11187.9	03.6	1	11	36.09	17	28	07.7
319	20301.0	06.3	1	10	36.	17	45	59.
324	18238.2	05.2	1	11	12.31	17	14	26.9
333	18222.4	04.4	1	12	10.52	17	42	57.3
342	13119.7	03.9	1	10	17.98	17	39	39.4
344	12776.4	03.5	1	11	07.43	17	57	13.7
348	19298.6	07.2	1	12	39.19	17	29	53.4
352	12655.0	04.7	1	11	42.73	17	24	16.6
353	19265.2	03.3	1	10	34.6	18	02	40.8
367	18934.7	04.4	1	10	08.11	17	49	16.9
374	19458.2	05.3	1	13	01.01	17	43	26.3
379	18874.8	03.7	1	10	27.95	17	30	15.7
394	19573.7	04.5	1	09	36.29	17	50	48.5
404	22203.6	05.1	1	10	33.13	17	35	42.6
406	20121.6	04.2	1	11	11.27	17	43	06.3
413	18877.8	04.1	1	11	08.77	17	35	34.5
418	18736.7	03.4	1	11	43.35	17	30	49.5
419	19797.9	04.4	1	10	03.09	17	58	03.9
430	18193.0	05.9	1	11	12.31	17	14	26.9
434	18635.9	04.1	1	11	31.83	17	54	38.3
451	18521.2	03.6	1	10	24.66	17	53	26.
454	12061.2	08.6	1	11	53.54	17	20	28.4
460	28686.0	03.4	1	11	10.24	17	26	19.7

Continued on next page...

Table A.3: Radial velocities from emission spectra. Column (1) represents the unique identifier assigned to each galaxy for the purpose of this study. Columns (2) and (3) are the heliocentric radial velocity and uncertainty, respectively. Columns (4)-(6) and (7)-(9) are the right ascension and declination of each galaxy, respectively. It should be noted that the uncertainties in Table A.3 are relative to the radial velocity of the emission reference spectra that were used and do not account for uncertainty within the reference spectra's VHELIO value, as explained in Section 3.1.3.

Continued from previous page...

	cz	σ	R.A. (J2000)			Dec. (J2000)		
ID	$(km\ s^{-1})$	$(km\ s^{-1})$	h	m	s	$\circ$	$\prime$	$\prime\prime$
(1)	(2)	(3)	(4)	(5)	(6)	(7)	(8)	(9)
461	16426.6	03.9	1	11	51.62	17	56	02.1
464	22251.6	03.4	1	09	03.94	17	43	09.9
468	12774.0	04.1	1	10	56.88	17	59	40.
470	12748.2	04.	1	10	35.78	17	39	48.
472	18841.5	03.7	1	10	20.21	17	54	25.
476	18114.9	03.9	1	11	46.19	17	48	43.6
478	28692.7	04.3	1	12	48.82	17	39	44.
491	18289.3	03.9	1	11	10.36	17	46	20.9
496	19831.3	03.8	1	11	08.58	17	30	46.6
498	20022.2	06.5	1	09	49.89	17	42	37.
503	19141.5	04.7	1	11	49.35	17	30	11.5
511	20107.2	03.4	1	09	46.29	17	32	34.3
512	18198.9	04.4	1	11	12.51	17	54	00.2
521	18693.6	03.9	1	11	19.	17	44	51.8
526	17980.3	04.5	1	10	45.14	17	31	25.6
529	23427.0	04.1	1	12	37.93	17	51	36.5
532	16259.0	04.7	1	11	51.89	17	51	51.1
547	19164.5	03.7	1	10	18.07	18	06	29.7
550	19447.4	03.4	1	10	01.05	17	35	55.1
561	16315.7	03.5	1	11	46.25	17	54	52.8
562	18629.6	03.9	1	10	17.65	17	15	02.2
563	19897.3	03.5	1	09	50.71	17	27	08.7
566	28870.2	03.9	1	10	15.12	17	27	06.
569	17987.1	04.4	1	12	23.94	17	37	59.7
577	13012.9	04.	1	10	48.39	17	26	05.8
593	23314.9	04.2	1	09	46.68	17	46	57.7
646	23475.8	03.5	1	10	19.22	17	32	03.9
656	19406.9	03.8	1	10	34.17	17	46	27.8
663	22210.0	03.1	1	09	58.39	17	28	39.
689	18959.4	03.7	1	09	51.46	17	21	29.4

ID in Table A.5	Original Measurement ID	R.A. (J2000)			Dec. (J2000)		
		h	m	s	°	′	″
701	281, 381	1	11	42.31	17	17	00.2
801	407, 554	1	11	25.02	17	32	34.3
802	324, 430	1	11	12.31	17	14	26.85
901	129, 221	1	11	02.81	17	39	46.6
902	178, 235, A12, D34	1	11	03.43	17	39	07.9
JK1	J78, K80	1	09	25.94	16	57	37.8

Table A.4: Cross-listing for duplicate measurements. This table provides a cross-listing of identification numbers for the five galaxies from the new measurements and one galaxy from the literature that had duplicated observations. The first column is the new unique identifier value. The second column indicates the initial identification values that were combined for final results.

A.3 Final Catalog

Table A.5 is the comprehensive catalog of radial velocity data that includes all current values for the 205 galaxies that now have radial velocity measurements. The data include both literature and new measurements with each galaxy represented only once. This incorporates the data in Tables A.1, A.2 and A.3.

In Table A.5, Column (1) is the unique identification value assigned to each galaxy. This identification value is defined in a manner that can be used to trace it directly back to the source of the observations. The number scheme is different for the literature data and the new measurements. For the new data, the first digit represents the field value and the last two digits represent the aperture value within that field. For literature values, the identification values are assigned sequentially and in the order of the references shown in Table 3.4. The first digit, however, is a letter that corresponds to the specific reference as showin in Table 3.4. The last two digits are sequentially numbered from 01 to 82. For measurements of the same galaxy from two different fields or two different literature sources, each has been given different identification numbers. These unique identifiers are presented and cross-listed to their original measurement identifications in Table A.4. The original measurement identifications use the same standard as Column (1) of Table A.5.

Columns (2) and (3) presents the galaxy's radial velocity and uncertainty, respec-

tively. Columns (4)-(6) and (7)-(9) are the right ascension and declination of each galaxy, respectively, in the J2000 epoch. Column (10) provides the source field or the reference from which the data were obtained.

In Table A.6, the KMM fractional likelihood results for assigning galaxies to Subgroups B1 and B2 is presented. The KMM code automatically assigns each galaxy in Group B to either subgroup, but it gives a likelihood based on the chances of being a member of either subgroup. The KMM algorithm only calculates the likelihood of a galaxy to a group, but a galaxy may be an interloper and not a member of either group, so these results may be inaccurate. In Table A.6, Column (1) represents the unique identifier assigned to each galaxy for the purpose of this study. Columns (2) and (3) are the heliocentric radial velocity and uncertainty, respectively. Columns (4)-(6) and (7)-(9) are the right ascension and declination of each galaxy, respectively, in the J2000 epoch. Column (10) and (11) are the fractional likelihood of membership to either Subgroups B1 or B2.

Table A.5: Radial velocities for Abell 154. The table includes all radial velocities, both newly presented here, and also those found in the literature through 2016. Column (1) represents the unique identifier assigned to each galaxy for the purpose of this study. Columns (2) and (3) are the heliocentric radial velocity and uncertainty, respectively. Columns (4)-(6) and (7)-(9) are the right ascension and declination of each galaxy, respectively. Column (10) is the source of the data by field (if it were our observation) and/or citation letter which is based on the identifications given in Table 3.4 (if data from the literature were used).

	cz	σ	R.A. (J2000)			Dec. (J2000)			
ID	($km\ s^{-1}$)	($km\ s^{-1}$)	h	m	s	°	′	″	Source
(1)	(2)	(3)	(4)	(5)	(6)	(7)	(8)	(9)	(10)
G57	19410	64	1	7	12.87	17	59	37.9	G
K79	12205	37	1	8	34.6	16	54	0	K
464	22251.6	17.5	1	9	3.94	17	43	9.9	4
F38	11663	65	1	9	7.1	17	18	9	F
504	20189.3	58.7	1	9	16.61	17	25	31.1	5
250	22430.9	16.4	1	9	20.09	17	33	30.4	2
664	52100.8	88.1	1	9	20.69	17	43	15.1	6
JK1	12191.4	21.3	1	9	25.94	16	57	37.8	J & K
F39	16423	69	1	9	29.7	17	4	58	F
279	11739	17.5	1	9	35.61	17	19	49.4	2
394	19576.5	15.3	1	9	36.29	17	50	48.5	3
441	19663.7	32.3	1	9	37.45	17	52	29	4
339	20346.7	27.7	1	9	40.86	17	53	12.9	3

Continued on next page...

Table A.5: Radial velocities for Abell 154. The table includes all radial velocities, both newly presented here, and also those found in the literature through 2016. Column (1) represents the unique identifier assigned to each galaxy for the purpose of this study. Columns (2) and (3) are the heliocentric radial velocity and uncertainty, respectively. Columns (4)-(6) and (7)-(9) are the right ascension and declination of each galaxy, respectively. Column (10) is the source of the data by field (if it were our observation) and/or citation letter which is based on the identifications given in Table 3.4 (if data from the literature were used).

Continued from previous page...

	cz	σ	R.A. (J2000)			Dec. (J2000)			
ID	($km\ s^{-1}$)	($km\ s^{-1}$)	h	m	s	°	′	″	Source
(1)	(2)	(3)	(4)	(5)	(6)	(7)	(8)	(9)	(10)
683	18802.5	30.4	1	9	41.9	18	0	43.5	6
511	20107.2	17.5	1	9	46.29	17	32	34.3	5
593	23314.9	17.7	1	9	46.68	17	46	57.7	5
371	34169.9	57.4	1	9	47.54	17	49	0.6	3
498	20022.2	18.4	1	9	49.89	17	42	37	4
563	19897.3	17.5	1	9	50.71	17	27	8.7	5
689	18959.4	17.6	1	9	51.46	17	21	29.4	6
490	19486.3	25.3	1	9	54.55	17	36	23	4
338	19563.1	46.1	1	9	57.37	17	16	35.1	3
663	22210	17.5	1	9	58.39	17	28	39	6
550	19451.3	15.1	1	10	1.05	17	35	55.1	5
419	19797.9	17.7	1	10	3.09	17	58	3.9	4
489	35887.2	46.5	1	10	5.8	17	24	51.5	4
367	18937.7	15.2	1	10	8.11	17	49	16.9	3
145	18810.7	23.4	1	10	8.2	17	23	45.7	1 & F
466	35903.8	36.2	1	10	8.57	17	22	35.8	4
694	35970.1	34.8	1	10	11.7	17	47	31	6
304	20060	17.8	1	10	12.85	17	32	20	3
645	51035.6	65.4	1	10	13.19	17	21	31.9	6
482	18809.3	32.9	1	10	14.03	17	58	7.1	4
566	28870.2	17.6	1	10	15.12	17	27	6	5
562	18629.6	17.6	1	10	17.65	17	15	2.2	5
342	13119.7	17.6	1	10	17.98	17	39	39.4	3
547	19164.5	17.6	1	10	18.07	18	6	29.7	5
646	23475.8	17.5	1	10	19.22	17	32	3.9	6
472	18840	16.6	1	10	20.21	17	54	25	4 & H
598	36927.8	48.2	1	10	21.37	17	42	25.8	5
446	22446.5	33.6	1	10	22.6	17	31	19.5	4
451	18524.4	14.3	1	10	24.66	17	53	26	4
556	45197	52.9	1	10	27.32	17	48	5.7	5
379	18875.4	15.2	1	10	27.95	17	30	15.7	3
M82	12380	34	1	10	28.9	16	11	25	M
343	12705.1	19.3	1	10	31.62	17	18	20.9	3
404	22203.7	16.8	1	10	33.13	17	35	42.6	4

Continued on next page...

Table A.5: Radial velocities for Abell 154. The table includes all radial velocities, both newly presented here, and also those found in the literature through 2016. Column (1) represents the unique identifier assigned to each galaxy for the purpose of this study. Columns (2) and (3) are the heliocentric radial velocity and uncertainty, respectively. Columns (4)-(6) and (7)-(9) are the right ascension and declination of each galaxy, respectively. Column (10) is the source of the data by field (if it were our observation) and/or citation letter which is based on the identifications given in Table 3.4 (if data from the literature were used).

Continued from previous page...

	cz	σ	R.A. (J2000)			Dec. (J2000)			
ID	($km\ s^{-1}$)	($km\ s^{-1}$)	h	m	s	°	′	″	Source
(1)	(2)	(3)	(4)	(5)	(6)	(7)	(8)	(9)	(10)
619	35854.7	40.6	1	10	33.35	17	48	6.5	6
656	19406.9	17.6	1	10	34.17	17	46	27.8	6
353	19272.8	15.7	1	10	34.6	18	2	40.8	3
670	19484.4	52.9	1	10	35.33	17	37	30.6	6
470	12748.2	17.7	1	10	35.78	17	39	48	4
319	20303.4	14.8	1	10	36	17	45	59	3
363	22211.6	33.1	1	10	36.8	17	35	37.7	3
462	19046.9	50.2	1	10	36.94	17	23	40.8	4
572	45134	45.8	1	10	38.02	17	47	6.4	5
585	45489.8	94.9	1	10	38.46	17	27	2.5	5
G58	19559	34	1	10	38.5	16	49	34.7	G
A02	20116	100	1	10	38.9	17	31	12	A
223	18338.9	25.6	1	10	38.99	17	11	49.6	2
L81	12307	10	1	10	39	16	35	51	L
294	17612.2	17.5	1	10	39.86	17	45	37.7	2 & H
384	18579.3	31.1	1	10	40.54	17	44	14	3
F41	19231	100	1	10	42.8	17	40	57	F
264	20880	38.2	1	10	43.31	17	41	0.2	2
672	20202.3	32.7	1	10	44.9	17	45	13.6	6
526	17976.7	16.7	1	10	45.14	17	31	25.6	5
471	21198	34.1	1	10	45.32	17	41	47.2	4
168	18841.3	30.8	1	10	45.86	17	59	26.8	1 & F
270	13186.9	14.2	1	10	46.65	17	39	55.5	2
268	19386.3	40.4	1	10	47.85	18	8	22.6	2
315	12838.4	26	1	10	48.31	17	24	55.1	3 & F
577	13012.9	17.6	1	10	48.39	17	26	5.8	5
337	18531.7	25.3	1	10	48.6	18	1	4.7	3
437	36000.4	38.6	1	10	48.66	18	1	37	4
391	18569.4	33.5	1	10	48.76	17	52	44.5	3
370	20866.1	33.3	1	10	48.86	17	39	3.2	3 & A
447	18867.8	23.1	1	10	49.43	17	50	35.4	4
456	20341.7	24.8	1	10	49.47	17	43	45.1	4
215	12818.8	32.9	1	10	51.38	17	21	4.3	2
590	19774.1	35	1	10	54.91	17	39	13.5	5

Continued on next page...

Table A.5: Radial velocities for Abell 154. The table includes all radial velocities, both newly presented here, and also those found in the literature through 2016. Column (1) represents the unique identifier assigned to each galaxy for the purpose of this study. Columns (2) and (3) are the heliocentric radial velocity and uncertainty, respectively. Columns (4)-(6) and (7)-(9) are the right ascension and declination of each galaxy, respectively. Column (10) is the source of the data by field (if it were our observation) and/or citation letter which is based on the identifications given in Table 3.4 (if data from the literature were used).

Continued from previous page...

	cz	σ	R.A. (J2000)			Dec. (J2000)			
ID	($km\ s^{-1}$)	($km\ s^{-1}$)	h	m	s	°	′	″	Source
(1)	(2)	(3)	(4)	(5)	(6)	(7)	(8)	(9)	(10)
246	19609.6	21.3	1	10	55.18	17	36	47.9	2
468	12774	17.7	1	10	56.88	17	59	40	4
H64	18406	50	1	10	57.3	17	59	46	H
567	19740.6	28.7	1	10	57.91	17	39	40.1	5
372	18526.4	26.4	1	10	58.13	17	40	12.2	3
346	19279	27.9	1	10	58.37	17	37	43	3, A & B
415	17614	32.2	1	10	58.46	17	38	31.5	4
H65	22404	50	1	10	59	17	56	32	H
568	18598.5	21.4	1	11	0.33	17	47	20.6	5
426	18255	25.9	1	11	0.71	17	37	44.9	4
524	18779.1	46	1	11	1.19	17	36	26.6	5
553	19063.8	28.3	1	11	1.31	17	40	46.9	5
B15	17767	80	1	11	1.6	17	14	11	B
425	18228.3	26.5	1	11	1.74	17	39	33	4 & B
610	20528.7	40	1	11	2.29	17	42	36.2	6
310	18355.7	14.7	1	11	2.35	18	3	33.5	3
453	19595.6	21.4	1	11	2.64	17	44	47.5	4
I75	18206	6	1	11	2.8	17	39	2	I
901	20257.9	28.8	1	11	2.81	17	39	46.6	1 & 2
902	18212.7	13.6	1	11	3.43	17	39	7.9	1, 2, D & E
I76	17591	15	1	11	3.5	17	38	59	I
B16	19065	80	1	11	3.6	17	14	31	B
402	18067.2	73.7	1	11	3.74	17	52	26.4	4
302	19723.1	50.2	1	11	3.77	17	53	41.6	3
D35	20107	33	1	11	3.8	17	39	47	C
I77	20279	15	1	11	4.2	17	39	14	I
429	17598	23.6	1	11	4.43	17	40	14	4 & B
530	21136.5	26.3	1	11	4.88	17	38	54.6	5
B17	18439	80	1	11	5.2	17	14	24	B
424	32096	43.7	1	11	5.21	17	27	40	4
B18	20689	80	1	11	5.4	17	14	30	B
369	17892.3	23.3	1	11	7.09	17	37	41.6	3
303	18908	54.1	1	11	7.21	17	34	49.8	3
344	12776.4	17.5	1	11	7.43	17	57	13.7	3

Continued on next page...

Table A.5: Radial velocities for Abell 154. The table includes all radial velocities, both newly presented here, and also those found in the literature through 2016. Column (1) represents the unique identifier assigned to each galaxy for the purpose of this study. Columns (2) and (3) are the heliocentric radial velocity and uncertainty, respectively. Columns (4)-(6) and (7)-(9) are the right ascension and declination of each galaxy, respectively. Column (10) is the source of the data by field (if it were our observation) and/or citation letter which is based on the identifications given in Table 3.4 (if data from the literature were used).

Continued from previous page...

	cz	σ	R.A. (J2000)			Dec. (J2000)			
ID	($km\ s^{-1}$)	($km\ s^{-1}$)	h	m	s	°	′	″	Source
(1)	(2)	(3)	(4)	(5)	(6)	(7)	(8)	(9)	(10)
B20	19889	80	1	11	7.7	17	38	51	B
421	17319.9	24.7	1	11	8.02	17	41	22.2	4
496	19831.3	17.6	1	11	8.58	17	30	46.6	4
210	18520.1	35.8	1	11	8.73	17	51	0.1	2
413	18877.8	17.7	1	11	8.77	17	35	34.5	4
510	36045.1	40.5	1	11	8.9	18	8	46.5	5
B21	18086	80	1	11	9	17	39	15	B
H66	22256	50	1	11	9.2	17	57	20	H
244	18416.3	23.3	1	11	9.73	18	2	59.6	2, C & H
460	28703	15.5	1	11	10.24	17	26	19.7	4
491	18289.3	17.6	1	11	10.36	17	46	20.9	4
349	19541.3	34.4	1	11	10.37	17	41	36	3
334	18391	25.6	1	11	11.15	17	51	54.8	3
406	20121.6	17.7	1	11	11.27	17	43	6.3	4
312	19373.7	14.7	1	11	11.8	17	59	45.9	3 & H
276	17689	16.4	1	11	12.08	17	42	14.9	2
306	22338.3	23	1	11	12.27	17	56	39.3	3
802	18210.5	10.3	1	11	12.31	17	14	26.9	3 & 4
512	18195.6	15.3	1	11	12.51	17	54	0.2	5
644	20776	63.9	1	11	12.81	17	57	15.4	6
217	13071.8	38.2	1	11	13.89	17	32	25.8	2
469	20180	25.9	1	11	15.22	17	37	49.6	4
H67	18544	50	1	11	15.8	17	57	20	H
412	45578.7	70.6	1	11	15.86	17	56	37	4
487	19449.1	24.2	1	11	15.92	17	36	38.5	4
299	10026.6	15.4	1	11	17.21	17	14	53	2
535	19890.7	34.1	1	11	17.31	17	42	36.1	5
F46	10150	101	1	11	17.5	17	15	26	F
521	18693.6	17.6	1	11	19	17	44	51.8	5
559	33810.9	35.2	1	11	19.16	17	48	4.4	5
801	19624.1	23.1	1	11	25.02	17	32	34.3	4 & 5
309	19185.8	29.1	1	11	25.57	17	40	34.6	3 & A
181	12573.7	28.4	1	11	26.36	17	26	54	1 & F
240	18569.6	18.9	1	11	28.02	17	56	48.2	2

Continued on next page...

Table A.5: Radial velocities for Abell 154. The table includes all radial velocities, both newly presented here, and also those found in the literature through 2016. Column (1) represents the unique identifier assigned to each galaxy for the purpose of this study. Columns (2) and (3) are the heliocentric radial velocity and uncertainty, respectively. Columns (4)-(6) and (7)-(9) are the right ascension and declination of each galaxy, respectively. Column (10) is the source of the data by field (if it were our observation) and/or citation letter which is based on the identifications given in Table 3.4 (if data from the literature were used).

Continued from previous page...

	cz	σ	R.A. (J2000)			Dec. (J2000)			
ID	($km\ s^{-1}$)	($km\ s^{-1}$)	h	m	s	°	′	″	Source
(1)	(2)	(3)	(4)	(5)	(6)	(7)	(8)	(9)	(10)
499	18512.7	41.8	1	11	28.04	17	13	48	4
481	18301.8	28.8	1	11	29.16	17	27	18.5	4
396	12513.5	34.4	1	11	29.33	17	17	5.4	3
386	19595.2	24.7	1	11	29.78	17	46	10.9	3
474	23460.4	33.9	1	11	30.37	17	39	29.7	4
387	32908.5	33.4	1	11	30.5	17	34	17.1	3
254	18361.7	31.5	1	11	30.67	17	27	29.2	2
288	19645.5	14.9	1	11	31.25	17	36	36.4	2 & A
434	18645.8	15	1	11	31.83	17	54	38.3	4
509	18422.4	47.4	1	11	32.43	17	39	31.3	5
508	47769.6	100.3	1	11	32.47	17	57	10.1	5
317	11187.9	17.6	1	11	36.09	17	28	7.7	3
549	45367.9	56.9	1	11	37.06	17	53	17.4	5
249	19317.2	35.9	1	11	40.42	17	54	43.6	2
296	31819.7	60.7	1	11	41.3	17	13	42.2	2
701	12525	26.9	1	11	42.31	17	17	0.2	2 & 3
352	12652.3	12	1	11	42.73	17	24	16.6	3
418	18729.2	15.2	1	11	43.35	17	30	49.5	4
G59	18633	59	1	11	45.24	16	53	10.5	G
476	18114.9	17.6	1	11	46.19	17	48	43.6	4
561	16316.3	13.2	1	11	46.25	17	54	52.8	5
F48	19172	96	1	11	46.9	16	54	35	F
503	19141.5	17.8	1	11	49.35	17	30	11.5	5
592	68686	100.4	1	11	50.32	18	4	20.6	5
557	19264	28.6	1	11	50.42	17	46	54.9	5
461	16426.6	17.6	1	11	51.62	17	56	2.1	4
532	16259.2	15.9	1	11	51.89	17	51	51.1	5
207	14080.6	39.3	1	11	52.87	17	18	5.1	2
454	12062.8	15.8	1	11	53.54	17	20	28.4	4
307	12633.8	29.5	1	11	54.01	17	14	37.5	3
107	12798.9	15	1	11	58.77	17	16	12.8	1
154	12596.6	22.1	1	12	0.41	17	18	34.8	1 & D
552	12569.8	41.9	1	12	1.18	17	19	15.8	5
321	36164.5	42	1	12	3.67	17	48	39.1	3

Continued on next page...

Table A.5: Radial velocities for Abell 154. The table includes all radial velocities, both newly presented here, and also those found in the literature through 2016. Column (1) represents the unique identifier assigned to each galaxy for the purpose of this study. Columns (2) and (3) are the heliocentric radial velocity and uncertainty, respectively. Columns (4)-(6) and (7)-(9) are the right ascension and declination of each galaxy, respectively. Column (10) is the source of the data by field (if it were our observation) and/or citation letter which is based on the identifications given in Table 3.4 (if data from the literature were used).

Continued from previous page...

	cz	σ	R.A. (J2000)			Dec. (J2000)			
ID	($km\ s^{-1}$)	($km\ s^{-1}$)	h	m	s	°	′	″	Source
(1)	(2)	(3)	(4)	(5)	(6)	(7)	(8)	(9)	(10)
313	19551.1	33	1	12	3.87	17	31	17.8	3
252	12738.8	34.2	1	12	4.08	17	18	53.7	2
218	19058.8	17.6	1	12	4.57	17	22	20.7	2
333	18221.4	15.1	1	12	10.52	17	42	57.3	3
114	12639.9	33.4	1	12	12.63	17	19	8.3	1
621	20871.8	20.2	1	12	17.06	17	50	19.2	6
117	12490.3	37	1	12	19.17	17	21	20.2	1
403	36091.4	77.9	1	12	20.79	17	28	9.2	4
555	54303.6	53.4	1	12	21.85	17	24	14.6	5
569	17989	16.1	1	12	23.94	17	37	59.7	5
473	12669.8	49.3	1	12	30.21	17	23	25.1	4
529	23428.3	16.4	1	12	37.93	17	51	36.5	5
348	19309.1	15.2	1	12	39.19	17	29	53.4	3
357	32234.3	43.3	1	12	42.07	17	54	10.5	3
388	19066.7	25.7	1	12	42.55	17	30	15.7	3
416	12837.2	47.2	1	12	46.59	17	33	24.3	4
320	28811.5	30.9	1	12	48.71	17	43	7.2	3
478	28695.4	16.3	1	12	48.82	17	39	44	4
374	19447.5	14.9	1	13	1.01	17	43	26.3	3
295	18854.9	48.9	1	13	2.46	17	38	7.9	2
F49	17926	91	1	13	11.3	17	49	53	F
G60	17913	31	1	14	4.47	18	3	40.4	G

Table A.6: Subgroup membership. The table presents the assigned membership of Subgroups B1 and B2 based on the KMM algorithm. Column (1) represents the unique identifier assigned to each galaxy for the purpose of this study. Columns (2) and (3) are the heliocentric radial velocity and uncertainty, respectively. Columns (4)-(6) and (7)-(9) are the right ascension and declination of each galaxy, respectively. Column (10) and (11) are the fractional likelihood of membership to either Subgroups B1 or B2.

	cz	σ	R.A. (J2000)			Dec. (J2000)			KMM	
ID	($km\ s^{-1}$)	($km\ s^{-1}$)	h	m	s	°	′	″	B1	B2
(1)	(2)	(3)	(4)	(5)	(6)	(7)	(8)	(9)	(10)	(11)
G57	19410	64	1	7	12.87	17	59	37.9	0	1

Continued on next page...

Table A.6: Subgroup membership. The table presents the assigned membership of Subgroups B1 and B2 based on the KMM algorithm. Column (1) represents the unique identifier assigned to each galaxy for the purpose of this study. Columns (2) and (3) are the heliocentric radial velocity and uncertainty, respectively. Columns (4)-(6) and (7)-(9) are the right ascension and declination of each galaxy, respectively. Column (10) and (11) are the fractional likelihood of membership to either Subgroups B1 or B2.

Continued from previous page...

	cz	σ	R.A. (J2000)			Dec. (J2000)			KMM	
ID	($km\ s^{-1}$)	($km\ s^{-1}$)	h	m	s	°	′	″	B1	B2
(1)	(2)	(3)	(4)	(5)	(6)	(7)	(8)	(9)	(10)	(11)
504	20189.3	58.7	1	9	16.61	17	25	31.1	0.002	0.998
394	19576.5	15.3	1	9	36.29	17	50	48.5	0.022	0.978
441	19663.7	32.3	1	9	37.45	17	52	29	0.02	0.98
339	20346.7	27.6	1	9	40.86	17	53	12.9	0.002	0.998
683	18802.5	30.4	1	9	41.9	18	0	43.5	0.237	0.763
511	20107.2	17.5	1	9	46.29	17	32	34.3	0.013	0.987
498	20022.2	18.4	1	9	49.89	17	42	37	0.012	0.988
563	19897.3	17.5	1	9	50.71	17	27	8.7	0.067	0.933
689	18959.4	17.6	1	9	51.46	17	21	29.4	0.729	0.271
490	19486.3	25.3	1	9	54.55	17	36	23	0.112	0.888
338	19563.1	46.1	1	9	57.37	17	16	35.1	0.698	0.302
550	19451.3	15.1	1	10	1.05	17	35	55.1	0.169	0.831
419	19797.9	17.7	1	10	3.09	17	58	3.9	0.075	0.925
367	18937.7	15.2	1	10	8.11	17	49	16.9	0.392	0.608
145	18810.7	23.4	1	10	8.2	17	23	45.7	0.865	0.135
304	20060	17.8	1	10	12.85	17	32	20	0.044	0.956
482	18809.3	32.9	1	10	14.03	17	58	7.1	0.618	0.382
562	18629.6	17.6	1	10	17.65	17	15	2.2	0.989	0.011
547	19164.5	17.6	1	10	18.07	18	6	29.7	0.701	0.299
472	18840	16.6	1	10	20.21	17	54	25	0.6	0.4
451	18524.4	14.3	1	10	24.66	17	53	26	0.729	0.271
379	18875.4	15.2	1	10	27.95	17	30	15.7	0.811	0.189
656	19406.9	17.6	1	10	34.17	17	46	27.8	0.26	0.74
353	19272.8	15.7	1	10	34.6	18	2	40.8	0.575	0.425
670	19484.4	52.9	1	10	35.33	17	37	30.6	0.276	0.724
319	20303.4	14.8	1	10	36	17	45	59	0.008	0.992
462	19046.9	50.2	1	10	36.94	17	23	40.8	0.899	0.101
G58	19559	34	1	10	38.5	16	49	34.7	1	0
A02	20116	100	1	10	38.9	17	31	12	0.044	0.956
223	18338.9	25.6	1	10	38.99	17	11	49.6	0.998	0.002
294	17612.2	17.5	1	10	39.86	17	45	37.7	0.867	0.133
384	18579.3	31.1	1	10	40.54	17	44	14	0.76	0.24
F41	19231	100	1	10	42.8	17	40	57	0.42	0.58
264	20880	38.2	1	10	43.31	17	41	0.2	0	1
672	20202.3	32.7	1	10	44.9	17	45	13.6	0.011	0.989

Continued on next page...

Table A.6: Subgroup membership. The table presents the assigned membership of Subgroups B1 and B2 based on the KMM algorithm. Column (1) represents the unique identifier assigned to each galaxy for the purpose of this study. Columns (2) and (3) are the heliocentric radial velocity and uncertainty, respectively. Columns (4)-(6) and (7)-(9) are the right ascension and declination of each galaxy, respectively. Column (10) and (11) are the fractional likelihood of membership to either Subgroups B1 or B2.

Continued from previous page...

	cz	σ	R.A. (J2000)			Dec. (J2000)			KMM	
ID	($km\ s^{-1}$)	($km\ s^{-1}$)	h	m	s	°	′	″	B1	B2
(1)	(2)	(3)	(4)	(5)	(6)	(7)	(8)	(9)	(10)	(11)
526	17976.7	16.7	1	10	45.14	17	31	25.6	0.952	0.048
471	21198	34.1	1	10	45.32	17	41	47.2	0	1
168	18841.3	30.8	1	10	45.86	17	59	26.8	0.752	0.248
268	19386.3	40.4	1	10	47.85	18	8	22.6	0.659	0.341
337	18531.7	25.3	1	10	48.6	18	1	4.7	0.867	0.133
391	18569.4	33.5	1	10	48.76	17	52	44.5	0.776	0.224
370	20866.1	33.3	1	10	48.86	17	39	3.2	0	1
447	18867.8	23.1	1	10	49.43	17	50	35.4	0.631	0.369
456	20341.7	24.8	1	10	49.47	17	43	45.1	0.005	0.995
590	19774.1	34.9	1	10	54.91	17	39	13.5	0.076	0.924
246	19609.6	21.3	1	10	55.18	17	36	47.9	0.165	0.835
H64	18406	50	1	10	57.3	17	59	46	0.871	0.129
567	19740.6	28.7	1	10	57.91	17	39	40.1	0.079	0.921
372	18526.4	26.4	1	10	58.13	17	40	12.2	0.807	0.193
346	19279	27.9	1	10	58.37	17	37	43	0.378	0.622
415	17614	32.2	1	10	58.46	17	38	31.5	0.927	0.073
568	18598.5	21.4	1	11	0.33	17	47	20.6	0.733	0.267
426	18255	25.9	1	11	0.71	17	37	44.9	0.886	0.114
524	18779.1	46	1	11	1.19	17	36	26.6	0.747	0.253
553	19063.8	28.3	1	11	1.31	17	40	46.9	0.489	0.511
B15	17767	80	1	11	1.6	17	14	11	0.919	0.081
425	18228.3	26.5	1	11	1.74	17	39	33	0.875	0.125
610	20528.7	40	1	11	2.29	17	42	36.2	0.001	0.999
310	18355.7	14.7	1	11	2.35	18	3	33.5	0.909	0.091
453	19595.6	21.4	1	11	2.64	17	44	47.5	0.101	0.899
I75	18206	6	1	11	2.8	17	39	2	0.881	0.119
901	20257.9	28.8	1	11	2.81	17	39	46.6	0.005	0.995
902	18212.7	13.6	1	11	3.43	17	39	7.9	0.879	0.121
I76	17591	15	1	11	3.5	17	38	59	0.925	0.075
B16	19065	80	1	11	3.6	17	14	31	0.508	0.492
402	18067.2	73.7	1	11	3.74	17	52	26.4	0.866	0.134
302	19723.1	50.2	1	11	3.77	17	53	41.6	0.066	0.934
D35	20107	33	1	11	3.8	17	39	47	0.011	0.989
I77	20279	15	1	11	4.2	17	39	14	0.004	0.996
429	17598	23.6	1	11	4.43	17	40	14	0.918	0.082

Continued on next page...

Table A.6: Subgroup membership. The table presents the assigned membership of Subgroups B1 and B2 based on the KMM algorithm. Column (1) represents the unique identifier assigned to each galaxy for the purpose of this study. Columns (2) and (3) are the heliocentric radial velocity and uncertainty, respectively. Columns (4)-(6) and (7)-(9) are the right ascension and declination of each galaxy, respectively. Column (10) and (11) are the fractional likelihood of membership to either Subgroups B1 or B2.

Continued from previous page...

	cz	σ	R.A. (J2000)			Dec. (J2000)			KMM	
ID	($km\ s^{-1}$)	($km\ s^{-1}$)	h	m	s	°	′	″	B1	B2
(1)	(2)	(3)	(4)	(5)	(6)	(7)	(8)	(9)	(10)	(11)
530	21136.5	26.3	1	11	4.88	17	38	54.6	0	1
B17	18439	80	1	11	5.2	17	14	24	0.825	0.175
B18	20689	80	1	11	5.4	17	14	30	0	1
369	17892.3	23.3	1	11	7.09	17	37	41.6	0.919	0.081
303	18908	54.1	1	11	7.21	17	34	49.8	0.675	0.325
B20	19889	80	1	11	7.7	17	38	51	0.03	0.97
421	17319.9	24.7	1	11	8.02	17	41	22.2	0.911	0.089
496	19831.3	17.6	1	11	8.58	17	30	46.6	0.077	0.923
210	18520.1	35.8	1	11	8.73	17	51	0.1	0.735	0.265
413	18877.8	17.7	1	11	8.77	17	35	34.5	0.669	0.331
B21	18086	80	1	11	9	17	39	15	0.887	0.113
244	18416.3	23.3	1	11	9.73	18	2	59.6	0.879	0.121
491	18289.3	17.6	1	11	10.36	17	46	20.9	0.804	0.196
349	19541.3	34.4	1	11	10.37	17	41	36	0.103	0.897
334	18391	25.6	1	11	11.15	17	51	54.8	0.775	0.225
406	20121.6	17.7	1	11	11.27	17	43	6.3	0.006	0.994
312	19373.7	14.7	1	11	11.8	17	59	45.9	0.247	0.753
276	17689	16.4	1	11	12.08	17	42	14.9	0.899	0.101
802	18210.5	10.3	1	11	12.31	17	14	26.9	0.997	0.003
512	18195.6	15.3	1	11	12.51	17	54	0.2	0.831	0.169
644	20776	63.9	1	11	12.81	17	57	15.4	0	1
469	20180	25.9	1	11	15.22	17	37	49.6	0.005	0.995
H67	18544	50	1	11	15.8	17	57	20	0.737	0.263
487	19449.1	24.2	1	11	15.92	17	36	38.5	0.153	0.847
535	19890.7	34.1	1	11	17.31	17	42	36.1	0.015	0.985
521	18693.6	17.6	1	11	19	17	44	51.8	0.571	0.429
801	19624.1	23.1	1	11	25.02	17	32	34.3	0.069	0.931
309	19185.8	29.1	1	11	25.57	17	40	34.6	0.189	0.811
240	18569.6	18.9	1	11	28.02	17	56	48.2	0.597	0.403
499	18512.7	41.8	1	11	28.04	17	13	48	0.993	0.007
481	18301.8	28.8	1	11	29.16	17	27	18.5	0.922	0.078
386	19595.2	24.7	1	11	29.78	17	46	10.9	0.025	0.975
254	18361.7	31.5	1	11	30.67	17	27	29.2	0.903	0.097
288	19645.5	14.9	1	11	31.25	17	36	36.4	0.028	0.972
434	18645.8	15	1	11	31.83	17	54	38.3	0.467	0.533

Continued on next page...

Table A.6: Subgroup membership. The table presents the assigned membership of Subgroups B1 and B2 based on the KMM algorithm. Column (1) represents the unique identifier assigned to each galaxy for the purpose of this study. Columns (2) and (3) are the heliocentric radial velocity and uncertainty, respectively. Columns (4)-(6) and (7)-(9) are the right ascension and declination of each galaxy, respectively. Column (10) and (11) are the fractional likelihood of membership to either Subgroups B1 or B2.

Continued from previous page...

	cz	σ	R.A. (J2000)			Dec. (J2000)			KMM	
ID	$(km\ s^{-1})$	$(km\ s^{-1})$	h	m	s	°	′	″	B1	B2
(1)	(2)	(3)	(4)	(5)	(6)	(7)	(8)	(9)	(10)	(11)
509	18422.4	47.4	1	11	32.43	17	39	31.3	0.643	0.357
249	19317.2	35.9	1	11	40.42	17	54	43.6	0.045	0.955
418	18729.2	15.2	1	11	43.35	17	30	49.5	0.485	0.515
G59	18633	59	1	11	45.24	16	53	10.5	1	0
476	18114.9	17.6	1	11	46.19	17	48	43.6	0.518	0.482
F48	19172	96	1	11	46.9	16	54	35	1	0
503	19141.5	17.8	1	11	49.35	17	30	11.5	0.121	0.879
557	19264	28.6	1	11	50.42	17	46	54.9	0.021	0.979
313	19551.1	33	1	12	3.87	17	31	17.8	0.004	0.996
218	19058.8	17.6	1	12	4.57	17	22	20.7	0.148	0.852
333	18221.4	15.1	1	12	10.52	17	42	57.3	0.115	0.885
621	20871.8	20.2	1	12	17.06	17	50	19.2	0	1
569	17989	16.1	1	12	23.94	17	37	59.7	0.073	0.927
348	19309.1	15.2	1	12	39.19	17	29	53.4	0	1
388	19066.7	25.7	1	12	42.55	17	30	15.7	0	1
374	19447.5	14.9	1	13	1.01	17	43	26.3	0	1
295	18854.9	48.9	1	13	2.46	17	38	7.9	0	1
F49	17926	91	1	13	11.3	17	49	53	0	1
G60	17913	31	1	14	4.47	18	3	40.4	0	1

A.4 Stellar Data

Observations of stars is presented in Table A.7. This table includes all radial velocities for the stars that were observed. It should be noted that the radial velocities for these stars were obtained using galaxy reference spectra rather than stellar reference spectra. Column (1) represents the unique identifier assigned to each star. This identification value is defined in a manner that can be used to trace it directly back to the source field and aperture of the observations, according to Table 3.1 and Section 3.1.2. The first digit represents the field value and the last two digits represent the aperture value within that field. Columns (2) and

(3) are the heliocentric radial velocity and uncertainty, respectively. Radial velocity values that are negative indicates a velocity towards us, whereas a positive radial velocity indicates a velocity away from us. Columns (4)-(6) and (7)-(9) are the right ascension and declination of each star, respectively, in the J2000 epoch.

Table A.7: Radial velocities for foreground stars. The table includes all radial velocities for the stars that were observed. Column (1) represents the unique identifier assigned to each star. Columns (2) and (3) are the heliocentric radial velocity and uncertainty, respectively. Columns (4)-(6) and (7)-(9) are the right ascension and declination of each star, respectively. It should be noted that the radial velocities for these stars were obtained using galaxy reference spectra rather than stellar reference spectra.

	cz	σ	R.A. (J2000)			Dec. (J2000)		
ID	($km\ s^{-1}$)	($km\ s^{-1}$)	h	m	s	$^\circ$	$'$	$''$
(1)	(2)	(3)	(4)	(5)	(6)	(7)	(8)	(9)
298	-29.65	31.37	1	9	5.86	17	44	39.8
584	6.16	27.6	1	9	7.19	17	46	1.6
642	-151.05	37.63	1	9	8.44	17	39	18
393	-91.22	51.87	1	9	8.63	17	48	8.2
165	-11.25	29.88	1	9	8.91	17	35	27.1
284	19.43	15.29	1	9	14.96	17	45	11
170	-49.62	29.14	1	9	15.77	17	38	14.3
141	-7.65	21.13	1	9	18.97	17	54	53.8
341	34.34	16.72	1	9	19.15	17	55	35.8
242	-44.21	16.24	1	9	19.39	17	38	53.7
505	-7.53	29.7	1	9	23.73	17	49	50.2
190	-72.59	27.03	1	9	24.04	17	36	2.2
527	1.59	29.08	1	9	24.21	17	40	40.5
184	7.81	33.08	1	9	24.84	17	45	47.2
111	62.51	21.01	1	9	27.08	17	30	51
139	-16.33	28.35	1	9	29.39	17	55	53.8
105	9.64	13.89	1	9	30.75	17	47	49.2
239	19.42	20.4	1	9	33.25	17	54	49.6
183	-39.01	15.67	1	9	34.1	18	0	41.1
167	-15.02	41.38	1	9	35.36	17	56	51.1
267	-37.23	50.22	1	9	35.36	17	56	51.1
205	-24.05	29.29	1	9	35.75	17	47	24.2
305	-17.18	23.87	1	9	35.75	17	47	24.2
256	-47.75	19.78	1	9	41.11	17	56	38.5
197	-67.05	20.48	1	9	42.06	17	29	28
194	-23.01	23.2	1	9	43.48	17	48	34.4
283	-15.43	35.04	1	9	47.26	17	55	30.6
146	8.16	37.09	1	9	48.81	17	23	52.1

Continued on next page...

Table A.7: Radial velocities for foreground stars. The table includes all radial velocities for the stars that were observed. Column (1) represents the unique identifier assigned to each star. Columns (2) and (3) are the heliocentric radial velocity and uncertainty, respectively. Columns (4)-(6) and (7)-(9) are the right ascension and declination of each star, respectively. It should be noted that the radial velocities for these stars were obtained using galaxy reference spectra rather than stellar reference spectra.

Continued from previous page...

	cz	σ	R.A. (J2000)			Dec. (J2000)		
ID	($km\ s^{-1}$)	($km\ s^{-1}$)	h	m	s	$^\circ$	$'$	$''$
(1)	(2)	(3)	(4)	(5)	(6)	(7)	(8)	(9)
189	-10.25	51.35	1	9	49.13	17	18	55.9
570	-136.5	56.72	1	9	51.18	17	38	33
138	-60.24	39.83	1	9	52.68	17	15	45.7
266	10.86	39.05	1	9	54.51	17	16	50
289	69.34	47.58	1	9	54.89	17	18	1.7
293	-25.23	45.24	1	9	55.28	17	44	34.4
422	15.36	38.2	1	9	55.79	18	4	55.1
263	-86.14	32.38	1	9	56.69	17	27	34
564	-20.06	58.21	1	10	0.23	17	41	20.4
166	-5.49	16.41	1	10	2.14	17	21	53.9
280	-34.34	53.34	1	10	2.14	17	21	53.9
597	-9.85	37.33	1	10	3.66	17	31	9.8
480	-39.6	32.94	1	10	3.69	17	26	24.8
382	-57.56	19.81	1	10	6.31	18	6	7.6
350	-16.55	21.35	1	10	9.14	17	36	21.9
211	21.3	15.06	1	10	10.46	17	35	22.6
580	46.21	69.78	1	10	11.72	17	28	16.7
185	1.72	15.84	1	10	13.11	17	15	46.9
680	13.11	51.73	1	10	13.82	17	28	49.7
119	-30.75	23.89	1	10	14.39	17	51	31
411	52.93	34.79	1	10	14.92	17	37	7.8
198	-51.83	18.01	1	10	16.58	17	42	15.3
551	-42.94	28.21	1	10	16.69	18	2	56.6
172	-96.12	28.46	1	10	17.55	17	52	0.9
147	-36.24	18.95	1	10	20.13	18	7	10.1
325	-68.01	37.06	1	10	21.93	17	37	13.4
245	-27.83	33.15	1	10	22.65	17	26	31.2
151	48.41	18.94	1	10	25	18	2	27.5
241	-4.19	33.2	1	10	27.5	17	47	41
467	14.33	21.7	1	10	27.63	17	46	38.3
164	-54.98	28.95	1	10	27.7	17	40	48.8
443	-32.25	31.11	1	10	28.59	17	15	37.1
323	-26.74	18.39	1	10	28.83	17	12	4.4
543	-58.27	48	1	10	29.28	17	16	3.3
523	-32.55	27.14	1	10	30.53	17	14	19.6

Continued on next page...

Table A.7: Radial velocities for foreground stars. The table includes all radial velocities for the stars that were observed. Column (1) represents the unique identifier assigned to each star. Columns (2) and (3) are the heliocentric radial velocity and uncertainty, respectively. Columns (4)-(6) and (7)-(9) are the right ascension and declination of each star, respectively. It should be noted that the radial velocities for these stars were obtained using galaxy reference spectra rather than stellar reference spectra.

Continued from previous page...

	cz	σ	R.A. (J2000)			Dec. (J2000)		
ID	($km\ s^{-1}$)	($km\ s^{-1}$)	h	m	s	$^\circ$	$'$	$''$
(1)	(2)	(3)	(4)	(5)	(6)	(7)	(8)	(9)
643	-215.51	88.63	1	10	30.84	17	25	26.9
351	-23.85	45.7	1	10	31.37	17	54	4.4
191	-13.62	14.08	1	10	34.66	18	2	54.6
272	-12.01	27.75	1	10	34.76	17	47	13
125	-81.37	19.73	1	10	35.01	17	34	53.4
104	11.65	19.41	1	10	37.61	17	33	54.8
153	20.15	15.63	1	10	38.59	17	58	14
143	-40.98	26.9	1	10	39.08	17	20	30.5
179	6.34	17.55	1	10	39.26	17	31	9.3
285	-2.08	14.75	1	10	39.26	17	31	9.3
253	-14.82	53.49	1	10	40.33	17	55	53.8
438	-48.96	25.48	1	10	41.47	17	32	18.2
398	27.97	20.69	1	10	42.22	17	40	57.4
182	-38.96	19.78	1	10	42.59	17	46	58
222	-47.45	21.97	1	10	42.59	17	46	58
123	-12.61	23.93	1	10	44.07	17	22	55.8
142	-24.83	14.4	1	10	45.08	17	40	9.3
442	21.71	18.52	1	10	46.53	17	40	35.1
204	-0.64	26.45	1	10	48.14	17	36	50.9
115	3.84	33.32	1	10	49	17	11	29
326	-66.74	45.08	1	10	50.35	17	19	35
385	-1.32	19.88	1	10	54.02	17	32	54.1
150	-11.4	22.2	1	10	54.42	17	37	26.5
389	-140.96	31.63	1	10	56.28	17	35	17.8
297	-45.93	17	1	10	59.28	17	39	39.3
126	7.87	29.94	1	11	1.07	17	19	38.2
226	10.02	35.2	1	11	1.29	17	24	23.7
277	-18.48	21.23	1	11	2.09	17	19	36.4
477	-22.06	35.58	1	11	2.14	17	26	57.8
177	-13.25	42.54	1	11	2.62	17	16	13.4
124	6.28	17.66	1	11	4.24	17	12	50.6
502	83.23	67.03	1	11	4.35	17	57	42.6
377	-33.84	29.61	1	11	5.81	17	23	46.5
108	-11.71	17.1	1	11	10.49	17	49	9.2
212	-11.7	18.55	1	11	10.49	17	49	9.2

Continued on next page...

Table A.7: Radial velocities for foreground stars. The table includes all radial velocities for the stars that were observed. Column (1) represents the unique identifier assigned to each star. Columns (2) and (3) are the heliocentric radial velocity and uncertainty, respectively. Columns (4)-(6) and (7)-(9) are the right ascension and declination of each star, respectively. It should be noted that the radial velocities for these stars were obtained using galaxy reference spectra rather than stellar reference spectra.

Continued from previous page...

	cz	σ	R.A. (J2000)			Dec. (J2000)		
ID	($km\ s^{-1}$)	($km\ s^{-1}$)	h	m	s	$^\circ$	$'$	$''$
(1)	(2)	(3)	(4)	(5)	(6)	(7)	(8)	(9)
316	3.95	45.63	1	11	10.92	17	35	44.8
130	-13.87	23.56	1	11	11.94	17	13	31.7
136	-43.4	31.7	1	11	12.32	17	39	50.2
230	-29.3	17.72	1	11	13.33	17	13	54.3
436	-35.14	26.56	1	11	13.85	17	39	56.6
330	-4.2	79.49	1	11	14.41	17	14	1.2
331	-131.33	25.21	1	11	16.11	17	26	56.8
216	-14.48	27.34	1	11	16.58	17	38	4.4
199	-3.84	15.15	1	11	17.56	17	18	17.7
576	-121.43	58.25	1	11	18.76	17	46	14.5
332	-80.25	24.69	1	11	19.39	17	43	7
112	-2	40.43	1	11	19.49	18	4	41.6
134	10.64	22.18	1	11	19.53	17	55	32.8
131	-45.96	26.92	1	11	20.59	17	26	49.9
273	-39.51	20.11	1	11	20.68	17	32	58.7
118	-7.74	40.9	1	11	20.78	17	29	54.8
314	28.45	72.99	1	11	20.78	17	29	54.8
328	-10.43	21.08	1	11	22.22	17	48	11.5
440	2.35	26.88	1	11	22.51	17	53	10.6
155	15.77	33.27	1	11	22.83	17	31	43.7
340	-15.39	21.99	1	11	22.93	17	59	29.3
354	-14.36	15.55	1	11	23.05	17	27	53.6
449	-16.84	15.47	1	11	24.18	17	51	3.5
206	-14.92	23.92	1	11	25.49	18	3	16.3
103	-7.33	23.53	1	11	26.22	17	33	48.3
229	-18.67	38.07	1	11	27.62	17	42	0.4
140	-4.28	76.22	1	11	28.44	18	4	11.8
506	-85.8	102.84	1	11	28.65	18	0	6.4
540	-42.22	19.78	1	11	28.83	17	56	5.7
574	-22.61	20.75	1	11	32.75	17	40	11.9
635	30.03	44.67	1	11	34.01	17	39	33.4
507	-38.43	32.77	1	11	34.49	17	24	39.6
208	-48.09	13.78	1	11	36.23	17	58	40.4
531	23.31	38.65	1	11	40.36	17	17	54.3
234	22.91	28.73	1	11	42.41	18	7	55.8

Continued on next page...

Table A.7: Radial velocities for foreground stars. The table includes all radial velocities for the stars that were observed. Column (1) represents the unique identifier assigned to each star. Columns (2) and (3) are the heliocentric radial velocity and uncertainty, respectively. Columns (4)-(6) and (7)-(9) are the right ascension and declination of each star, respectively. It should be noted that the radial velocities for these stars were obtained using galaxy reference spectra rather than stellar reference spectra.

Continued from previous page...

	cz	σ	R.A. (J2000)			Dec. (J2000)		
ID	($km\ s^{-1}$)	($km\ s^{-1}$)	h	m	s	$^\circ$	$'$	$''$
(1)	(2)	(3)	(4)	(5)	(6)	(7)	(8)	(9)
492	-31.69	91.56	1	11	42.97	17	58	14.9
113	-70.32	36.56	1	11	44.82	17	33	30.2
631	-142.93	48.26	1	11	45.07	17	13	51.4
452	-14.99	23.13	1	11	46.03	17	26	0.8
495	0.44	45.17	1	11	47.25	17	38	10.2
329	-6.5	21.08	1	11	47.37	17	44	45.5
116	-45.66	28.82	1	11	48.54	17	36	38.4
228	-41.53	26.22	1	11	49.35	17	58	31.3
428	-47.28	20.83	1	11	51.76	18	0	5
148	-55.47	22.37	1	11	52.53	17	33	25.5
188	-17.66	22.81	1	11	53.37	17	35	41.2
528	14	64.31	1	11	54.1	18	3	6.1
359	18.02	16.74	1	11	54.12	17	53	33.3
628	-53.14	39.99	1	11	57.82	18	2	5.5
261	15.72	24.27	1	11	59.24	17	57	40.4
152	-49.79	25.69	1	12	3.92	17	18	23.6
128	-36.67	17.67	1	12	4.09	18	2	56.8
149	24.7	35.93	1	12	4.21	17	59	34.2
417	1.44	32.58	1	12	5.4	17	26	25.4
355	-0.42	32.83	1	12	5.43	17	26	25.6
209	23.66	14.1	1	12	5.74	17	41	1.7
361	-11.97	16.32	1	12	6.71	18	0	34.2
159	-20.39	19.24	1	12	7.16	17	57	41.1
161	-13.86	35.87	1	12	8.34	17	59	48
278	-25.18	14.28	1	12	14.63	17	38	10.7
259	4.74	21.61	1	12	16.07	17	58	37.2
173	-5.48	19.94	1	12	16.11	17	25	22.1
213	-42.37	25.06	1	12	16.48	17	30	21.6
169	-5.31	38.8	1	12	16.81	17	38	22.9
132	-39.17	15.12	1	12	17.31	17	56	33.3
536	-24.79	60.32	1	12	19.67	17	47	55.8
287	23.67	29.44	1	12	19.72	17	34	27.8
248	2.76	14.8	1	12	32.35	17	31	6.4
157	-43.11	30.65	1	12	37.86	17	52	14.8
274	-4.79	22.58	1	12	39.18	17	42	27.3

Continued on next page...

Table A.7: Radial velocities for foreground stars. The table includes all radial velocities for the stars that were observed. Column (1) represents the unique identifier assigned to each star. Columns (2) and (3) are the heliocentric radial velocity and uncertainty, respectively. Columns (4)-(6) and (7)-(9) are the right ascension and declination of each star, respectively. It should be noted that the radial velocities for these stars were obtained using galaxy reference spectra rather than stellar reference spectra.

Continued from previous page...

	cz	σ	R.A. (J2000)			Dec. (J2000)		
ID	($km\ s^{-1}$)	($km\ s^{-1}$)	h	m	s	$^\circ$	$'$	$''$
(1)	(2)	(3)	(4)	(5)	(6)	(7)	(8)	(9)
174	-18.25	23.37	1	12	45.04	17	42	43.2
203	2.28	17.99	1	12	46.03	17	24	42.3
657	38.38	43.01	1	12	47.27	17	53	15.8
133	15.34	18.75	1	12	47.58	17	46	52.2
233	12.66	19.33	1	12	47.58	17	46	52.2
187	-56.76	28.04	1	12	48.15	17	33	1.9
409	-9.96	40.65	1	12	51.87	17	41	45.9
616	-90.71	35.2	1	12	52.54	17	33	7.8
674	-40.24	29.04	1	12	53.23	17	42	15.4
336	25.12	16.96	1	12	53.37	17	51	18.7
488	-36.9	52.27	1	12	56.16	17	30	32.9
195	-17.31	30.38	1	12	57.5	17	38	2.8
269	-40.82	36.86	1	12	58.05	17	36	56.2

Bibliography

Abell, G. O. 1957, Astronomical Journal, 62, 2

—. 1958, Astrophysical Journal Supplement Series, 3, 211

Abell, G. O., Corwin, Jr., H. G., & Olowin, R. P. 1989, Astrophysical Journal Supplement Series, 70, 1

Adami, C., Biviano, A., & Mazure, A. 1998, Astronomy and Astrophysics, 331, 439

Allen, S. W., Evrard, A. E., & Mantz, A. B. 2011, Annual Review of Astronomy and Astrophysics, 49, 409

Ashman, K. M., Bird, C. M., & Zepf, S. E. 1994, Astronomical Journal, 108, 2348

Austin, C. G. 2008, PhD thesis, University of Minnesota

Bahcall, N. A. 1977, Annual Review of Astronomy and Astrophysics, 15, 505

—. 1999, Clusters and Super Clusters of Galaxies (Cambridge University Press)

Baier, F. W. 1977, Astronomische Nachrichten, 298, 151

Balogh, M. L., Navarro, J. F., & Morris, S. L. 2000, Astrophysical Journal, 540, 113

Barkhouse, W. A., Yee, H. K. C., & López-Cruz, O. 2007, Astrophysical Journal, 671, 1471

Bautz, L. P., & Morgan, W. W. 1970, Astrophysical Journal, 162, L149

Beers, T. C., Flynn, K., & Gebhardt, K. 1990, Astronomical Journal, 100, 32

Beers, T. C., & Geller, M. J. 1983, Astrophysical Journal, 274, 491

Beers, T. C., Geller, M. J., & Huchra, J. P. 1982, Astrophysical Journal, 257, 23

Bender, R., Ziegler, B., & Bruzual, G. 1996, Astrophysical Journal Letters, 463, L51

Berrington, R. C., Lugger, P. M., & Cohn, H. N. 2002, Astronomical Journal, 123, 2261

Bevington, P. R., & Robinson, D. K. 2003, Data Reduction and Error Analysis for the Physical Sciences, 3rd edn. (McGraw-Hill)

Binney, J., & Merrifield, M. 1998, Galactic Astronomy (Princeton University Press)

Binney, J., & Tremaine, S. 2008, Galactic Dynamics, 2nd edn. (Princeton University Press)

Bird, C. M. 1994, Astronomical Journal, 107, 1637

Birkinshaw, M. 1999, Physics Reports, 310, 97

Birney, D. S., Gonzalez, G., & Oesper, D. 2006, Observational Astronomy, 2nd edn. (Cambridge University Press)

Blakeslee, J. P., & Tonry, J. L. 1992, Astronomical Journal, 103, 1457

Bothun, G. 1998, Modern Cosmological Observations and Problems (Taylor & Francis Group)

Brown, W. R. 2015, Annual Review of Astronomy and Astrophysics, 53, 15

Carroll, B. W., & Ostlie, D. A. 2006, An Introduction to Modern Astrophysics and Cosmology, 2nd edn. (Addison-Wesley)

Carter, D., & Metcalfe, N. 1980, Monthly Notices of the Royal Astronomical Society, 191, 325

Chandrasekhar, S. 1942, Principles of Stellar Dynamics (The University of Chicago Press)

—. 1943, Astrophysical Journal, 277, 255

D'Agostino, R. B., & Stephens, M. A. 1986, Goodness-of-Fit Techniques (Dekker)

Davenhall, A. C., & Leggett, S. K. 1997, VizieR Online Data Catalog, 6049

David, L. P., Hughes, J. P., & Tucker, W. H. 1992, Astrophysical Journal, 394, 452

De Grandi, S., & Molendi, S. 2002, Astrophysical Journal, 567, 163

De Propris, R., Colless, M., Peacock, J. A., et al.. 2004, Monthly Notices of the Royal Astronomical Society, 351, 125

Donahue, M., Horner, D. J., Cavagnolo, K. W., & Voit, G. M. 2006, Astrophysical Journal, 643, 730

Dressler, A. 1978a, Astrophysical Journal, 223, 765

—. 1978b, Astrophysical Journal, 226, 55

—. 1980a, Astrophysical Journal Supplement Series, 42, 565

Dressler, A. M. 1976, PhD thesis, California Univ., Santa Cruz.

—. 1980b, Astrophysical Journal, 236, 351

—. 1984, Annual Reviews of Astronomy and Astrophysics, 22, 185

Dressler, A. M., & Shectman, S. A. 1988, Astronomical Journal, 95, 985

Dubinski, J. 1998, Astrophysical Journal, 502, 141

Dyer, C. C., & Roeder, R. C. 1976, Nature, 260, 764

Edwards, L. O. V., Hudson, M. J., Balogh, M. L., & Smith, R. J. 2007, Monthly Notices of the Royal Astronomical Society, 379, 100

Efron, B., & Tibshirani, R. 1986, Statistical Science, 1, 54

Einstein, A. 1911, Annalen der Physik, 340, 898

Elvis, M., Plummer, D., Schachter, J., & Fabbiano, G. 1992, Astrophysical Journal Supplement Series, 80, 257

Faber, S. M., & Dressler, A. M. 1977, Astronomical Journal, 82, 187

Faber, S. M., & Gallagher, J. S. 1979, Annual Reviews of Astronomy & Astrophysics, 17, 135

Faber, S. M., & Jackson, R. E. 1976, Astrophysical Journal, 204, 668

Fabian, A. C. 1994, Annual Reviews of Astronomy and Astrophysics, 32, 277

—. 2012, Annual Reviews in Astronomy and Astrophysics, 50, 455

Fabian, A. C., Nulsen, P. E. J., & Canizares, C. R. 1991, Astronomy and Astrophysics Review, 2, 191

Fabian, A. C., & Sanders, J. S. 2009, in American Institute of Physics Conference Series, Vol. 1201, 275

Fairall, A. P. 1992, The Observatory, 112, 286

Falco, E. E., Kurtz, M. J., Geller, M. J., et al.. 1999, Publications of the Astronomical Society of the Pacific, 111, 438

Fanti, C., Fanti, R., Feretti, L., et al.. 1983, Astronomy and Astrophysics Supplement Series, 51, 179

Feretti, L., & Giovannini, G. 1994, Astrophysical Journal, 281, 375

Fitchett, M. 1988, Monthly Notices of the Royal Astronomical Society, 230, 161

Forman, W., & Jones, C. 1990, in Clusters of Galaxies, 257

Forman, W. R., & Jones, C. 1982, Annual Reviews of Astronomy and Astrophysics, 20, 547

Gal, R. R., de Carvalho, R. R., Brunner, R., Odewahn, S. C., & Djorgovski, S. G. 2000, Astronomical Journal, 120, 540

Geller, M. J., & Beers, T. C. 1982, Publications of the Astronomical Society of the Pacific, 94, 421

Geller, M. J., & Huchra, J. P. 1989, Science, 246, 897

Giovanelli, R., & Haynes, M. P. 1993, Astronomical Journal, 105, 1271

Grubbs, F. E. 1950, Annals of Mathematical Statistics, 21, 27

Guthrie, B. N. G. 1974, Monthly Notices of the Royal Astronomical Society, 168, 15

Hamwey, R. M. 1989, PhD thesis, Dartmouth University

Hartigan, J. A., & Hartigan, P. M. 1985, Annals of Statistics, 13, 70

Harvey, D., Massey, R., Kitching, T., Taylor, A., & Tittley, E. 2015, Science, 347, 1462

Haynes, M. P., van Zee, L., Hogg, D. E., Roberts, M. S., & Maddalena, R. J. 1998, Astronomical Journal, 115, 62

Heisler, J., Tremaine, S., & Bahcall, J. N. 1985, Astrophysical Journal, 298, 8

Hoffman, G. L., & Williams, H. L. 1991, Astronomical Journal, 101, 325

Hogg, D. W. 1999, ArXiv Astrophysics e-prints, astro-ph/9905116

Hubble, E. 1929, Contributions from the Mount Wilson Observatory, vol. 3, pp.23-28, 3, 23

Huchra, J. P., Davis, M., Latham, D., & Tonry, J. L. 1983, Astrophysical Journal Supplement Series, 52, 89

Huchra, J. P., Vogeley, M. S., & Geller, M. J. 1999, Astrophysical Journal Supplement, 121, 287

Huchra, J. P., Macri, L. M., Masters, K. L., et al.. 2012, VizieR Online Data Catalog, 219

Iglewicz, B. 1983, Robust Scale Estimators and Confidence Intervals for Location. (John Wiley and Sons), 405–431

Jacoby, G. H., Branch, D., Ciardullo, R., et al.. 1992, Publications of the Astronomical Society of the Pacific, 104, 599

Jarvis, J. F., & Tyson, J. A. 1981, Astronomical Journal, 86, 476

Jones, C., & Forman, W. 1984, Astrophysical Journal, 276, 38

Kahlhoefer, F., Schmidt-Hoberg, K., Frandsen, M. T., & Sarkar, S. 2014, Monthly Notices of the Royal Astronomical Society, 437, 2865

Kaiser, N. 1984, Astrophysical Journal Letters, 284, 9

Koda, J. 2009, PhD thesis, The University of Texas at Austin

Kormendy, J., & Djorgovski, S. 1989, Annual Review of Astronomy and Astrophysics, 27, 235

Kravtsov, A. V., & Borgani, S. 2012, Annual Review of Astronomy and Astrophysics, 50, 353

Kriessler, J. R., & Beers, T. C. 1997, Astronomical Journal, 113, 80

Lauer, T. R., Postman, M., Strauss, M. A., Graves, G. J., & Chisari, N. E. 2014, Astrophysical Journal, 797, 82

Ledlow, M. J., & Owen, F. N. 1995, Astronomical Journal, 110, 1959

Lee, K. L. 1979, Journal of the American Statistical Association, 68, 159

Leo, W. R. 1994 (Springer-Verlag)

Loken, C., Melott, A. L., & Miller, C. J. 1999, Astrophysical Journal, 520, L5

Loubser, S. I., Sansom, A. E., Sánchez-Blázquez, P., Soechting, I. K., & Bromage, G. E. 2008, Monthly Notices of the Royal Astronomical Society, 391, 1009

Lynden-Bell, D. 1967, Monthly Notices of the Royal Astronomical Society, 136, 101

Magri, C., Haynes, M. P., Forman, W., Jones, C., & Giovanelli, R. 1988, Astrophysical Journal, 333, 136

Makino, N., & Tomita, K. 1995, Publications of the Astronomical Society of Japan, 47, 117

McDowell, J. C., ed. 1994, The Einstein Observatory Soft X-ray Source List

McLachlan, G. J. 1987, Journal of the Royal Statistical Society. Series C (Applied Statistics), 36, 318

McLachlan, G. J., & Basford, K. E. 1988, Mixture Models. Inference and Applications to Clustering (CRC Press)

McMillan, S. L. W., Kowalski, M. P., & Ulmer, M. P. 1989, Astrophysical Journal Supplement Series, 70, 723

McNamara, B. R., & Nulsen, P. E. J. 2007, Annual Reviews of Astronomy and Astrophysics, 45, 117

Merrifield, M. R., & Kent, S. M. 1991, Astronomical Journal, 101, 783

Merritt, D. 1984a, Astrophysical Journal, 276, 26

—. 1984b, Astrophysical Journal Letters, 280, L5

—. 1985, Astrophysical Journal, 289, 18

Moore, B., Katz, N., Lake, G., Dressler, A., & Oemler, A. 1996, Nature, 379, 613

Moran, S. M. 2008, PhD thesis, California Institute of Technology

Muratov, A. L., & Gnedin, O. Y. 2010, Astrophysical Journal, 718, 1266

Myers, S. T., Baker, J. E., Readhead, A. C. S., Leitch, E. M., & Herbig, T. 1997, Astrophysical Journal, 485, 1

Navarro, J. F., Frenk, C. S., & White, S. D. M. 1995, Monthly Notices of the Royal Astronomical Society, 275, 720

Ness, J.-U., ed. 2012, Galaxy Clusters as Giant Cosmic Laboratories

Ochsenbein, F., Bauer, P., & Marcout, J. 2000, Astronomy and Astrophysics Supplement, 143, 23

Ostriker, J. P. 1980, Comments on Astrophysics, 8, 177

Ostriker, J. P., & Tremaine, S. D. 1975, Astrophysical Journal Letters, 202, L113

Owen, F. N. 1974, Astronomical Journal, 79, 427

Owen, F. N., & Ledlow, M. J. 1995, Astronomical Journal, 109, 14

—. 1997, Astrophysical Journal Supplement Series, 108, 41

Paolillo, M., Andreon, S., Longo, G., et al.. 2001, Astronomy and Astrophysics, 367, 59

Pearson, E. S., & Hartley, H. O. 1962, Biometrika Tables for Statisticians (Cambridge University Press)

Pearson, E. S., & Stephens, M. A. 1964, Biometrika, 51, 484

Peterson, J. R., Kahn, S. M., Paerels, F. B. S., et al.. 2003, Astrophysical Journal, 590, 207

Pinkney, J., Roettiger, K., Burns, J. O., & Bird, C. M. 1996, Astrophysical Journals, 104, 1

Porter, A. C., Schneider, D. P., & Hoessel, J. G. 1991, Astronomical Journal, 101, 1561

Postman, M., & Lauer, T. R. 1995, Astrophysical Journal, 440, 28

Press, W. H., & Schechter, P. 1974, Astrophysical Journal, 187, 425

Quintana, H., & Lawrie, D. G. 1982, Astronomical Journal, 87, 1

Rhee, G. F. R. N., van Haarlem, M. P., & Katgert, P. 1991, Astronomy and Astrophysics, 91, 513

Ricketts, M. J. 1978, Monthly Notices of the Royal Astronomical Society, 183, 51P

Riess, A. G., Macri, L., Casertano, S., et al.. 2009, Astrophysical Journal, 699, 539

Rood, H. J. 1981, Reports on Progress in Physics, 44, 1077

Rood, H. J., & Sastry, G. N. 1971, Publications of the Astronomical Society of the Pacific, 83, 313

Sarazin, C. L. 1986, Reviews of Modern Physics, 58, 1

—. 1988, X-ray Emission From Clusters of Galaxies (Cambridge University Press)

Sarazin, C. L. 2002, in Astrophysics and Space Science Library, Vol. 272, Merging Processes in Galaxy Clusters

Sarazin, C. L. 2008, in Lecture Notes in Physics, Berlin Springer Verlag, Vol. 740, A Pan-Chromatic View of Clusters of Galaxies and the Large-Scale Structure, http://www.astro.virginia.edu/∼cls7i/papers/Mexico.pdf, Retrieved 2015

—. 2009, Basic Properties of Clusters of Galaxies and the Physics of the Intracluster Gas, https://www.astro.virginia.edu/∼cls7i/papers/Varenna.pdf, Retrieved 2015

Seyfert, C. K. 1948, Astronomical Journal, 53, 203

Shankar, F., Buchan, S., Rettura, A., et al.. 2015, Astrophysical Journal, 802, 73

Shapiro, S. S., & Wilk, M. B. 1965, Biometrika, 52, 591

Shapley, H. 1933, Proceedings of the National Academy of Science, 19, 591

—. 1944, Proceedings of the National Academy of Science, 30, 61

Shapley, H., & Boyd, C. D. 1940, Proceedings of the National Academy of Science, 26, 41

Shapley, H., & Paraskevopoulos, J. S. 1940a, Proceedings of the National Academy of Science, 26, 31

—. 1940b, Harvard College Observatory Bulletin, 914, 6

Slee, O. B., Perley, R. A., & Siegman, B. C. 1989, Australian Journal of Physics, 42, 633

Slee, O. B., Roy, A. L., & Andernach, H. 1996, Australian Journal of Physics, 49, 977

Slee, O. B., Roy, A. L., & Savage, A. 1994, Australian Journal of Physics, 47, 145

Smith, R. M., Frenk, C. S., Efstathiou, G., Ellis, R. S., & Valentijn, E. A. 1985, Monthly Notices of the Royal Astronomical Society, 216, 71P

Springel, V., White, S. D. M., Jenkins, A., et al.. 2005, Nature, 435, 629

Stephens, M. A. 1974, Journal of the American Statistical Association, 347, 730

Stewart, G. C., Fabian, A. C., Jones, C., & Forman, W. 1984, Astrophysical Journal, 285, 1

Struble, M. F., & Rood, H. J. 1982, Astronomical Journal, 87, 7

—. 1991, Astrophysical Journal, 374, 395

—. 1999, Astrophysical Journal Supplement Series, 125, 35

Sunyaev, R. A., & Zeldovich, Y. B. 1969, Nature, 223, 721

Tonry, J., & Davis, M. 1979, Astronomical Journal, 84, 1511

Tully, R. B., & Fisher, J. R. 1977, Astronomy and Astrophysics, 54, 661

Ulmer, M. P., Wirth, G. D., & Kowalski, M. P. 1992, Astrophysical Journal, 397, 430

van den Bergh, S. 1961, Astronomical Journal, 66, 56

Véron-Cetty, M. P., & Véron, P. 2000, Annual Review of Astronomy and Astrophysics, 10, 81

Vogt, N. P., Forbes, D. A., Phillips, A. C., et al.. 1996, Astrophysical Journal Letters, 465, L15

Voit, G. M. 2005, Reviews of Modern Physics, 77, 207

Wainer, H., & Thissen, D. 1976, Psychometrika, 41, 9

Wegner, G., Colless, M., Saglia, R. P., et al.. 1999, Monthly Notices of the Royal Astronomical Society, 305, 259

West, M. J., & Bothun, G. D. 1990, Astrophysical Journal, 350, 36

White, D. A., Jones, C., & Forman, W. 1997, Monthly Notices of the Royal Astronomical Society, 292, 419

White, S. D. M., & Rees, M. J. 1978, Monthly Notices of the Royal Astronomical Society, 183, 341

Williams, L. L. R., & Saha, P. 2011, Monthly Notices of the Royal Astronomical Society, 415, 448

Wolfram Research, Inc. 2016

Woods, D. F., Geller, M. J., & Barton, E. J. 2006, Astronomical Journal, 132, 197

Yahil, A., & Vidal, N. V. 1977, Astrophysical Journal, 214, 347

Zabludoff, A. I., Geller, M. J., Huchra, J. P., & Vogeley, M. S. 1993, Astronomical Journal, 106, 1273

Zabludoff, A. I., Huchra, J. P., & Geller, M. J. 1990, The Astrophysical Journal Supplement Series, 74, 1

Zhao, D., Aragón-Salamanca, A., & Conselice, C. J. 2015, Montly Notices of the Royal Astronomical Society, 453, 4444

Zhao, J.-H., Burns, J. O., & Owen, F. N. 1989, Astronomical Journal, 98, 64

Zwicky, F. 1933, Helvetica Physica Acta, 6, 110

—. 1937, Physical Review, 51, 290

—. 1938, Publications of the Astronomical Society of the Pacific, 50, 218

—. 1939, Proceedings of the National Academy of Science, 25, 604

—. 1942a, Publications of the Astronomical Society of the Pacific, 54, 185

—. 1942b, Astrophysical Journal, 95, 555

—. 1942c, Physical Review, 61, 489

—. 1950a, Publications of the Astronomical Society of the Pacific, 62, 256

—. 1950b, Publications of the Astronomical Society of the Pacific, 62, 196

—. 1951a, Publications of the Astronomical Society of the Pacific, 63, 17

—. 1951b, Publications of the Astronomical Society of the Pacific, 63, 61

—. 1953, Publications of the Astronomical Society of the Pacific, 65, 215

—. 1956a, Publications of the Astronomical Society of the Pacific, 68, 331

Zwicky, F. 1956b, in Third Berkeley Symposium on Mathematical Statistics and Probability, 113–144

—. 1957, Publications of the Astronomical Society of the Pacific, 69, 518

—. 1959, Handbuch der Physik, 53, 390

Zwicky, F., Herzog, E., Karpowicz, M., Kowal, C. T., & Wild, P. 1961-1968, Catalogue of Galaxies and of Clusters of Galaxies (6 vols.; Pasadena: California Institute of Technology)